Measurement of Solar Magnetic Fields: Development of a Polarimeter for *Multi-Application Solar Telescope*

A thesis submitted in partial fulfillment of

the requirements for the degree of

Doctor of Philosophy

by

Alok Ranjan Tiwary

(Roll No. 11330020)

Under the guidance of

Prof. Shibu K. Mathew

Udaipur Solar Observatory

Physical Research Laboratory, Udaipur, India.

DEPARTMENT OF PHYSICS

INDIAN INSTITUTE OF TECHNOLOGY GANDHINAGAR

2017

Dedicated to

my parents

Declaration

I declare that this written submission represents my ideas in my own words and where others' ideas or words have been included, I have adequately cited and referenced the original sources. I also declare that I have adhered to all principles of academic honesty and integrity and have not misrepresented or fabricated or falsified any idea/data/fact/source in my submission. I understand that any violation of the above will be cause for disciplinary action by the Institute and can also evoke penal action from the sources which have thus not been properly cited or from whom proper permission has not been taken when needed.

Alok Ranjan Tiwary
(Roll No: 11330020)

Date: June 21, 2018

CERTIFICATE

It is certified that the work contained in the thesis titled "**Measurement of Solar Magnetic Fields: Development of a Polarimeter for *Multi-Application Solar Telescope***" by **Alok Ranjan Tiwary (11330020)**, has been carried out under my supervision and that this work has not been submitted elsewhere for a degree.

Dr. Shibu K. Mathew
(Thesis Supervisor)
Professor,
Udaipur Solar Observatory,
Physical Research Laboratory,
Udaipur, India.

Date: June 21, 2018

Acknowledgements

I would like to start by expressing my sincere and deep gratitude to my PhD adviser, Prof. Shibu K. Mathew for his invaluable guidance, encouragement and support throughout my PhD tenure.

I am deeply grateful to Dr. A. Raja Bayanna for his continuous encouragement and generous support throughout my research endeavor. I have enjoyed talking to him about work and other matters on several occasions.

I am also grateful to Prof. P. Venkatakrishnan for his suggestions and constructive comments to improve the quality of work carried out in this thesis. I express my sincere gratitude to the Doctoral Studies Committee (DSC) members as well as thesis experts, Prof. Nandita Srivastava and Dr. Ramitendranath Bhattacharya for their useful comments and suggestions during my IITGN review reports and for throughly reviewing my thesis.

I express my gratitude to the Director of Physical Research Laboratory (PRL), all faculty members, and administrative staff of PRL, for giving me a nice opportunity to pursue my research work. I also express my gratitude to the academic committee of PRL for reviewing my progress in research periodically. I extend my thank to the staff of computer center and library staff (Specially Dr. Nistha Anil Kumar and Dr. Nurul Alam) at PRL for helping me whenever I needed. I thank the faculty members of USO, Prof. Ashok Ambastha, Dr. Bhuwan Joshi, and Dr. Brajesh Kumar for their generous helps and encouragements throughout my research endeavor. A very special thanks to all other staff members of USO, Mr. Raju Koshy, Mr. Rakesh Jaroli, Mr. Pinakin Shikari, Ms. Ramya Bireddy, Mr. Sudarshan Jain, Mr. Naresh Jain, Mr. Mukesh M. Saradava and all the trainees for their help and support in various ways during my stay at USO.

I must express my sincere gratitude to my seniors at USO; Dr. Anand D. Joshi, Dr. Vema Reddy Panditi, Dr. Suruchi Goel, Dr. Wageesh Mishra, Dr. Dinesh Kumar, Dr. Upendra Kushwaha, Dr. Sajal Dhara, Dr. Avijeet Prasad, Dr. Sowmya, Dr. Supriya, and Dr. Sindhuja for helping me at various stages of the thesis work. I also thank all the seniors at PRL for being supportive whenever I visited PRL especially Dr. Gaurav Tomar and his wife Dr. Bhavya. I would like to thank all my batch-mates; Sanjay Kumar, Arun Pandey, Guru Kadam, Girish Kumar, Manu George, Ikshu Gautam, Sharadha Band, Tanmoy Mondal, Gaurava Jaiswal, Abhaya Swain, Chithrabhanu P., Kuldeep Suthar, and my junior

Rahul Yadav, Newton Nath, Pankaj Bhalla, Hemant Saini, Ranadeep Sarkar, Praveer Mitron, and Sushree Sangita for their support during my stay at PRL and USO. I extend my thank to my college and university friends Dr. Mohit Srivastava, Guru Sharan Pathak, Rajkumar Prasad, Baliraj Singh, Arvind Yadav, Arun, Alok, Neeraj, Kaleem, Kishore, Mohit, Mellissa, Anita, Dr. Shipra Pandey and many others who have been always supportive.

I would like to take this opportunity to thank all the family members at USO colony Mrs. Usha Venkatakrishnan, Mrs. Saraswati, Mrs. Mahima, and Mrs. Bharti for inviting me for lunches and dinners on various occasions.

My special thanks to Dr. Dinesh Tripathi sir and Rakesh Bhaiya for their invaluable support, and giving me right-direction at the crucial moment of my life.

I am in dearth of words to thank my parents (Mr. Baliram Tiwary and Mrs. Kalindi Devi) for the encouragement and the support they have provided me throughout my life. Words cannot express my gratitude to them. Therefore, I dedicate my thesis to them. I also thank my dear brothers (Ashutosh Ranjan) and sisters (Majusha and Binu) for their support, suggestions and love. I extend thanks to my other family members, my all cousins (especially Appu Bhaiya and Amod) for their affection and support. I am very thankful to Anamika for her continuous and unconditional support and being with me whenever I felt alone and weak. I am also thankful to her family for their support and faith in me. Last and really not least, I thank all my friends, relatives, teachers and students from whom I have learnt something to be where I am today.

Alok Ranjan Tiwary

Abstract

The solar magnetic field governs all the solar activities occurring at the outer atmosphere of Sun. The magnetic field lines in the solar atmosphere are stressed or deformed by the convective motion at the photosphere. These stressed magnetic field configuration is believed to be responsible for activity phenomena like flares, filament eruptions, coronal mass ejections (CMEs) etc. Majority of the eruptive events occur in the regions of strong and complex magnetic fields called as active regions. These eruptive phenomena directly affect near-Earth space weather by the accompanying high-energy radiation and charged particles. In order to predict these events a detailed investigation of solar magnetic structures is required. Thus, measurement of solar magnetic fields is of utmost importance in solar physics. However, measurement of solar magnetic field is done remotely by measuring the polarization of solar spectral lines induced by Zeeman effect. Polarization measurement is quite a challenging task because the polarization state of incoming light can be modified due to several factors/components (Earth atmosphere, Telescope, other optical components) coming in the path of light beam.

Multi-Application Solar Telescope (MAST), a 50 cm off-axis Gregorian telescope, was installed at Udaipur Solar Observatory (USO), India, which has been made operational recently. For understanding the evolution and dynamics of solar magnetic and velocity fields, an imaging spectropolarimeter has been developed at USO as one of the back-end instruments of MAST. This system consists of a narrow-band imager and a polarimeter. This instrument is intended for the simultaneous observations in the spectral lines at 6173 Å and 8542 Å, which are formed in the photosphere and chromosphere, respectively. The focus of this thesis is on the development of a polarimeter for measuring the polarization signal induced in the photosphere and chromosphere. The polarimeter includes a linear polarizer and two sets of Liquid Crystal Variable Retarders (LCVRs). It is known that the retardance of LCVR depends on the voltage and temperature. Voltage at

a constant temperature is used for fast modulation.

However, fluctuations in the temperature and voltage reduces the accuracy in the polarimetric measurements. Thus we have characterized LCVRs of the polarimeter for various combinations of voltages and temperatures. Further, to achieve a sufficient polarimetric accuracy of 10^{-3} *, it is necessary to calibrate the polarimeter and remove the cross-talk arising from the polarimeter itself. The calibration of the polarimeter is performed by introducing a calibration unit (CU) consisting of a linear polarizer and a zero order quarter wave plate (QWP). Both elements are placed in computer controlled rotating mounts. The calibration unit is placed just after the folding mirror (M6) of MAST. Thus, during operations with MAST, calibration unit is used to generate known polarization by rotating QWP. The polarimeter response function or X-matrix is determined from a comparison between created input and measured output. The application of the inverse matrix* X^{-1} *on the measured Stokes vector removes the cross-talk arised due to properties of the polarimeter components.*

In the thesis, spectropolarimetric observations of various active regions obtained with the imaging spectropolarimeter for MAST are also presented. For verification, we have made comparison of line-of-sight observations of a selected active region obtained from the Helioseismic Magnetic Imager (HMI) onboard the Solar Dynamics Observatory (SDO) with that obtained from observations in the spectral line 6173 Å from MAST telescope. We found good agreement between both the line-of-sight observations, considering the fact that MAST observations are limited by atmospheric seeing.

It is important to note that MAST is a nine mirror system with two off-axis parabolic and seven plane oblique mirrors, the oblique reflections of these mirrors complicate the measurement as the instrumental polarization corrupts the incoming radiation. The polarization induced due to mirrors of telescope is linear. In order to get the vector magnetic field Stokes Q, and U profiles need to corrected using telescope matrix. We have planned to obtain the telescope matrix

both theoretically and experimentally. The thesis is concluded with a discussion on the ongoing experiment for the determination of telescope matrix using sheet polarizer.

Contents

List of Figures

List of Tables

Chapter 1

Introduction

The Sun is our nearest star of which, high spatial resolution imaging is done routinely using various ground and space based telescopes. These contemporary observations have unmasked the dynamic nature of the Sun (Bhatnagar and Livingston 2005). A detailed study is important because solar eruptive events: flares and coronal mass ejections (CMEs) along with solar wind, solar energetic particles (SEPs) and radiations (at multi-wavelengths) influence the Earth and other planets of the solar system—the whole heliosphere. The totality of this influence at the near-Earth space can be nomenclatured as space-weather, which not only is an interesting stand alone physical problem, but also has economic consequences and importance in human safety. For example, many critical technologies upon which society has become increasingly dependent are vulnerable to space-weather events. Such events can damage Earth-orbiting satellites, disrupt communications and GPS networks, disable power grids; and pose health hazards to astronauts and airline passengers on polar routes. The underlying physics of space-weather events are of solar origin and yet to be fully understood. What triggers flares and CMEs, why the solar corona is at million degree kelvin, how the solar wind is accelerated are few such open questions (Tomczyk et al. 2016, and references therein). As per the growing consensus, all the above processes are intricately linked to the magnetic field of the Sun and its evolution. To further

highlight importance of the magnetic field, in the following, a brief description of the Sun's structure is presented with focus on different solar features of magnetic origin.

1.1 Structure of the Sun

The Sun is a main sequence star of spectral type G2V with mass M $\approx 1.98 \times 10^{30}$ kg, luminosity L$\approx 3.84 \times 10^{26}$ W and radius R $\approx 6.96 \times 10^{8}$ m (Lang (2006), p. 24). The mass of the Sun is about 99% of the total mass of the solar system. Similar to other stars, the Sun was born from the gravitational collapse of a molecular cloud approximately around 4.6×10^{9} years ago, and now is currently in a state of hydrostatic equilibrium. It is predicted that the Sun will enter in a red giant phase in another $\approx$ 5 billion years before ending its life as a white dwarf (Foukal 2004).

Based on different parameters and prevailing physics, the Sun can be layered into different zones made of plasma (Bhatnagar and Livingston 2005). Overall, the Sun can be divided into two regions (interior and atmosphere), documented below in detail.

1.1.1 Interior of the Sun

The modern picture of the internal structure of the Sun has been built up over time. The three most important contributions to this have been the standard solar model (SSM; Bahcall et al. (1982)), helioseismology (Leibacher et al. 1985), and solar neutrino observations (Bahcall 2001). As the interior of the Sun cannot be directly observed, its structure is modeled and then compared to the observed properties by iteratively changing the model parameters, until they match with the observations. The SSM is essentially several differential equations, constrained by boundary conditions on mass, radius and luminosity of the Sun. Generally, the methods of helioseismology probe the solar interior by studying

different modes of sound wave (Leighton et al. (1962); Ulrich (1970)).

The interior of the Sun includes the core, the radiation zone and the convection zone (see Figure 1.1). The core extends out to about 0.25 R from the center, having a temperature of about 1.5×10^7 K and has a density $\approx 1.5\times10^5$ kg m^{-3} (Lang (2006)). The core energizes via the process of pp-chain reaction which results in formation of Helium and releases energy in the form of gamma ray photons. Outside the core is the radiative zone which extends out from 0.25 R to 0.70 R. The gamma photons produced in the core are absorbed and re-emitted repeatedly by nuclei in the radiative zone, with the re-emitted photons having successively lower energies and longer wavelengths. The temperature drops from about 7×10^6 K at the bottom of the radiative zone to 2×10^6 K just at the top. Because of large mass density ($\approx 2\times10^4$ kg m^{-3}) of the radiative zone, the mean free path of photons is very small ($\approx 9.0\times10^{-2}$ cm) and the photons take approximately tens to hundreds of thousands of years to travel up to the photosphere, the visible surface of the Sun (Mitalas and Sills 1992). Hence, if the pp-chain reaction at the core suddenly stops, the Sun will continue to shine for an additional million years or more.

Above the radiative zone is the convective zone extending from about 0.70 R to 1 R at the surface of the Sun. At $\approx$ 0.7R, helioseismology shows the sound speed and density profiles to have a distinct sudden bump and the layer is called the tachocline (Spiegel and Zahn 1992). The convection zone rotates differentially and temperature in this zone decreases very rapidly with height, becoming approximately 5700 K at the outer boundary. The energy is transported by convection. Hot regions at the bottom of this layer become buoyant and rise, cooler material from the above descends; creating giant convective cells which can be seen as granules on the photosphere. The plasma at this zone is magnetized and, in presence of magnetic field the space is known to get separated into two types of regions. In one types, magnetic field is excluded and vigorous convection takes place. In other regions, magnetic field gets concentrated in the form of flux-

tubes which are essentially made of magnetic field lines, and the tension of the lines suppresses convection in those regions. Importantly, the flux-tubes rise up because of magnetic buoyancy and pops out of the photosphere creating bipolar sunspots. A co-located cluster of such sunspots constitutes an active region (AR) and the corresponding magnetic field lines traverses through the solar atmosphere before terminating in opposite polarity regions on the photosphere. This large scale magnetic field is important for many solar activities.

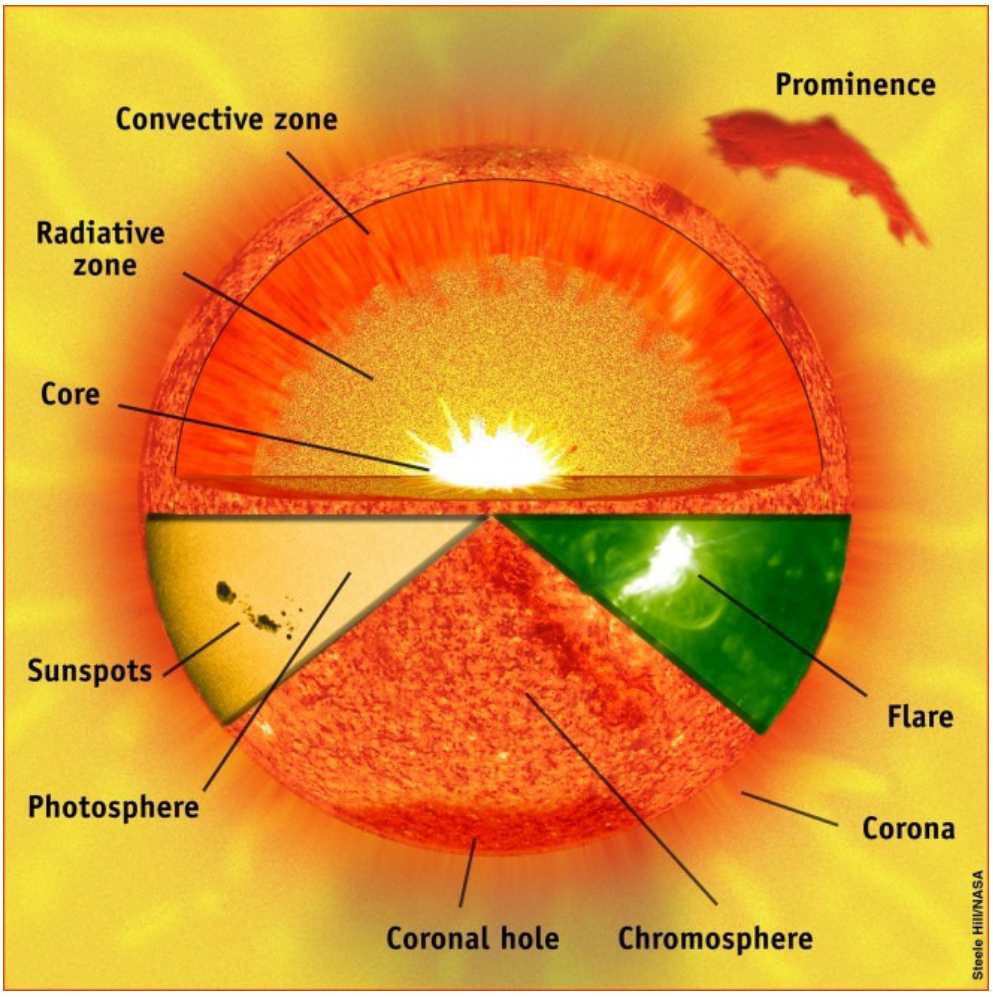

Figure 1.1: Figure shows the complete structure of Sun: the solar interior, features at the surface and the atmosphere of the sun. This is adopted from the website of NASA 'www.thesuntoday.org'.

1.1.2 Atmosphere of the Sun

Based on the density, temperature, and composition; the atmosphere of the Sun is subdivided into three regions: the photosphere, chromosphere and corona. The density of the plasma generally decreases from the photosphere to the corona. However, the temperature decreases before reaching a minimum at the base of the chromosphere, then slowly increases until there is a rapid increase at the transition region which continues into the corona (Figure 1.2).

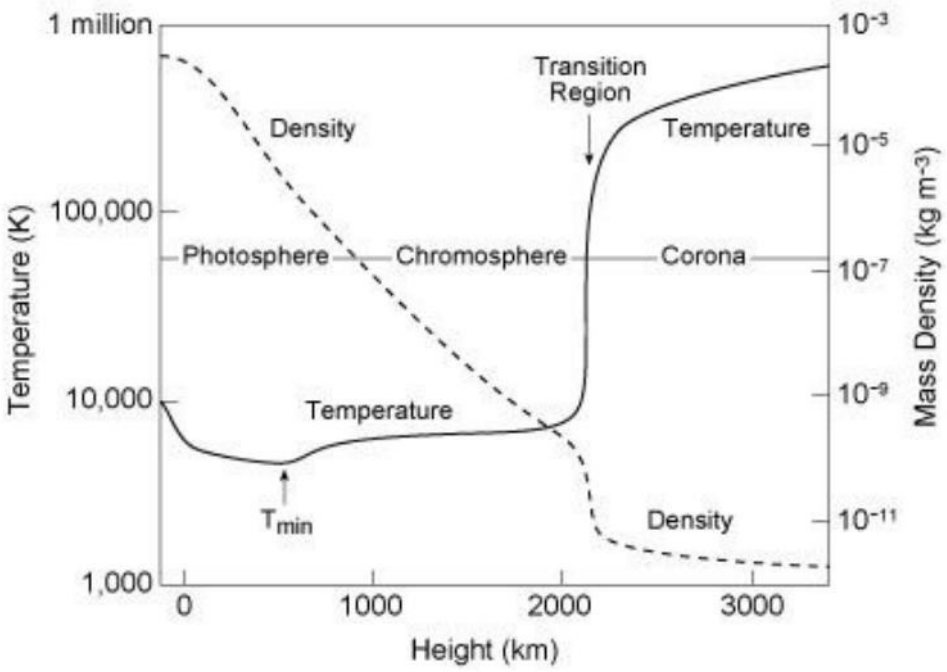

Figure 1.2: The temperature of the solar atmosphere decreases from≈ 5700 K at the visible photosphere to a minimum value of≈ 4,400 K about 500 km higher up. The temperature increases with height, slowly at first, then extremely rapidly in the narrow transition region (less than 100 km thick, between the chromosphere and corona) from ≈ 10,000 K to about one million K. (Courtesy of Eugene Avrett, Smithsonian Astrophysical Observatory, Lang (2006), p. 115)

The solar corona extends millions of kilometers into space and is naturally visible during a total solar eclipse. The three components of the corona (i.e. K-corona, F-corona, and E-corona) are described based on the nature of radiation emitted by them. The K-corona dominates between 1.03 R -2.5 R. From this

region, the emitted scattered light from the coronal plasma shows the continuous spectrum of the photosphere with no Fraunhofer lines and is found to be strongly polarised. The F-corona dominates beyond 2.5 R displays the solar spectrum with Fraunhofer lines superimposed on the continuum. The outer part of the F-corona is observed to merge into the zodiacal light. The E-corona is due to spectral line emission from visible to EUV by several atoms and ions in the inner part of the corona, containing many forbidden line transitions. The corona is tenuous with particle density $\approx 10^6$ to 10^8 cm^{-3} whereas the same for the chromosphere and the photosphere are in the ranges 10^{10} to 10^{12} cm^{-3} and of 10^{16} to 10^{17} cm^{-3} respectively(Golub and Pasachoff (2009), ch. 1). Importantly, the corona is magnetized with an ambient field of 10 to 20 Gauss.

Presently, the chromosphere and corona are observed mostly by space based telescopes at wavelengths ranging from Extreme Ultraviolet to X-rays (Wiegelmann et al. 2015; van Driel-Gesztelyi and Green 2015). However, there are number of ground based telescopes which provide observations of photosphere and chromosphere in visible and infrared wavelengths. The Multi-Application Solar Telescope (MAST) at Udaipur Solar Observatory (USO) is one such ground based instrument which provides simultaneous observations of the photosphere and chromosphere with a FOV limited to 3 arc-min (Figure 1.3). Also, Figure 1.4 shows the full-disk image of the chromosphere in H-alpha (6563 Å), constructed using MAST observations. The atmospheric magnetic field plays a crucial role in different solar activities which are described in the following sub-section.

1.2 Solar Active Regions

In its modern definition, ARs are the totality of observable phenomena in a 3D volume represented by the extension of the magnetic field from the photosphere to the corona (van Driel-Gesztelyi and Green 2015). The simplest ARs have bipolar magnetic field configurations. More complex ARs may develop by emer-

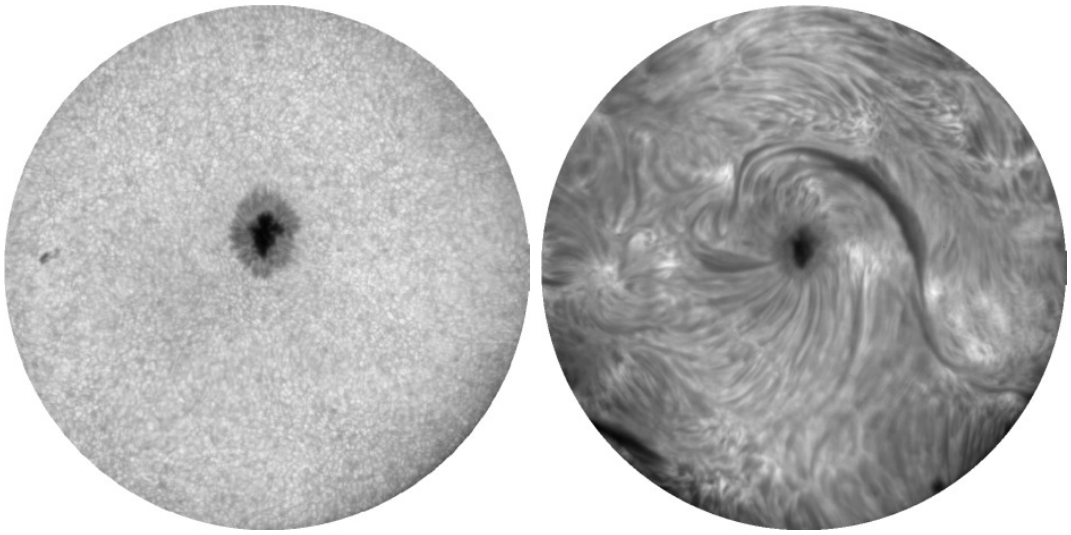

Figure 1.3: Photospheric (left) and chromospheric (right) images taken in G-band (4305 Å) and H-alpha (6563 Å) wavelengths. The images are of active region NOAA# 12356, taken on 04 June 2015, 05:13UT with MAST. The field of view is around 3 arc-min.

gence of several bipoles in close succession within a limited photospheric region. The strong magnetic field in the photosphere is manifested in the form of dark sunspots (see Figure 1.5) or pores, whereas the bright faculae are weak and relatively dispersed magnetic field regions (e.g. Solanki (2003), Borrero and Ichimoto (2011), Stix (2004)). In the chromosphere, arch filament systems connect opposite magnetic polarities. The filaments form along the polarity inversion line and the bright regions that appear above the dispersed fields are called plages (see Figure 1.4). In the transition region and corona; bright, hot, dense loops connect the opposite magnetic polarities. ARs are the principal source of a broad range of solar activity phenomena, ranging from small-scale brightening and jets to solar flares and CMEs. Evolutionary stage of an AR decides the level and type of the solar activity—being highest during the formation phase. Presumably, Active regions do not evolve in isolation. For instance, an AR may emerge into a pre-existing magnetic environment formed by previous active regions. The interactions of the old and new magnetic field lines contribute to the overall evolution. Moreover, field lines from an AR may interact with the open field lines of coronal

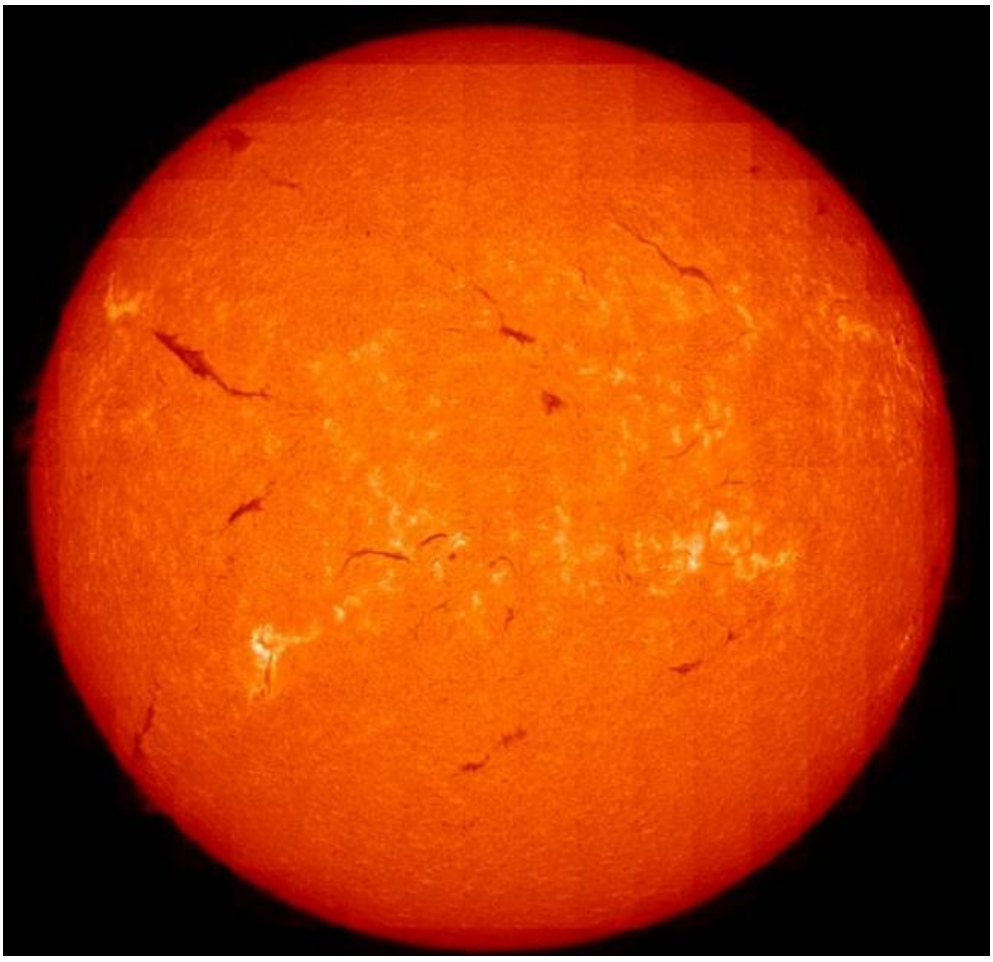

Figure 1.4: Hα full disk image constructed from a sequential mosaic of 293 images taken by MAST on 19th May, 2015.

holes and affect its evolution. Consequently a plausibility is, the large-scale solar magnetic field is determined by the superposed growth and subsequent diffusion of all previously occurring ARs along with their magnetic morphologies and topological complexities. To introspect, formation and morphology/complexity of ARs are crucial to govern the dynamics of large scale magnetic field lines which ultimately lead to different solar transients and space weather effects. It is then imperative to measure the AR magnetic field.

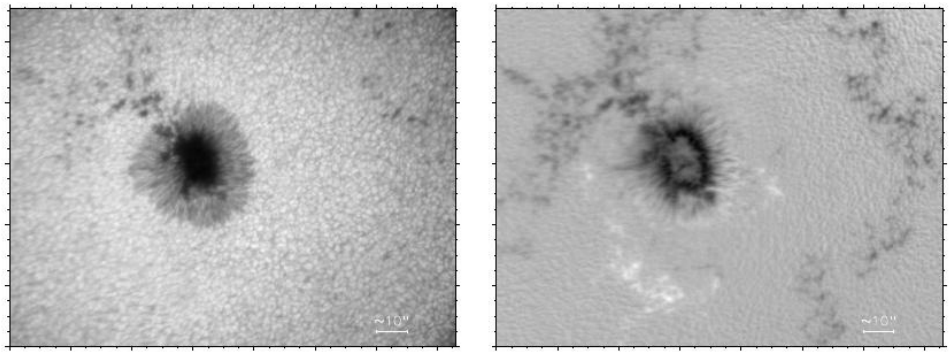

Figure 1.5: One example for the magnetic field measurement carried out at Fe I 6173 Å line. The measurement is carried out on October 24, 2015, of AR#NOAA12436. The right image shows one of the Stokes I images taken in the line continuum and the right image is for Stokes V around 30 mÅ from the line center.

1.3 Measurement of Active Region Magnetic Fields

The Zeeman effect (Zeeman 1897) (discussed in section 1.3.1), has been recognized as the most authentic tool for more than a century to derive the magnetic field of sunspots and pores in the photosphere (Stenflo 2015, and references therein). With the advancement of instrumentation capabilities, one can now measure the Zeeman signals of all kind of magnetic structures (active regions or small-scale structure) present in the photosphere as well as in the chromosphere (Solanki 2003; Stenflo 2015). For example, active regions in the photosphere generally have fields up to $\approx$ 3000 Gauss (Stix 2004) whereas the field strength of active regions in chromosphere is up to the order of hundreds of Gauss (Durrant 1988). However the coronal magnetic field being weak ($\approx$ 20 Gauss), the Zeeman effect becomes insensitive. Therefore, we rely on the Hanle effect (Hanle 1924) for coronal magnetic field measurements. In special cases, both these effects can be combined to have magnetic field measurements in different atmospheric layers of the Sun (Lagg et al. 2015). The standard is to measure polarization state induced by either Zeeman or Hanle effect in the magnetically sensitive spectral lines of the incoming light. The following subsection discusses both these effects in details.

1.3.1 Zeeman Effect

In the presence of magnetic field, a magnetically sensitive (Landé g-factor (g) $\neq$ 0) spectral line widens or splits (depending on the field strength) into different polarized components. This phenomenon is known as Zeeman effect (Zeeman 1897). The polarization of the splitted components of the spectral lines depends on the magnitude and direction of the magnetic field vector. The basic principle of this effect is splitting of the atomic energy levels due to a precession of atoms around the magnetic field as shown in Figure 1.6. In the absence of magnetic field, the energy of atomic levels depends only on the total angular momentum (J) but when magnetic field is present it also depends on M_J, the component of J parallel to the magnetic vector **B** ($-J \leq M_J \leq$J). The energy of each level can be written as

$$E_{J,M} = E_J + \mu_0 g M_J B \tag{1.1}$$

Where g is Landé-g factor and μ_0 is Bohr magneton. Important for observations is the consequent splitting of spectral lines formed between two such levels into three groups of lines according to the selection rule $\Delta\ M_J = 0, \pm 1$. Here $\Delta\ M_J = 0$ corresponds to π component and $\Delta\ M_J = \pm\ 1$ corresponds to σ components (see Figure 1.6).

Notably, for complete Zeeman splitting the magnetic field must be more than 1500 Gauss, else the line only broadens. With additional thermal and Doppler broadening, for lesser magnetic field, the broadening due to the Zeeman effect may get masked. Further, the influence of magnetic field on observed profile may also be substantially reduced if the magnetic features are not spatially resolved. On the contrary, the polarization signatures of the Zeeman components σ and π are unaffected by the Doppler and thermal broadening and hence, typically are used to measure the magnetic field. Importantly, the state of polarization depends on the direction of the magnetic field with respect to the observer.

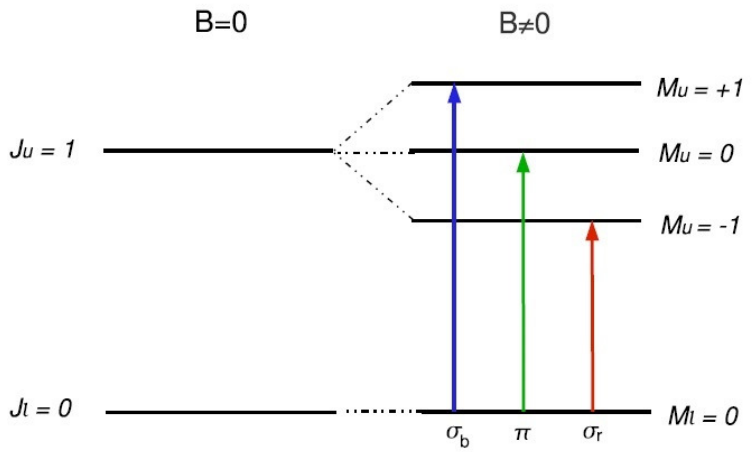

Figure 1.6: Scheme of energy levels for a Zeeman triplet: one un-shifted π component (green) and two shifted σ components (blue and red).

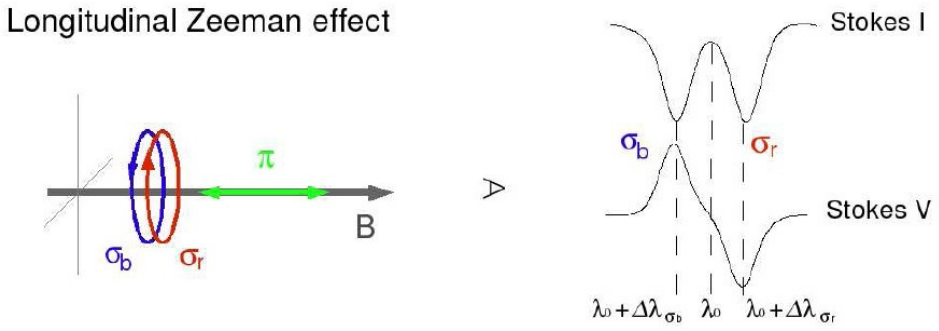

Figure 1.7: Pictorial representation of longitudinal Zeeman effect.

- When magnetic vector is parallel to the line-of-sight (LOS) i.e., for longitudinal field, no π component is visible only the two σ -components are oppositely circularly polarised. This is known as longitudinal Zeeman effect as described in Figure 1.7.

- For a transverse field the π component is linearly polarised and parallel to **B**, while the σ components are linearly polarised and perpendicular to **B**. This is known as transverse Zeeman effect as shown in Figure 1.8.

- For an arbitrary angle between **B** and LOS the light is in general elliptically

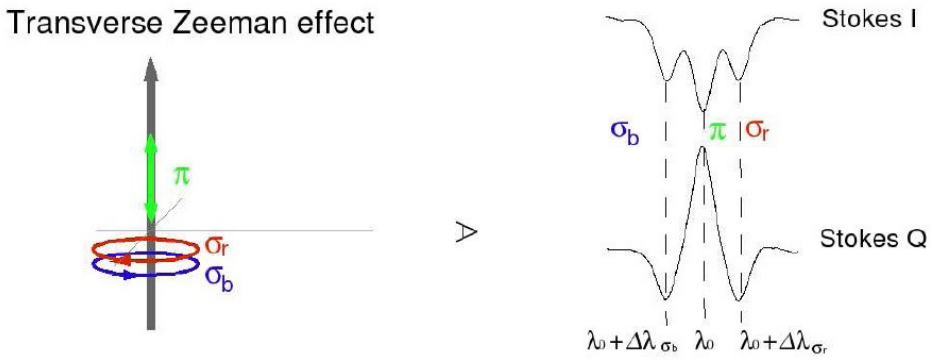

Figure 1.8: Pictorial representation of transverse Zeeman effect.

polarised.

1.3.2 Polarization by Scattering: Hanle Effect

Polarization does not necessarily require a magnetic field in the region where the light originates. Polarized radiation is also produced by scattering. For example, the blue sky is polarized due to Rayleigh scattering of air molecules. A necessary condition for polarization due to scattering is the anisotropic illumination of the scattering particles. A different class of polarization effects, due to coherent scattering can also be used for magnetic field diagnostics. Certain lines in the solar spectrum become polarized when they are partly formed by coherent scattering. Polarization through scattering in the solar atmosphere is always linear with Q/I of order 10^{-3} or smaller. In the presence of magnetic field the precession of the atoms induces a modification, called the Hanle effect, of this scattering polarization. The Hanle effect causes a decrease in the scattering polarization and a rotation of the plane of polarization, and occurs when a magnetic field is present in the observed part of the atmosphere (Hanle 1924). This effect was first investigated by Hanle (1924) in the context of resonant fluorescence. Even a weak magnetic field may lead to depolarization via the Hanle effect, and there is no cancellation of the contributions of unresolved magnetic dipoles such as

that occurs with the circular polarization caused by the Zeeman effect. With the availability of high-precision imaging Stokes polarimeters it has become possible to make use of the Hanle effect as a new tool for magnetic-field diagnostics across the solar disk. The Hanle effect is sensitive to magnetic fields in a different parameter regime as compared with the Zeeman effect, in particular to weak fields, turbulent fields, and chromospheric fields. The Hanle and Zeeman effect compliment each other, since the Hanle effect is sensitive to a different magnetic field regime (weak fields and the fields of mixed polarities) as compared with the ordinary Zeeman effect.

For a complete understanding of the Zeeman and Hanle effect applied to the Sun, readers are referred to the book by Stenflo (1994) and (Stix 2004). This thesis deals only with the measurement of magnetic field using Zeeman effect.

1.3.3 Polarization Measurement

Light can be described as a transverse wave, with an electric and magnetic field oscillating in planes perpendicular to each other and to the propagation direction. The Stokes parameters are a set of values that describe the polarization states of the electromagnetic radiation. The mathematical formulation of these parameters was developed by G.G. Stokes in 1852 (Chandrasekhar 1960; Born and Wolf 1999). The Stokes representation has an advantage that the parameters being intensities, are directly measurable and encompasses all states of polarised light. The four Stokes parameters are I, Q, U, V; where I is the total intensity (i.e. the sum of polarised and the unpolarised fractions of the light), Q and U represent linearly polarized light and V represents the circularly polarized light. The parameters are expressed as

$$I = I_{lin}(\chi = 0) + I_{lin}(\chi = \frac{\pi}{2}), \tag{1.2}$$

$$Q = I_{lin}(\chi = 0) - I_{lin}(\chi = \frac{\pi}{2}), \tag{1.3}$$

$$U = I_{lin}(\chi = \frac{\pi}{4}) - I_{lin}(\chi = \frac{3\pi}{4}), \tag{1.4}$$

$$V = I_{circ}(right) - I_{circ}(left). \tag{1.5}$$

where

$I_{lin}(\chi)$ refers to linearly polarised radiation whose electric vector makes an angle χ to some reference direction.

I_{circ} refers to circularly polarized light.

If the light is completely polarized, then the 4 Stokes parameters are no longer independent of each other:

$$I^2 = Q^2 + U^2 + V^2. \tag{1.6}$$

If light is completely unpolarised then Q=U=V=0 and I=1.

If light is partially polarised then degree of polarisation is defined as:

$$P = \sqrt{\frac{Q^2 + U^2 + V^2}{I^2}} \tag{1.7}$$

Usually, Stokes parameters are arranged in a column vector known as the Stokes vector.

$$\mathbf{I} = [I, Q, U, V]^T$$

The vector **I** is constructed by utilizing a polarimeter consisting of one or more retarder and a linear polarizer. In the Figure 1.9 a schematic is shown for measuring the Stokes parameters where the two retarders are variable retarders but not rotating retarders, and this configuration is one particular example of polarimeter that is adopted in this work. We see that Q and V can be measured

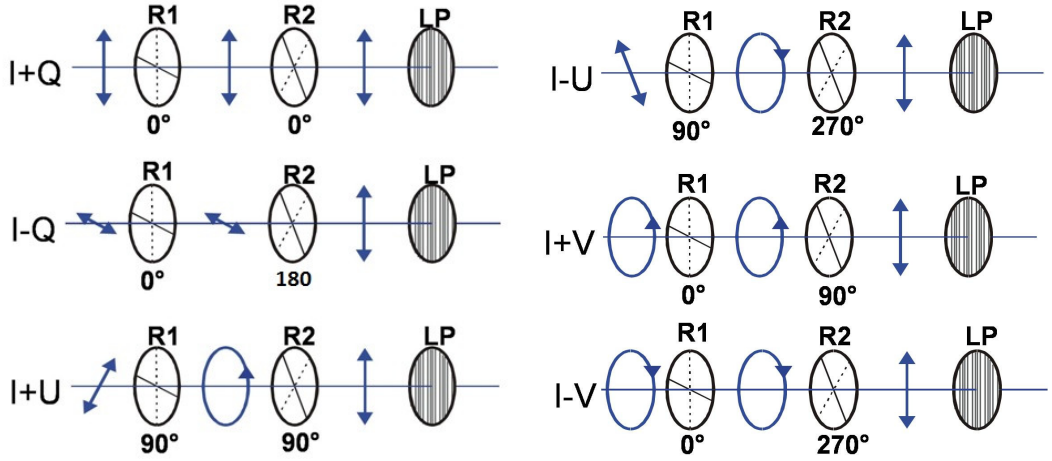

Figure 1.9: Schematic representation of the polarization measurement using two variable retarders (R1 and R2) (not rotating retarders) and a linear polarizer (LP) and this configuration is one particular example of polarimeter that is adopted in this work.

with a variable retarder and a polarizer. However, for measuring U we need two variable retarders along with a linear polarizer. Therefore for Stokes vector measurement, one uses two variable retarders and a linear polarizer in the polarimeter, as shown in Figure 1.10. But with a rotating wave plate, i.e. with a single retarder, all four Stokes parameters can be measured. However, this single rotating retarder scheme takes much longer time to complete one cycle in comparison to a polarimeter which employs variable retarders.

The measured Stokes vector could be used for retrieving various parameters of the solar atmosphere by solving radiative transfer equation (RTE) for polarized light which is discussed in a latter section.

1.3.4 Mueller Matrix

If the light is represented by Stokes vector then the optical components used for measuring the polarization state of light are described by Mueller matrices. Any optical system used to measure the polarization state of the light can be represented by a 4×4 matrix called Mueller matrix (Collett 1992). The output

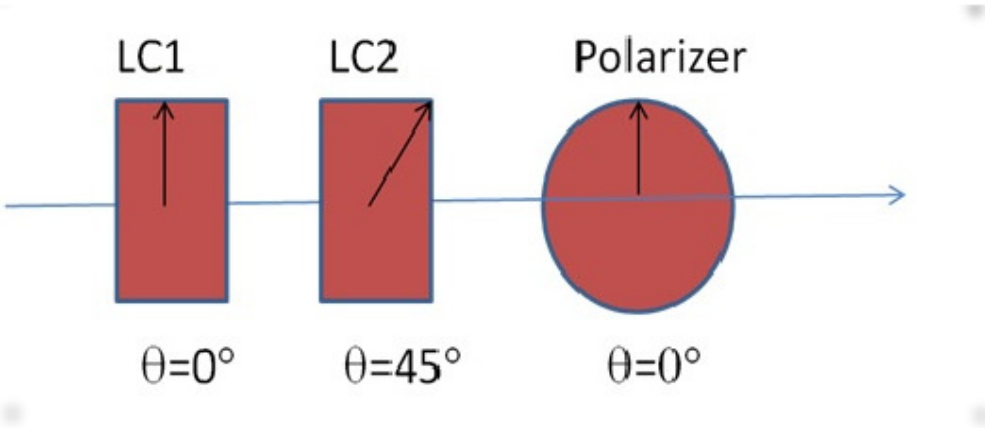

Figure 1.10: Schematic layout of the polarimeter with two variable retarders and a polarizer.

and the input stokes vectors are related through the Mueller matrix as,

$$\mathbf{I}_{out} = M\mathbf{I}_{in}$$

where M is the Mueller Matrix.

If an optical system has a train of optical elements, say 1,2,3,.....,n; with the first element close to an input source, the overall Mueller matrix of the optical system can be constructed by multiplying in order, i.e.,

$$M = M_n M_{n-1} \ldots\ldots\ldots M_2 M_1$$

M is the combined Mueller matrix & M_1, M_2,....., M_n are the Mueller matrices of the optical elements 1,2,....,n respectively. Mueller calculation makes the calibration of the optical system much easier for polarization measurement. To calibrate any optical system, the combined Mueller matrix need to be calculated.

The Mueller matrix of a retarder (M_R) basically depends on the retardation (δ) and the fast axis orientation (θ), which can be expressed as follows.

$$M_R(\theta,\delta) = \begin{pmatrix} 1 & 0 & 0 & 0 \\ 0 & cos^2 2\theta + sin^2 2\theta cos\delta & sin2\theta cos2\theta(1-cos\delta) & -sin2\theta sin\delta \\ 0 & sin2\theta cos2\theta(1-cos\delta) & sin^2 2\theta + cos^2 2\theta cos\delta & cos2\theta sin\delta \\ 0 & sin2\theta sin\delta & -cos2\theta sin\delta & cos\delta \end{pmatrix} \tag{1.8}$$

The Mueller matrix of a linear polarizer (M_{LP}) is given as

$$M_{LP}(\theta) = \frac{1}{2}\begin{pmatrix} 1 & cos2\theta & sin2\theta & 0 \\ cos2\theta & cos^2 2\theta & sin2\theta cos2\theta & 0 \\ sin2\theta & sin2\theta cos2\theta & sin^2 2\theta & 0 \\ 0 & 0 & 0 & 0 \end{pmatrix} \tag{1.9}$$

where θ is the orientation angle of the polarizer.

1.3.5 Radiative Transfer Equation and Milne-Eddington Atmosphere

A typical Radiative Transfer equation (RTE) (Chandrasekhar 1960; Landolfi and Landi Degl'Innocenti 1982) can be expressed in the following form,

$$\frac{dI}{d\tau} = \mathbf{K}(\mathbf{I} - \mathbf{S}) \tag{1.10}$$

where, $\mathbf{I} = [I, Q, U, V]^T$ represents the Stokes vector, τ stands for the continuum optical depth, $\mathbf{S}$ for the Source function vector, and $\mathbf{K}$ represents the 4×4 propagation matrix. All the medium properties relevant to line formation are contained in $\mathbf{K}$ and $\mathbf{S}$. Under local thermodynamic equilibrium (LTE) conditions, source function becomes $S = [B_\lambda(T), 0, 0, 0]^T$, where $B_\lambda(T)$ is the Planck function at local temperature T.

The propagation matrix **K** is given by (Unno and Kato 1962)

$$K = \begin{pmatrix} \eta_I & \eta_Q & \eta_U & \eta_V \\ \eta_Q & \eta_I & \rho_V & -\rho_U \\ \eta_U & -\rho_V & \eta_I & -\rho_Q \\ \eta_V & \rho_U & -\rho_Q & \eta_V \end{pmatrix} \tag{1.11}$$

where

$$\begin{aligned} \eta_I &= 1 + \frac{\eta_0}{2}\{\phi_p sin^2\theta + \frac{1}{2}[\phi_b + \phi_r](1 + cos^2\theta)\} \\ \eta_Q &= \frac{\eta_0}{2}\{\phi_p - \frac{1}{2}[\phi_b + \phi_r]\} sin^2\theta cos2\varphi \\ \eta_U &= \frac{\eta_0}{2}\{\phi_p - \frac{1}{2}[\phi_b + \phi_r]\} sin^2\theta sin2\varphi \\ \eta_V &= \frac{\eta_0}{2}[\phi_r - \phi_b] cos\theta \end{aligned} \tag{1.12}$$

and

$$\begin{aligned} \rho_Q &= \frac{\eta_0}{2}\{\psi_p - \frac{1}{2}[\psi_b + \psi_r]\} sin^2\theta cos2\varphi \\ \rho_U &= \frac{\eta_0}{2}\{\psi_p - \frac{1}{2}[\psi_b + \psi_r]\} sin^2\theta sin2\varphi \\ \rho_V &= \frac{\eta_0}{2}[\psi_r - \psi_b] cos\theta. \end{aligned} \tag{1.13}$$

Here $\varphi_{p,b,r}$ and $\psi_{p,b,r}$ are the absorption and dispersion profiles respectively, the p, b, r indices stand for the central, red-wing, and blue-wing components of a Zeeman triplet respectively, and η_0 is the ratio between the line and continuum absorption coefficients respectively. θ is the inclination angle of the magnetic field vector with respect to the propagation direction and ϕ is the azimuth angle of magnetic field B with respect to Stokes Q positive direction.

The RTE can be solved analytically by assuming the Milne-Eddington (ME)

model atmosphere. A ME atmosphere can be described by a set of parameters which contains the magnetic and thermodynamic quantities (Del Toro Iniesta 2003, and references therein). It assumes that all the atmospheric quantities are constant with depth except for the source function that varies linearly with height.

$$\mathbf{S} = \mathbf{S}_0 + \mathbf{S}_1 = (S_0 + S_1\tau)[1,0,0,0]^T \tag{1.14}$$

The analytical solution of radiative transfer equation under ME atmosphere is known as Unno-Rachkovsky solution and is given by

$$\begin{aligned}
I &= S_0 + S_1\Delta^{-1}[(1+\eta_I)((1+\eta_I)^2 + \rho_Q^2 + \rho_U^2 + \rho_V^2)] \\
Q &= -S_1\Delta^{-1}[(1+\eta_I)^2\eta_Q + (1+\eta_I)(\eta_V\rho_U - \eta_U\rho_V) + \rho_Q(\eta_Q\rho_Q + \eta_U\rho_U + \eta_V\rho_V)] \\
U &= -S_1\Delta^{-1}[(1+\eta_I)^2\eta_U + (1+\eta_I)(\eta_Q\rho_V - \eta_V\rho_Q) + \rho_U(\eta_Q\rho_Q + \eta_U\rho_U + \eta_V\rho_V)] \\
V &= -S_1\Delta^{-1}[(1+\eta_I)^2\eta_V + \rho_V(\eta_Q\rho_Q + \eta_U\rho_U + \eta_V\rho_V)]
\end{aligned}$$

where,

$$\Delta = (1+\eta_I)^2[(1+\eta_I)^2 - \eta_Q^2 - \eta_U^2 - \eta_V^2 + \rho_Q^2 - \rho_U^2 - \rho_V^2] - (\eta_Q\rho_Q + \eta_U\rho_U + \eta_V\rho_V)^2 \tag{1.15}$$

These solutions are functions of line-to-absorption coefficient ratio η_0, the Doppler width of the line $\Delta\lambda_D$, the central wavelength of the line λ, the damping parameter a, and the three components (B,θ,ϕ) of the magnetic field. Hence, the whole model is specified by these seven parameters plus the two parameters describing the source function, S_0 and S_1. The synthetic profiles of the Stokes parameters are shown in Figure 1.11 for different values of magnetic field strength when other parameters are constant.

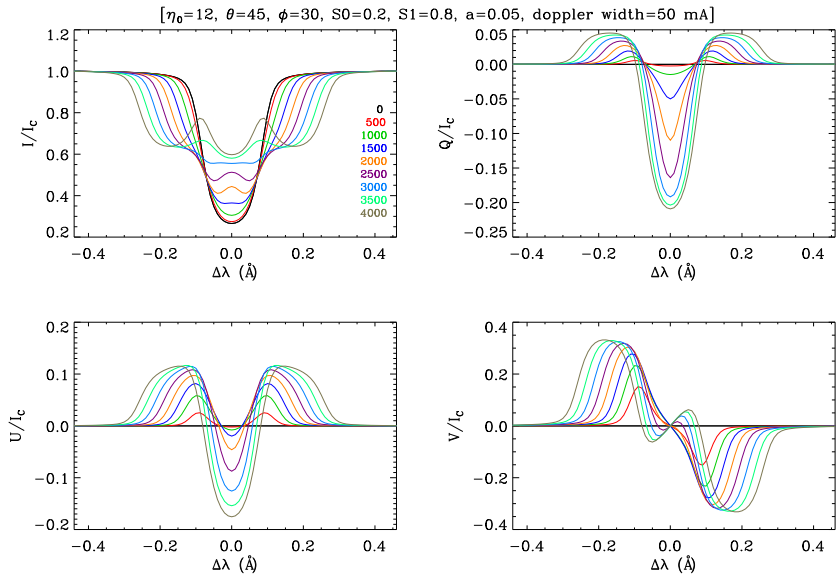

Figure 1.11: Analytical Stokes profiles of a Zeeman triplet of Fe I 6173 Å in a Milne-Eddington atmosphere for different magnetic fields when other parameters are constant.

1.4 Objective and overview of the thesis

The solar activity is an immediate consequence of solar magnetic field. Majority of the eruptive events, solar flares and CMEs, occur in the regions of strong and complex ARs. The magnetic field lines in the solar atmosphere are continuously shuffled by the convective motion at the photosphere, resulting in a build up of stresses in the field lines. The stored magnetic energy of this stressed field eventually releases into kinetic energy and heat via the process of magnetic reconnection, which is believed to be responsible for various eruptive phenomena. An understanding of the underlying physics requires a quantitative measurement of AR magnetic fields, especially at photosphere and chromosphere, and LOS velocity—which is the aim of the thesis. A cadence of more than one minute is sufficient to study the evolution of active regions and energy build-up due to the foot point motions (Wiegelmann and Sakurai 2012; Rempel and Schlichenmaier 2011, and references therein). Magnetogram (by tuning the filter to a single wavelength position) can be obtained with a cadence of 10 seconds, which

could be used for studying the magnetic field evolution of small scale moving magnetic features seen around the sunspot. A six wavelength step scan, which takes around 50 seconds can reproduce the line profile as seen in SDO/HMI is suitable for the vector magnetic field retrieval, as long as the horizontal speed of the moving feature is below 3 kms^{-1} (Ma et al. 2015, and references therein). In order to achieve this, we have developed an imaging based spectro-polarimeter as a back-end instrument of MAST for simultaneous measurement of magnetic field in the photosphere and chromosphere. The thesis is organized in six chapters. The overview of the thesis is provided below.

In chapter 2, we have given a brief description of MAST, its scientific goals, and its back-end instruments. Particularly, we provide a detailed description of the newly developed imaging spectropolarimeter for MAST. Imaging spectropolarimeter consists of a narrow-band imager and a polarimeter which is used for measuring the Stokes vector at two different wavelengths *i.e.* at 6173 Å and 8542 Å, respectively. The narrow-band imager is designed using two z-cut Lithium Niobate ($LiNbO_3$) Fabry-Perot etalons placed in tandem to provide a better spectral resolution. The polarimeter consists of two Liquid Crystal Variable Retarders (LCVRs) and a linear polarizer. In this chapter, we have also discussed the design of the polarimeter, different modulation schemes for the measurement of Stokes parameters, and inversion techniques to retrieve the magnetic field from the Stokes I, Q, U and V observations.

In chapter 3, we have described the experimental setup which has been used for characterizing the polarimeter components. The main component of the polarimeter is LCVR made of nematic liquid crystals. We studied the effect of various parameters on the retardance of the LCVR. We derived voltages required for the corresponding retardance used in the modulation schemes by characterizing all the LCVRs in a laboratory setup. We also discussed the effect of temperature on the retardance of LCVR and the effect of voltage on the orientation of the fast axis of the LCVR. Relevantly the accurate determination of retardance of

LCVRs is very important for sensitive Stokes polarimetry.

In chapter 4, we have discussed about the efficiency and sensitivity of the polarimeter. In this regard, we have estimated the exposure time and the number of polarization measurements needed for the required polarimetric accuracy. We also analyzed several factors which contribute to the polarimetric accuracy. We have used two separate polarimeters for the photospheric and chromospheric measurements at two different wavelength 6173 Å and 8542 Å. The response matrices were experimentally determined in the lab for both the polarimeters and correspondingly modulation schemes (involving four and six measurements). As the optical set-up in the imaging spectropolarimeter differs from the lab set-up, we installed a calibration unit with the spectropolarimeter setup for intermittent calibration of the polarimeter. The obtained new response matrix is also presented in this chapter.

In chapter 5, we have presented the spectropolarimetric observations taken with the imaging spectropolarimeter. After interfacing the polarimeter with the imager, we obtained observations in Fe I 6173 line by operating the polarimeter in longitudinal and vector mode. We also carried out a comparison of our results obtained from preliminary observations with the magnetograms availed from *Helioseismic Magnetic Imager* (HMI) instrument onboard the *Solar Dynamics Observatory* (SDO). Qualitatively, the two observations match well, considering the fact that MAST observations are limited by seeing. After analyzing the preliminary observations, we have carried out a re-tuning of the etalons to optimally cover the continuum at blue and red side of the spectral line. On 16 April, 2016, the Stokes V scan was carried out after the re-tuning of the FP filters. Another observation of a small pore and internetwork region in the active region NOAA AR 12648 taken under moderate seeing on 07 April 2017 is also discussed. After the dark and flat field correction the Stokes I and V profiles have been inverted using SPIN code. We also present the circular polarization measurements obtained in the chromospheric CaII 8542 Å line. We have also operated the polarimeter

in vector mode and preliminary observations of all the Stokes parameters are presented in this chapter.

In chapter 6, summary and conclusions of the thesis are presented. We also discuss the future work in this chapter.

Chapter 2

Spectropolarimeter for Multi Application Solar Telescope

2.1 Introduction

The Multi-Application Solar Telescope (MAST) (Denis et al. 2008, 2010; Mathew 2009) is a 50 cm off-axis Gregorian telescope that has recently become operational at the Udaipur Solar Observatory (USO), India. The telescope is designed to provide near diffraction limited observations with adaptive optics system. The major science goals that can be addressed using MAST are as follows:

- High-angular resolution observations of the Sun in different wavelengths to understand the properties of small-scale magnetic and velocity fields in addition to the dynamics of small-scale intensity features in the photosphere and chromosphere.

- Simultaneous measurement of magnetic and velocity fields of photosphere and chromosphere to understand the solar activities using spectropolarimetric observations in 6173 Å and 8542 Å.

- Understanding the topology and evolution of emerging flux regions which

lead to flares and CMEs.

- Explaining the magnetic and velocity structure of sunspots and small scale features such as pores in the photosphere and the chromosphere, decay of sunspots and their relation to moving magnetic features.

2.1.1 Brief Description of MAST

The telescope is designed and developed by Advanced Mechanical Optical Systems (AMOS), Belgium. The optical layout of the telescope is shown in Figure 2.1. The telescope has an off-axis Gregorian design with 50 cm aperture. The primary mirror (M1) is made of Zerodur and has a focal length of 2 m. The field selector placed at prime focus allows 3 arc-min FOV to pass through the remaining optics. The secondary mirror (M2) placed close to the field stop collimates the light. The Coude train, which consists of three mirrors (M3, M4 and M5), sends the beam vertically down to the observing floor. The telescope is placed on an alt-azimuth mount and thus causes image rotation. The beam is sent through an image derotator (M6, M7 and M8) before reaching the folding mirror M9. From M9 the collimated beam is send to the back-end instruments in the observing floor.

The secondary support structure is not in the path of the incoming sunlight for an off-axis design thereby avoiding any light scattered from the secondary support structure from reaching the M1. An increased collecting area is available compared with the same size on-axis telescope since there is no central obscuration on the primary mirror. Another advantage is the availability of the full pupil plane image for adaptive-optics wavefront sensing. A more detailed discussion on the advantages of off-axis design can be found in Kuhn and Hawley (1999). A stiff central structure connects the altitude shafts of the alt-azimuth mount. M1 is placed on this structure (see Figure 2.2). A reinforced strut structure keeps the M2 connected to the central structure. M2 is mounted on a hexapod

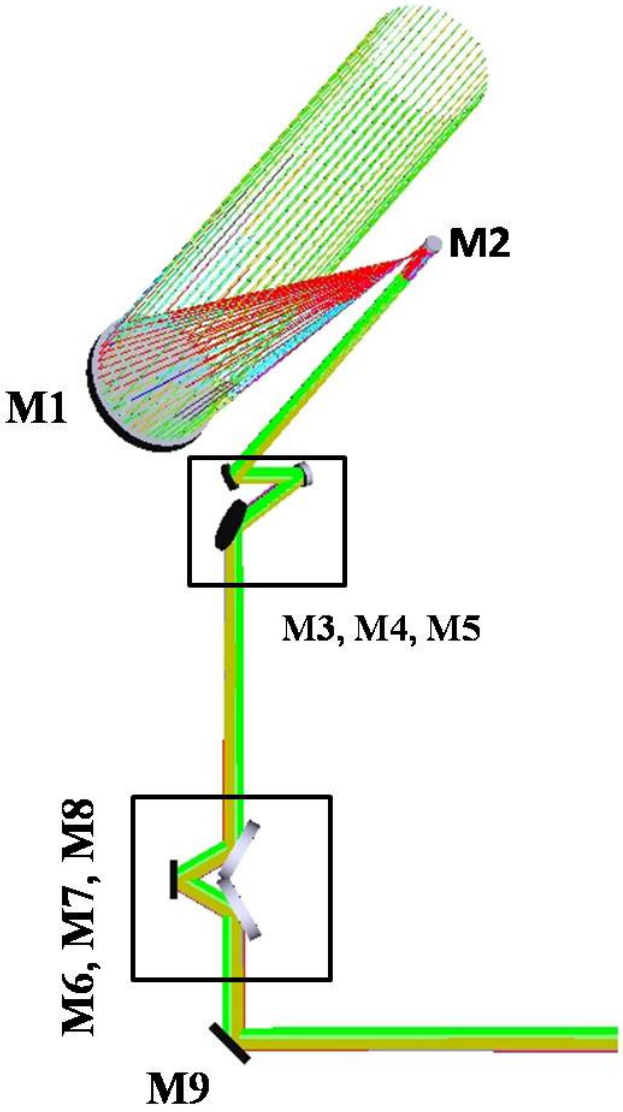

Figure 2.1: Optical design of the Multi-Application Solar Telescope (MAST).

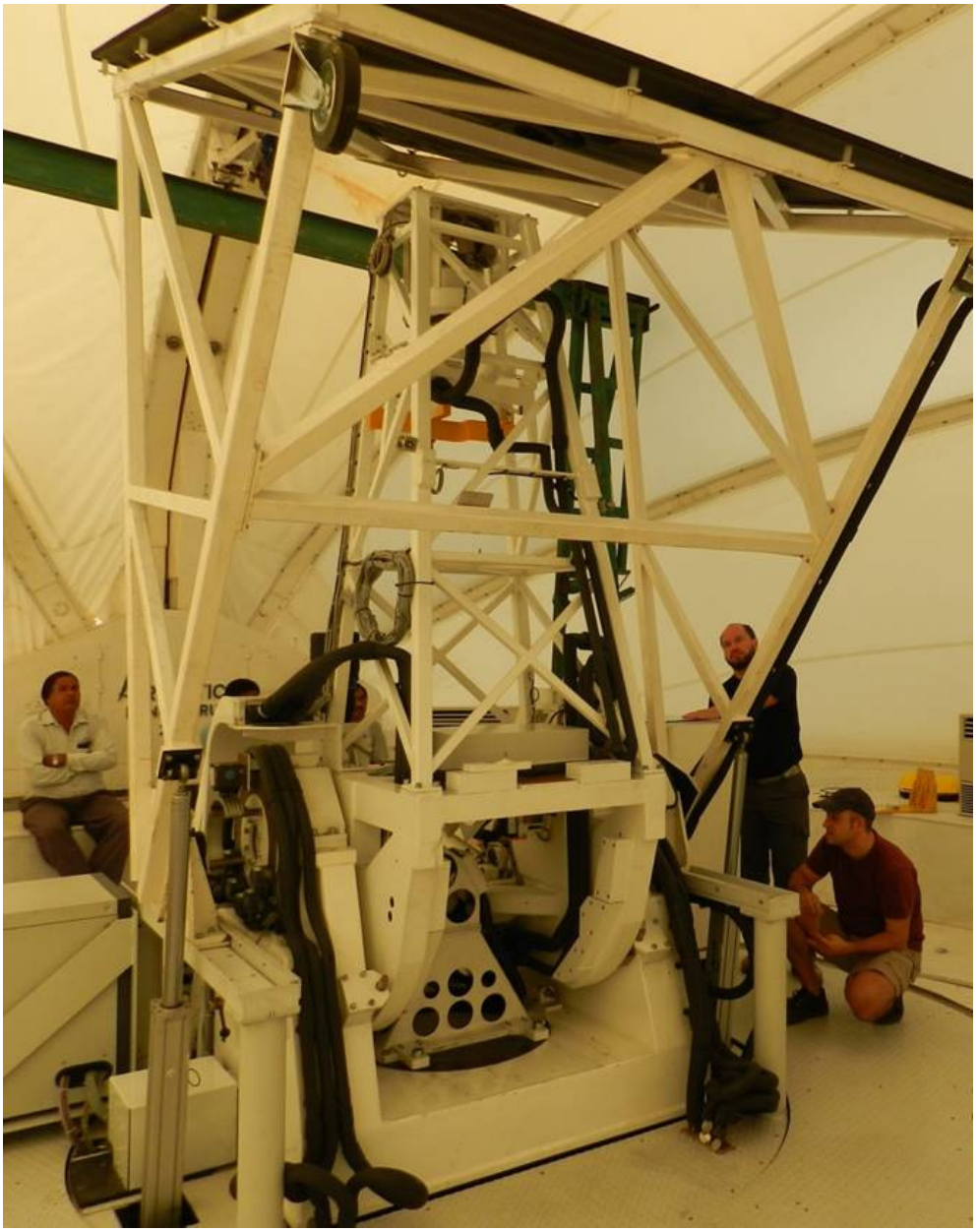

Figure 2.2: Mechanical design of Multi-Application Solar Telescope.

which has correcting capabilities for tilt, centering and translation. The altitude and azimuth drives are controlled by a Delta Tau programmable multi-axis controller[1] (PMAC) with a dedicated Telescope Control Software (TCS). A closed loop tracking accuracy of 0.1 arcsec for an hour and a differential tracking accuracy of 0.5 arcsec are expected for the drive system. The thermal design of the telescope is aimed at reducing the solar flux falling on the opto-mechanical components in order to avoid any differential expansion of the support structure. The temperature of the optical and opto-mechanical components are also controlled to minimize the difference with the ambient temperature and mitigates the seeing degradation. The thermal control is achieved by several ways. A sunshield, moving with the telescope, and allowing only the primary mirror to receive the sunlight, shades the mechanical components of the telescope structure from direct sunlight. The mirror M1 is thermally controlled by means of two conduits of air flows with controlled temperatures. This keeps the primary mirror within $\pm 1^{\circ}$C of the ambient. Heating or cooling of the main telescope elements is also carried out to keep the temperature as close to the ambient as possible.

2.2 Back-end Instruments of MAST

In order to use the full capability of the 50 cm telescope we are integrating various back-end instruments with the telescope. The following back-end instruments were developed at USO to accomplish the stated science goals of MAST:

1. **G-band imager:** This instrument is used to regularly observe the photosphere with a temporal resolution of 10 images per second. It consists of broadband interference filter centered at 4302 Å with passband of 10 Å and a 1376×1040 PCO sensicam^{TM} CCD (Figure 2.3).

2. **H-alpha imager:** This instrument is used to regularly observe the chro-

[1]https://www.deltatau.com

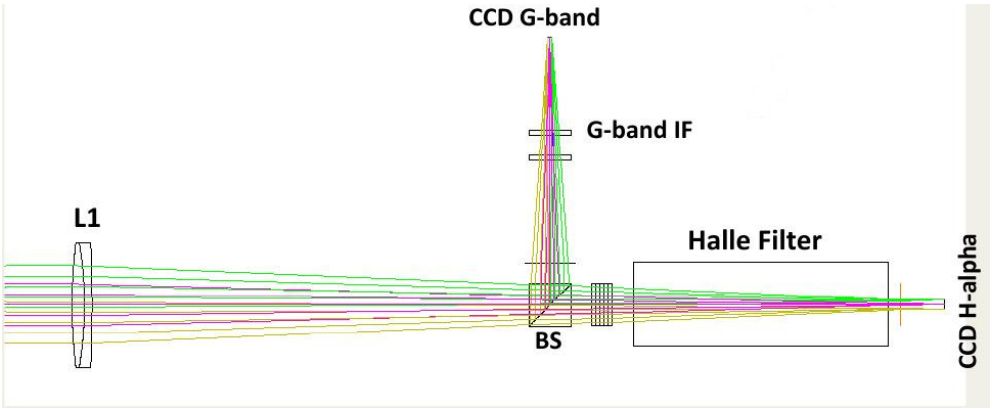

Figure 2.3: Schematic optical setup for the G-band imager and H-alpha imager with MAST.

mosphere with a temporal resolution of 5 images per second. It consists of narrow-band Halle filter centered at 6563 Å with passband of 500 mÅ and a 1024×1024 Photon Max^{TM} CCD (Figure 2.3).

3. **Adaptive Optics (AO):** In order to have diffraction limited images from the telescope an adaptive optics system is installed with MAST for the seeing compensation. A two stage correction will be carried out; a tip-tilt mirror for the global tilt (first order) correction and a membrane mirror with 37 actuators for the higher order corrections. The adaptive optics system could potentially provide seeing corrected diffraction limited images for a FOV of around 15 arc-secs (Figure 2.4).

4. **Narrow-band imager:** This instrument is used for the photospheric and chromospheric observations at wavelengths Fe I 6173 Å and Ca II 8542 Å respectively. It consists of a blocking filter and two voltage tuneable Lithium Niobate ($LiNbO_3$) Fabry-Perot etalons in tandem (Figure 2.4). More details about this instrument is discussed in Raja Bayanna et al. (2014) and Mathew et al. (2017).

5. **Polarimeter:** For the measurements of solar magnetic fields, a polarimeter is integrated along with the narrow-band imager. Polarimeter, consists of

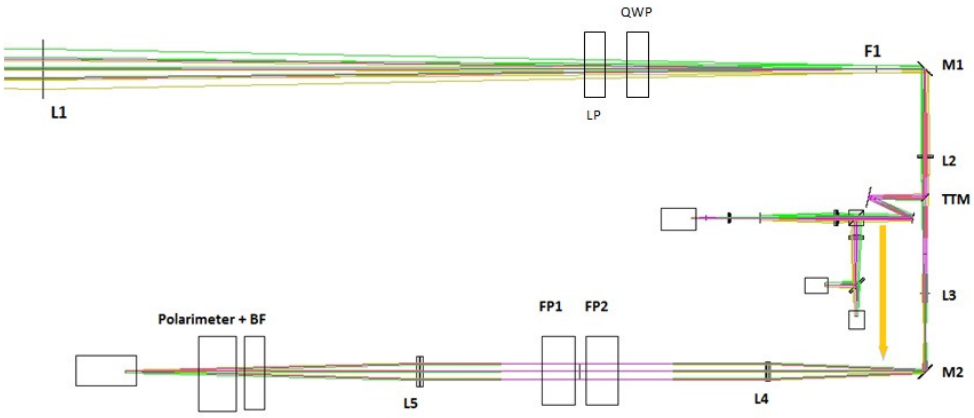

Figure 2.4: Schematic of the optical setup for the narrow band imager, adaptive optics, and polarimeter integrated with MAST.

two liquid-crystal variable retarders and a linear polarizer, is used for the measurements of Stokes parameters for two wavelengths 6173 Å and 8542 Å (Figure 2.4). The details of the polarimeter is presented in Section 2.4.

6. **Multi-slit spectropolarimeter:** It is a scanning, Echelle, Littrow multi-slit spectrograph, with five slits suitably separated to cover around 4 Å spectral range. The spectral range includes the two Fe I lines around 6302 Å. The inclusion of the multi-slit improves the scanning speed by five times compared with single slit spectrograph.

2.3 Solar Spectropolarimetry

As discussed in chapter 1, light gets polarized and depolarized in the presence of magnetic field. The polarization of light is described in terms of the Stokes parameters I, Q, U, and V (Chandrasekhar 1960; Born and Wolf 1999), where I denotes the total intensity, Q and U represents the linear polarization and V represents the circular polarization. The spectropolarimeter consists of a filtergraph/spectrograph and a polarimeter, and is employed to derive the solar vector

magnetic fields by measuring Stokes I, Q, U, and V. Generally, two different techniques have been commonly used for spectral analysis: (1) imaging (filter) based and (2) spectrograph (slit-based). For polarization analysis either single beam polarimeter or dual-beam polarimeter is employed. In imaging based spectropolarimetry, 2D images are obtained in a sequence by tuning a narrow-band filter to different wavelengths along the spectral line profile of interest. Modern imaging spectropolarimeters employ either single or multiple Fabry-Perot (FP) etalons as narrow-band filters because of their high transmission and fast tuning capability. A few examples of the currently working imaging spectropolarimeters are:

- *GREGOR Fabry-Perot instrument* (GFPI; Denker et al. (2010), (Puschmann 2016, and references therein)),
- KIS/IAA *Visible Imaging Polarimeter* (VIP; Beck et al. (2010)),
- *CRisp Imaging Spectro-Polarimeter* (CRISP, Scharmer et al. (2008)),
- the Gottingen spectropolarimeter (Bendlin et al. 1992; Bello González and Kneer 2008),
- *Interferometric BIdimensional Spectrometer* (IBIS; Cavallini (2006)),
- *Imaging Vector Magnetograph* (IVM; Mickey et al. (1996)),
- *Imaging Magnetograph eXperiment* (IMaX; Martínez Pillet et al. (2011)) flown with the *Sunrise* balloon mission (Barthol et al. 2011).

These instruments differ in the number of etalons and the optical configuration (telecentric or collimated).

Contrarily, slit-based spectropolarimeter obtains the spectrum for a given slit position and scans over the required field-of-view (FOV) in sequence. Examples of slit-based spectropolarimeters are:

- *Diffraction Limited Spectro-Polarimeter* (DLSP; Sankarasubramanian et al. (2003)),

- *POlarimetric LIttrow Spectrograph* (POLIS; Beck et al. (2005)),
- *Spectro-Polarimeter for Infrared and Optical Regions* (SPINOR; Socas-Navarro et al. (2006)),
- Spectropolarimeter of the *Solar Optical Telescope* (SOT) onboard the *Hinode* (Ichimoto et al. (2008), Tsuneta et al. (2008)),
- Multi Slit Spectropolarimeter for MAST (MSSP, Mohankrishna et al., 2017).

Either of the above mentioned techniques are preferred based on the scientific requirement. However, with the advances in the technology, both these techniques yield similar results.

2.3.1 Imaging-based Spectropolarimetry with MAST

To accomplish the scientific objectives of MAST as discussed in Section 2.1, an imaging spectropolarimeter has been developed. It consists of a narrow-band imager and a polarimeter which are used to measure the Stokes vector at two different wavelengths 6173 Å and 8542 Å; corresponding to photospheric and chromospheric heights respectively. The criteria to select these spectral lines is based on high Landé-g factor and absence of blends of molecular lines nearby the core of spectral lines.

The narrow-band imager is designed using two z-cut Lithium Niobate ($LiNbO_3$) FabryPerot etalons placed in tandem to provide a better spectral resolution. The wavelength characterization of the components of the narrow-band imager is described in Raja Bayanna et al. (2014). The integration and test results of the imager obtained with MAST is presented in Mathew et al. (2017). The full-width at half maximum (FWHM) of the FP combination is $\approx$ 95 mÅ at 6173 Å with an effective free-spectral range (FSR) of 6 Å. A blocking filter of 2.5 Å is introduced to restrict the FP channel of the desired wavelength. We use only one etalon with 175 mÅ FWHM for the Ca II 8542 Å line. The polarimeter consists of two

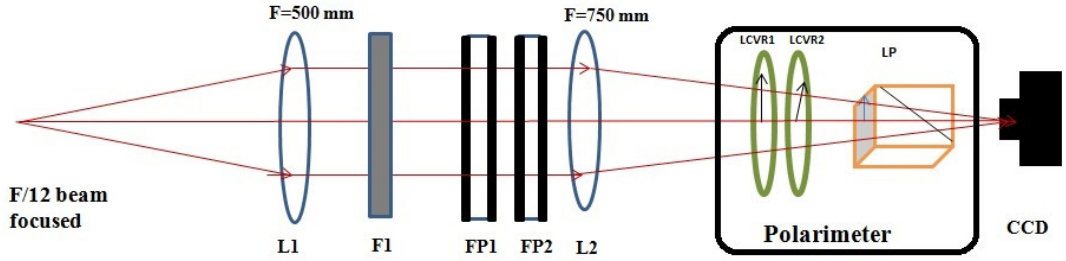

Figure 2.5: Schematic diagram of the imaging polarimeter for MAST. In this setup a F/12 beam from the telescope is collimated using the lens L1. The collimating beam passes through narrow-band imager consists of two Fabry-Perot etalons (FP1 and FP2) and prefilter F1. Polarimeter consist of two LCVR and a Glan-Thompson polarizer is kept in between the CCD and imaging lens (L2) in the converging beam. The F-number of the converging beam is 18.

liquid crystal variable retarders (LCVRs) and a linear polarizer (Glan-Thompson polarizer). More details about polarimeter will be discussed in the latter sections. The optical setup of the spectropolarimeter is shown in Figure 2.5. The F-12 beam from the telescope was collimated using a lens (L1) of focal length 500 mm. The FPs were placed in this collimated beam in order to reduce the wavelength shift produced by the finite incidence angle arising from the FOV. The collimated output through the FPs was imaged using a lens (L2) of focal length 750 mm, which provides a plate scale of 0.145 arcsec pixel^{-1} at the CCD plane. The polarimeter was placed in this converging beam after the lens L2, to accommodate the smaller Glan-Thompson polarizer. The acceptance angles of the LCVRs are large enough to work with the resultant F-18 beam. Since the z-cut etalons with a small incidence angle produce negligible polarization effects, we did not separately consider the effect of the etalons in the polarization measurements. The fast axes of the first and second LCVRs were kept at 0° and 45° with respect to the polarization axis of the linear polarizer. The temperatures of the LCVRs were kept at 28°C.

2.4 Polarimeter for MAST

A polarimeter measures the polarization of the light by modulating the input polarization into measurable intensities. In general, the polarization analysis can be done in two ways (Del Toro Iniesta 2003, and references therein): (a) Temporal polarization modulation/single beam polarimetry in which the different polarization measurements are obtained sequentially. The time gap between the measurements could introduce seeing related spurious signals in the difference image (Lites (1987); Leka and Rangarajan (2001)). This can be minimized either by compensating the atmospheric turbulence by adaptive optics or by implementing a very fast modulation scheme, wherein one modulation cycle is completed before atmospheric seeing changes completely, or by both. However, this imposes stringent requirements on the polarization modulator. (b) Spatial polarization modulation/Dual beam polarimetry (Lites 1987) in which the orthogonal polarization states are separated by means of the polarizing beam splitter or displacer and both the beams are recorded simultaneously. This cancels out the fluctuations in the Stokes I to the other Stokes parameters caused due to atmospheric seeing (Martínez Pillet et al. 2011). Since both the beams are used for final computation of the Stokes parameters, this method improves signal-to-noise ratio (S/N) by a factor of $\sqrt{2}$ as compared to the single beam polarimetry. However, different optical paths for the measurements of two polarization states might introduce a systematic error; this puts a stringent requirement on the quality of the two optical paths in the experimental setup. It also requires a larger area of the detector to accommodate larger FOV.

Though the dual beam polarimetry is more advantageous than the single beam polarimetry for small FOVs, we preferred to use single beam setup to perform the polarization analysis over a larger FOV. The fast modulation scheme with Liquid crystal variable retarders along with a matching fast camera readout, enable us to complete the modulation cycle before the seeing changes significantly. We

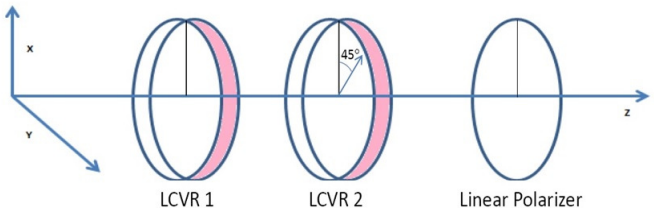

Figure 2.6: Schematic layout of the polarimeter for MAST. The fast axis of LCVR1 and LCVR2 are kept at 0° and 45° with respect to the linear polarizer.

plan to implement the dual beam spectropolarimetry with MAST at a later stage with a suitable large format camera and a polarizing beam displacer to mitigate seeing induced polarization effects which is necessary for weak magnetic fields measurements and high resolution observation.

The main components of the MAST polarimeter are LCVRs for polarization modulation and Glan-Thompson polarizer for analysis. Many of the modern polarization modulators use liquid crystals, in which retardance (as in nematic liquid crystals) or fast axis (as in ferroelectric liquid crystals) can be changed by applying voltages (Heredero et al. 2007, and references therein). These modulators allow us to implement fast modulation schemes by avoiding mechanical motions and beam wobble as in the case of rotating retarders (Heredero et al. 2007). Two sets of LCVRs along with a linear polarizer are used for obtaining the Stokes parameters in MAST. LCVRs for MAST polarimeter are custom made nematic liquid crystal devices with an aperture size of 80 mm, procured from Meadowlark Optics, USA. Figure 2.6 shows the schematic of MAST polarimeter. The fast axis of LCVR1 and LCVR2 are fixed at 0° and 45° with respect to the linear polarizer (LP), respectively. Light from the telescope enters through the LCVR1, passes through the LCVR2 and exits from the LP. Both LCVRs and the LP are mounted on rotatable mounts to make the adjustment for the angles. The photograph of the installed system is shown in Figure 2.7. The temperature of the LCVRs is actively controlled using flexible heaters fixed on the holder; a temperature sensor in a closed loop provides a thermal stability of $\pm 1°C$.

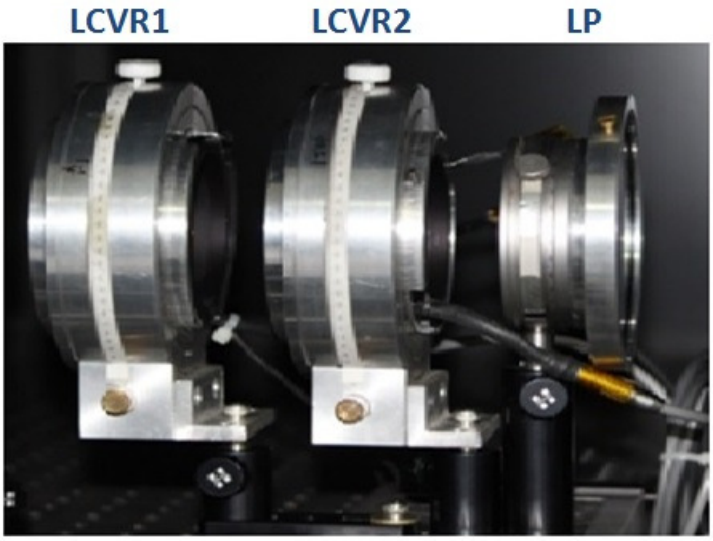

Figure 2.7: Imaging polarimeter for MAST at USO. From left to right LCVR1, LCVR2 and linear polarizer. The LCVR1 and LCVR2 are kept at 0° and 45° with respect to the linear polarizer (LP), respectively.

The modulation voltages for the LCVRs are supplied from a Meadowlark digital interface. The amplitude of the basic 2 kHz square waveform can be adjusted by an input DC voltage or counts provided from the software through a USB computer interface. Modulation voltages in the range of $0 - 10$ V with 16-bit accuracy can be applied to the LCVRs through this interface. Computer programs in C language have been written for the image acquisition to be synchronous with the modulation voltages. The modulation scheme employed here is described in the following subsection.

2.4.1 Modulation Schemes for the Measurement of Stokes Parameters

As discussed in the previous section, the MAST polarimeter consists of two LCVRs and a linear polarizer. The Stokes vector of input light (S_{in}) at LCVR1 and the Stokes vector of output light at LP (S_{out}), are related using Mueller-

matrix formalism by the following equation:

$$S_{out} = M_P M_{LC2}(\gamma, \theta_2) M_{LC1}(\delta, \theta_1) S_{in} = M_S S_{in} \tag{2.1}$$

where M_P, $M_{LC1}(\delta, \theta_1)$, and $M_{LC2}(\gamma, \theta_2)$ are the Mueller matrices of the linear polarizer, LCVR1 and LCVR2, respectively. The fast axis of LCVR1 and LCVR2 with respect to the transmission axis of the linear polarizer is represented by θ_1 and θ_2, respectively. The retardance of the LCVR1 and LCVR2 are given by δ and γ, respectively. M_S is the resultant Mueller matrix of the polarimeter for a particular value of δ, γ, θ_1, and θ_2.

The intensity I, measured at CCD, can be expressed as a linear combination of all the input Stokes parameters by using the Mueller matrix of the retarder and polarizer in the Equation 2.1.

$$I_j = S^0_{out} = 1S^0_{in} + a_j S^1_{in} + b_j S^2_{in} + c_j S^3_{in}, \tag{2.2}$$

where the parameters $[1, a_j, b_j, c_j]$ are the first row of M_S which depend on θ_1, θ_2, δ, and γ. Here j runs over the number of observations (from 1 to 'n'). From Equation 2.2, we can measure n number of intensities for different combinations of retardances and fast axis orientations of both the LCVRs. However, it is always preferred to have a minimum number of intensity measurements to infer all the Stokes parameters (del Toro Iniesta and Collados 2000). A minimum four measurements ($n \geq 4$) are needed for vector polarimetry whereas longitudinal polarimetry can be done with two measurements ($n \geq 2$) only. Therefore for n intensity measurements, a modulation scheme is fully characterized by a $(n \times 4)$ modulation matrix $\mathbf{O}$ built from the n first rows of M_S,

$$I_{meas} = \mathbf{O} S_{in}. \tag{2.3}$$

The Stokes vector is derived using the following Equation,

$$\mathbf{S}_{in} = \mathbf{O}^{-1}\mathbf{I}_{meas} = \mathbf{D}I_{meas}. \tag{2.4}$$

If n= 4, then $\mathbf{O}$ is a 4×4 matrix so its inverse will be unique. But, if $n = 6$ then $\mathbf{O}$ is 6×4 matrix, which is not a square matrix, and its inverse will not be unique. Hence, when D is not a square matrix, it is determined using the following Equation (del Toro Iniesta and Collados 2000),

$$\mathbf{D} = (\mathbf{O}^T\mathbf{O})^{-1}\mathbf{O}^T. \tag{2.5}$$

The efficiency of the modulation scheme is defined as,

$$e_i = (n\sum_{j=1}^{n}\mathbf{D}_{ij}^2)^{-1/2}, \tag{2.6}$$

where, e_1, e_2, e_3, and e_4 are the efficiencies for measuring the Stokes parameter I, Q, U, and V respectively.

For four measurement modulation scheme (n=4), the following equation applies:

$$I_{meas} = \begin{bmatrix} I_1 \\ I_2 \\ I_3 \\ I_4 \end{bmatrix} = \mathbf{O}\begin{bmatrix} S_{in}^0 \\ S_{in}^1 \\ S_{in}^2 \\ S_{in}^3 \end{bmatrix}, \tag{2.7}$$

where $\mathbf{O}$ is the modulation matrix given as,

$$\mathbf{O} = \begin{pmatrix} 1 & a_1 & b_1 & c_1 \\ 1 & a_2 & b_2 & c_2 \\ 1 & a_3 & b_3 & c_3 \\ 1 & a_4 & b_4 & c_4 \end{pmatrix}. \tag{2.8}$$

Table 2.1: Four measurement modulation scheme (Martinez Pillet et al. 2004) for vector polarimetry.

δ ($^\circ$)	γ ($^\circ$)	Measured Intensity I_{meas}
315.0	305.264	I_1=$I + Q/\sqrt{3} + U/\sqrt{3} + V/\sqrt{3}$
315.0	54.736	I_2=$I + Q/\sqrt{3} - U/\sqrt{3} - V/\sqrt{3}$
225.0	125.264	I_3=$I - Q/\sqrt{3} - U/\sqrt{3} + V/\sqrt{3}$
225.0	234.736	I_4=$I - Q/\sqrt{3} + U/\sqrt{3} - V/\sqrt{3}$

Table 2.2: Six measurement modulation scheme (Tomczyk et al. 2010) for vector polarimetry.

δ ($^\circ$)	γ ($^\circ$)	Measured Intensity I_{meas}
180.0	360.0	$I_1 = I + Q$
180.0	180.0	$I_2 = I - Q$
090.0	090.0	$I_3 = I + U$
090.0	270.0	$I_4 = I - U$
180.0	090.0	$I_5 = I + V$
180.0	270.0	$I_6 = I - V$

Orientation of the fast axis of LCVR1 and LCVR2 is fixed at $\theta_1 = 0^\circ$, and $\theta_2 = 45^\circ$, respectively (Martinez Pillet et al. 2004) for the polarimeter configuration shown in Figure 2.6.

Four and six measurement modulation schemes are implemented for vector polarimetry at MAST using different combinations of retardances of LCVR1 and LCVR2, *i.e.*, δ and γ. The modulation schemes of four and six measurements are listed in Table 2.1 and 2.2.

O for the four measurement modulation scheme is given by,

$$\mathbf{O} = \begin{pmatrix} 1 & 0.57735 & 0.57735 & 0.57735 \\ 1 & 0.57735 & -0.57735 & -0.57735 \\ 1 & -0.57735 & -0.57735 & 0.57735 \\ 1 & -0.57735 & 0.57735 & -0.57735 \end{pmatrix}. \tag{2.9}$$

For this modulation scheme, the maximum efficiencies are determined from Equations 2.5 and 2.6 as $e_1 = 1$, $e_2 = 0.57735$, $e_3 = 0.57735$, and $e_4 = 0.57735$.
Similarly, the modulation matrix for six measurement modulation scheme can be expressed as a 6×4 matrix,

$$\mathbf{O} = \begin{pmatrix} 1 & 1 & 0 & 0 \\ 1 & -1 & 0 & 0 \\ 1 & 0 & 1 & 0 \\ 1 & 0 & -1 & 0 \\ 1 & 0 & 0 & 1 \\ 1 & 0 & 0 & -1 \end{pmatrix}. \tag{2.10}$$

For this modulation scheme, the maximum efficiencies are determined as $e_1 = 1$, $e_2 = 0.57735$, $e_3 = 0.57735$, and $e_4 = 0.57735$. These are the maximum efficiencies that an ideal polarimeter system can have (del Toro Iniesta and Collados 2000).
Both the modulation schemes provide equal modulation efficiencies for the measurement of Q, U, and V (Del Toro Iniesta and Martínez Pillet 2012). Either of these modulation schemes can be used for the measurement of all the Stokes parameters in vector polarimetry. Measurement of all the Stokes parameters is required to obtain the vector magnetic field, whereas the longitudinal magnetic field can be obtained from Stokes I and V only.

Table 2.3: Modulation scheme for longitudinal polarimetry

δ ($^\circ$)	γ ($^\circ$)	Measured Intensity I_{meas}
360.0	90.0	$I_1 = I - V$
360.0	270.0	$I_2 = I + V$

The modulation scheme for longitudinal polarimetry is listed in Table 2.3. The relation between the incoming Stokes vector and measured Stokes vector is given as (Beck et al. 2005),

$$S_{meas} = \mathbf{X}.S_{in}, \tag{2.11}$$

where $\mathbf{X}$ is the 4×4 square matrix known as response matrix which includes all the processes for polarimetric measurement such as properties of optical components, modulation schemes and their demodulation (de Juan Ovelar et al. 2014; Beck et al. 2005). Furthermore, $\mathbf{X}$ can be expressed as

$$\mathbf{X} = \mathbf{DO}. \tag{2.12}$$

In the response matrix of an ideal polarimeter, the diagonal elements will be unity and the off-diagonal elements will be zero. However, in practice off-diagonal element of the response matrix will have non-zero values representing the cross-talk between the Stokes parameters introduced due to several reasons (de Juan Ovelar et al. 2014). All these factors are discussed in chapter 4.

2.5 Summary

Multi-Application Solar Telescope (MAST) is an off-axis Gregorian telescope of 50 cm clear aperture situated on an island in the Fateh Sagar lake at Udaipur Solar Observatory (USO). An imaging based spectropolarimeter has been devel-

oped at USO as a back-end instrument of MAST for measuring the magnetic and velocity fields in the photosphere and chromosphere at two different heights. The spectropolarimeter consists of a narrow-band imager and a polarimeter. Narrow-band imager uses two lithium niobate Fabry-Perot etalons in tandem with a blocking filter for spectral analysis. Polarimeter yields simultaneously the polarization state of light in two magnetically sensitive spectral lines at 6173 Å and 8542 Å. The polarization measurement is performed with two LCVRs, which modulates the incoming polarization. The modulated light is transformed into a varying intensity by using a Glan-Thompson polarizer. These intensities can be demodulated to obtain all the Stokes parameters using an efficient four or six measurement modulation scheme. The line-of-sight measurement can be performed with two intensities measurements only. The observed Stokes profiles will be inverted using an inversion code to infer the magnetic and thermodynamic properties of the solar atmosphere for the particular spectral line. Thus, the characterization of the all the optical components of the polarimeter is very important in order to achieve better polarimetric accuracy. In the next chapter, we discuss the characterization of the polarimeter components.

Chapter 3

Characterization of the polarimeter components

3.1 Introduction

From the previous chapter, we note that LCVR is the main component of the polarimeter. Therefore accurate information about retardance of the LCVR is important for polarimetric measurements. The retardance of LCVR mainly depends on the applied voltage but it also depends on temperature for a fixed wavelength. The characterization of each LCVR is important in order to get the accurate retardance for better polarimetric accuracy. In this chapter, I will briefly describe the properties of the LCVRs, the experimental setup which we have used for their characterization, and the results obtained from the experiments.

3.1.1 Liquid Crystal Variable Retarder

LCVR is made of nematic liquid crystal which is a phase of matter whose physical properties lie between liquids and solids. Nematic liquid crystals have long cigar-shaped molecules which can move almost similar to the ones in ordinary liquids but they tend to be more or less parallel to the substrate, even though their

positions are fairly random. To make them behave as variable retarders, we are using their two important properties: optical anisotropy which makes them form uniaxial birefringent layers, and electrical anisotropy which makes their optical properties tunable. Figure 3.1 shows a sketch of this behaviour of the liquid crystal molecules in the absence of the electric field (Figure 3.1, left) and in the presence of electric field (Figure 3.1, right).

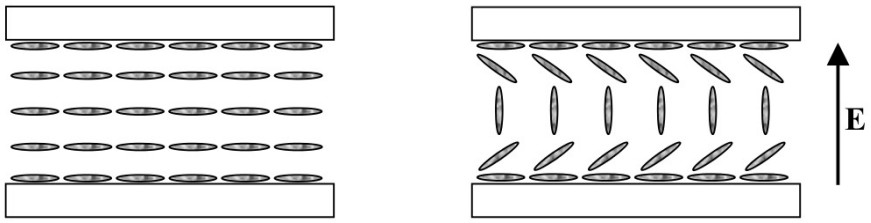

Figure 3.1: Sketch of nematic liquid crystal molecules without electric field (left) and with electric field (right). Courtesy: Jochum et al. (2003).

The retardance δ introduced by a layer of liquid crystals is determined using the relation,

$$\delta = 2\pi.\Delta n.\frac{d}{\lambda} \quad , \quad \Delta n = (n_0 - n_e) \tag{3.1}$$

Here, d is the layer thickness, λ is the wavelength and Δn is the birefringence coefficient, which is the difference between the refractive index of the ordinary and extraordinary beam.

Without an electric field, the molecules are aligned with their long axis parallel to the substrate surfaces. If an electric field is applied to the liquid crystal layer, the molecules will tilt by an angle θ until the long axis of the molecules is parallel to the field direction for strong fields (see Figure 3.2).

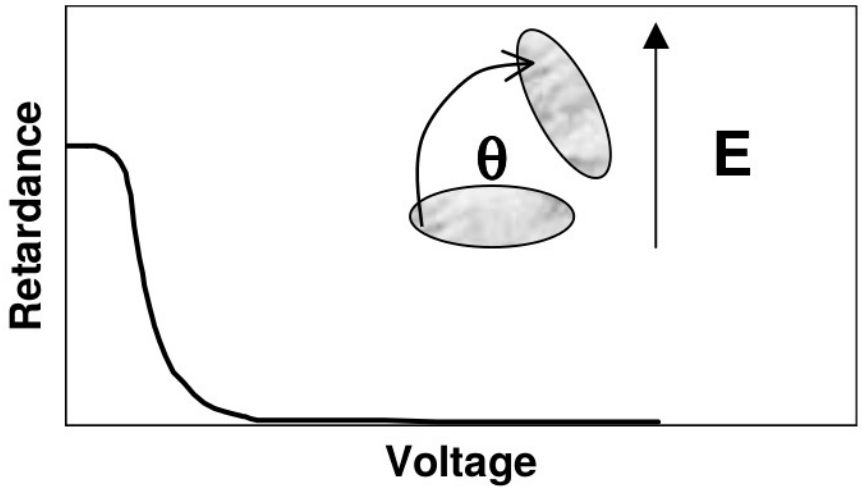

Figure 3.2: Changes of retardance with increasing E-field. Courtesy: Jochum et al. (2003).

3.2 Characterization of LCVRs

3.2.1 Theory

The states of matter whose symmetric and mechanical properties are intermediate between those of a crystalline solid and an isotropic liquid are called "liquid crystal". The most fundamental characteristic of a liquid crystal is the presence of long-range orientational order while the positional order is either limited (smectic phases) or absent altogether (nematic phases). One phase differs from the other with respect to its symmetry (de Gennes et al. 1995). The transition between different phases corresponds to the breaking of the symmetry and can be described in terms of order parameter (S), which describes the phase transition. The order parameter S is defined as

$$S = \langle \frac{3}{2} cos^2\theta - \frac{1}{2} \rangle \tag{3.2}$$

where θ represents the angle between the main axis of a particular molecule and the average orientation of all molecules, and $\langle\rangle$ symbolizes an average over the entire system. Here, S=1 corresponds to a perfectly aligned liquid crystal, and S=0 to an isotropic state (De Gennes 1969).

It is well known that S decreases with temperature and that, near the nematic-isotropic transition temperature (T_c), it drops non-continuously to zero. This behavior with temperature can be understood as when the molecules gain energy they can depart more, from order than at lower temperatures, due to combined effects of entropy and energy. Considering this, Haller has shown the order parameter can be described over the entire nematic temperature range by the following relation (Haller 1975).

$$S = \left(1 - \frac{T}{T_C}\right)^{\beta} \tag{3.3}$$

Where, β is a critical exponent related to the phase transition. β also has a dependence on the birefringence, which in turn depends on the applied voltage. This shows that the order parameter also depends on the applied voltage.

Liquid crystal devices such as LCVR are used for the modulation of the input beam by changing the retardance by the application of voltage. In the absence of applied voltage, LCVR produces maximum retardance as the director (long axes of the liquid crystal molecules) of the liquid crystal is parallel to the interfaces. The retardance would be low if all molecules are not aligned parallel to the interface. The retardance of the LCVRs can be tuned by applying voltages. The voltage dependence of retardance of LCVR is given by the following Equation (Saleh and Teich 2007),

$$\delta = \frac{2\pi d}{\lambda}\left[\left(\frac{sin^2(\Theta)}{n_o^2} + \frac{cos^2(\Theta)}{n_e^2}\right)^{-\frac{1}{2}} - n_e\right], \tag{3.4}$$

where, n_o and n_e are the refractive indices of the ordinary and extraordinary beam and the equilibrium tilt angle Θ for liquid crystal molecules depends on the applied voltage, which is described by

$$\begin{aligned}\Theta &= 0, \ \forall \ V \leq V_C \\ &= \frac{\pi}{2} - 2\tan^{-1}\left[\exp\left(-\frac{V - V_C}{V_0}\right)\right], \ \forall \ V > V_C,\end{aligned}$$

where, V is the applied voltage, V_C is the critical voltage at which the tilting process begins, and V_0 is a constant.

Retardance and the order parameter are related by the equation (Capobianco et al. 2008)

$$\begin{aligned} \delta &= \delta_0 S \\ &= \delta_0 \left(1 - \frac{T}{T_C}\right)^{\beta} \end{aligned} \tag{3.5}$$

where δ_0 is the retardance for S=1, T_C is the nematic-isotropic transition temperature, and β is a critical exponent related to the phase transition. As evident from the above equation, for a particular voltage as temperature increases, S and δ decreases. Thus, from the measurements of retardance as a function of voltage at different temperatures the behavior of S can be understood.

3.2.2 Experimental setup and procedure

Experimental setup for the characterization of LCVRs is shown in Figure 3.3. We have used a stabilized DC lamp as a white light source (S) along with a diffuser to get uniform intensity. A lens (C1) is placed in front of the pinhole to collimate the light. An interference filter (F1) is used to select the particular wavelength for which characterization of the LCVRs is carried out. The LCVR is placed in between two Glan-Thompson polarizing prisms (P1 & P2). Glan-Thompson polarizing prisms offers high extinction ratio (1×10^{-6}) and high transmittance for a wavelength band between 3500-23000 Å (Hecht 2001). Another lens (C2) is placed after the analyzer (P2) to image the beam onto a CCD camera to measure the intensity of output light. The incoming light is linearly polarized by the polarizer P1. After being retarded by the LCVR, with its fast axis at 45°, the light is analyzed by the second polarizer P2. Polarizer P2 is mounted on a computer controlled rotation stage to measure the intensities at two different

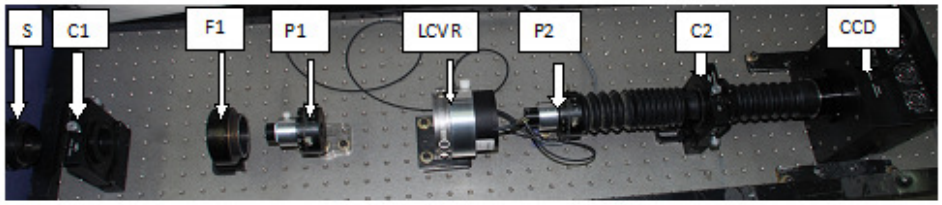

Figure 3.3: Experimental setup for the calibration of LCVRs: In this setup, a light beam coming from a pinhole source is collimated using a lens C1. Then the collimating light passes through an interference filter (F1), linear polarizer (P1) and LCVR whose fast axis is kept at 45° with respect to P1. Finally, light is imaged by imaging lens (C2) on CCD which is placed in the focal plane of the imaging lens after passing through analyzer P2.

orientations.

The Stokes vector S_{out} after P2 can be written as

$$S_{out} = M_{POL} M_R(\delta) S_{in}, \tag{3.6}$$

where $S_{in} = [1\ 1\ 0\ 0]^T$ represents the light linearly polarized by the polarizer P1. $M_R(\delta)$ and M_{POL} are the Mueller matrix for the LCVR and the polarizer P2, respectively. $M_R(\delta)$ and M_{POL} can be written as

$$M_R(\delta) = \begin{pmatrix} 1 & 0 & 0 & 0 \\ 0 & cos^2 2\phi + sin^2 2\phi cos\delta & sin2\phi cos2\phi(1 - cos\delta) & -sin2\phi sin\delta \\ 0 & sin2\phi cos2\phi(1 - cos\delta) & sin^2 2\phi + cos^2 2\phi cos\delta & cos2\phi sin\delta \\ 0 & sin2\phi sin\delta & -cos2\phi sin\delta & cos\delta \end{pmatrix}. \tag{3.7}$$

$$M_{POL}(\theta) = \frac{1}{2} \begin{pmatrix} 1 & cos2\theta & sin2\theta & 0 \\ cos2\theta & cos^2 2\theta & sin2\theta cos2\theta & 0 \\ sin2\theta & sin2\theta cos2\theta & sin^2 2\theta & 0 \\ 0 & 0 & 0 & 0 \end{pmatrix}. \tag{3.8}$$

where ϕ is the orientation of the fast axis of the LCVR with respect to P1, δ is the retardance of LCVR due to the voltage applied, and θ is the orientation angle

of P2 with respect to P1.

Substituting M_R, M_{POL} and S_{in} in Equation 3.6, the output intensity (I_{out}) measured by the CCD is

$$I_{out} = \frac{1}{2}\left[1 + cos2\theta(cos^2 2\phi + sin^2 2\phi cos\delta) + sin2\theta sin2\phi cos2\phi(1 - cos\delta)\right]. \quad (3.9)$$

In our setup, we always keep ϕ=45°. Hence, Equation 3.9 becomes

$$I_{out} = \frac{1}{2}\left[1 + cos2\theta cos\delta\right]. \quad (3.10)$$

For $\theta = 0°$, P2 is parallel to P1, output intensity is

$$I^0_{out} = \frac{1}{2}\left[1 + cos\delta\right]. \quad (3.11)$$

For $\theta = 90°$, P2 is crossed to P1, the output intensity is

$$I^{90}_{out} = \frac{1}{2}\left[1 - cos\delta\right]. \quad (3.12)$$

Using Equations 3.11 and 3.12, retardance of LCVR can be obtained as

$$\delta = cos^{-1}\left(\frac{I^0_{out} - I^{90}_{out}}{I^0_{out} + I^{90}_{out}}\right). \quad (3.13)$$

Rotating the polarizer P2 provides two angles for θ, viz. θ=90° and θ=0°. Thus, by measuring the intensities I_{out} for the two different angles, $\theta = 90°$ and $\theta = 0°$, the retardance δ of the LCVR can be estimated for different voltages. However, it requires prior knowledge of the transmission axis of the polarizers and the fast axis of the LCVR. Hence, we determined the transmission axis of the polarizers and the fast axis of the LCVR using the same experimental setup before we carried out the characterization of LCVR.

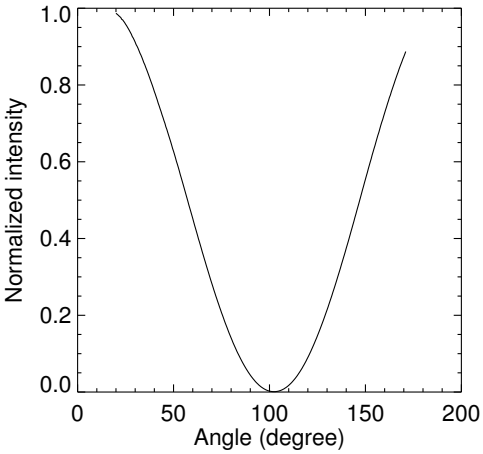

Figure 3.4: Variation of intensity with the rotation of polarizer P2 with respect to polarizer P1. The minimum intensity gives the angle at which both the polarizers are crossed to each other.

3.2.3 Determination of the transmission axis of the polarizers

The LCVR, shown in Figure 3.3, is removed from the optical path in order to precisely align the axis of the polarizers P1 and P2. By keeping the polarizer P1 at a fixed position, the polarizer P2 is rotated from 0° to 180° with respect to P1, with a step size of 0.5° using a computer controlled rotation stage (least count of the computer controlled rotating mount is 0.5°). For each angle, the intensity is measured using the CCD. The plot of the measured intensity as a function of the angle is shown in Figure 3.4. The intensity is maximum when P1 and P2 are in parallel position. The intensity starts decreasing with an increase in the angle between them. We get the minimum intensity at the crossed position which further starts increasing with an increase in the angle between P1 and P2. From the Figure 3.4, the angle of polarizer or analyzer P2 is obtained at (90±0.5)°. Therefore the transmission axis of the polarizer P1 is (0±0.5)°. The above result

satisfies the following equation,

$$M_{P2}(\theta = 90^\circ).M_{P1}(\theta = 0^\circ) = 0.$$

3.2.4 Determination of the fast or slow axis of LCVR

After knowing the crossed position of the polarizers P1 and P2, we proceed to determine the fast axis of the LCVR. For this purpose, the polarizers P1 and P2 are kept in crossed position and the LCVR is again placed between them. After that, the output intensity is measured by rotating the LCVR. Figure 3.5 shows the plot between measured intensity and angle of the LCVR with respect to P1. The angle at which minimum intensity is observed is the angle at which fast axis of LCVR is parallel to P1 or perpendicular to polarizer P2. The above procedure can be easily understood by solving the following Mueller matrix Equation,

$$M_{P2}(\theta = 90^\circ).M_{LCVR}(\phi = 0^\circ, \delta).M_{P1}(\theta = 0^\circ) = 0.$$

We rotate the fast axis of the LCVR by (45±0.5)° from this position for further characterization of the LCVR.

3.2.5 Characterization of LCVRs with voltage

After knowing the crossed position of polarizers and the fast axis of LCVRs, we moved to characterize the dependence of voltage on the retardance of the LCVRs using the following procedure. Keeping the polarizers P1 and P2 in crossed position and the fast axis of the LCVR at 45° with respect to P1, we applied voltages from 0 to 10 V in steps of 0.05 V to the LCVR. Five images were taken at each voltage and the mean intensity was computed to obtain I^{90}_{out}. Following the same procedure, we obtained I^{0}_{out} as a function of voltage after rotating P2 such that P1 and P2 are in parallel position. In both the cases, the temperature

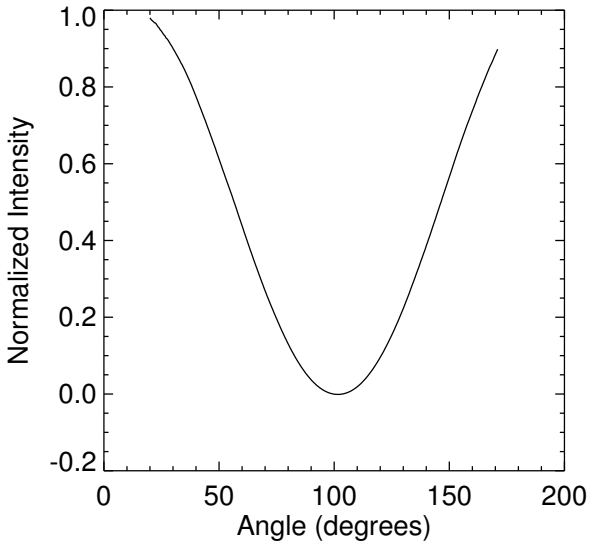

Figure 3.5: Variation of intensity with the rotation of the fast axis of LCVR. The minimum intensity gives the position where the fast axis of LCVR is parallel with the polarizer P1.

of LCVR is kept constant at 28°C.

With the measured I^0_{out} and I^{90}_{out} at each voltage, the retardance is calculated using Equation 3.13. The retardance of LCVRs (LCVR1 and LCVR2) with voltage for 6173 Å and 8542 Å are shown in Figure 3.6 and 3.7, respectively. The characteristic plots between retardance and voltage are used to estimate the voltages required in both the modulation schemes (vector and longitudinal). Figures 3.6(a) and 3.6(c) represent the corresponding voltages required for the retardance

Table 3.1: Derived voltages for the required retardance at 6173 Å in the vector field mode modulation scheme for both the LCVRs.

δ_1 (°)	Voltage of LCVR1 (V)	δ_2 (°)	Voltage of LCVR2 (V)
315.0	2.098±0.001	305.264	2.273±0.001
315.0	2.098±0.001	054.736	5.048±0.001
225.0	2.598±0.001	125.264	3.615±0.001
225.0	2.598±0.001	234.736	2.651±0.001

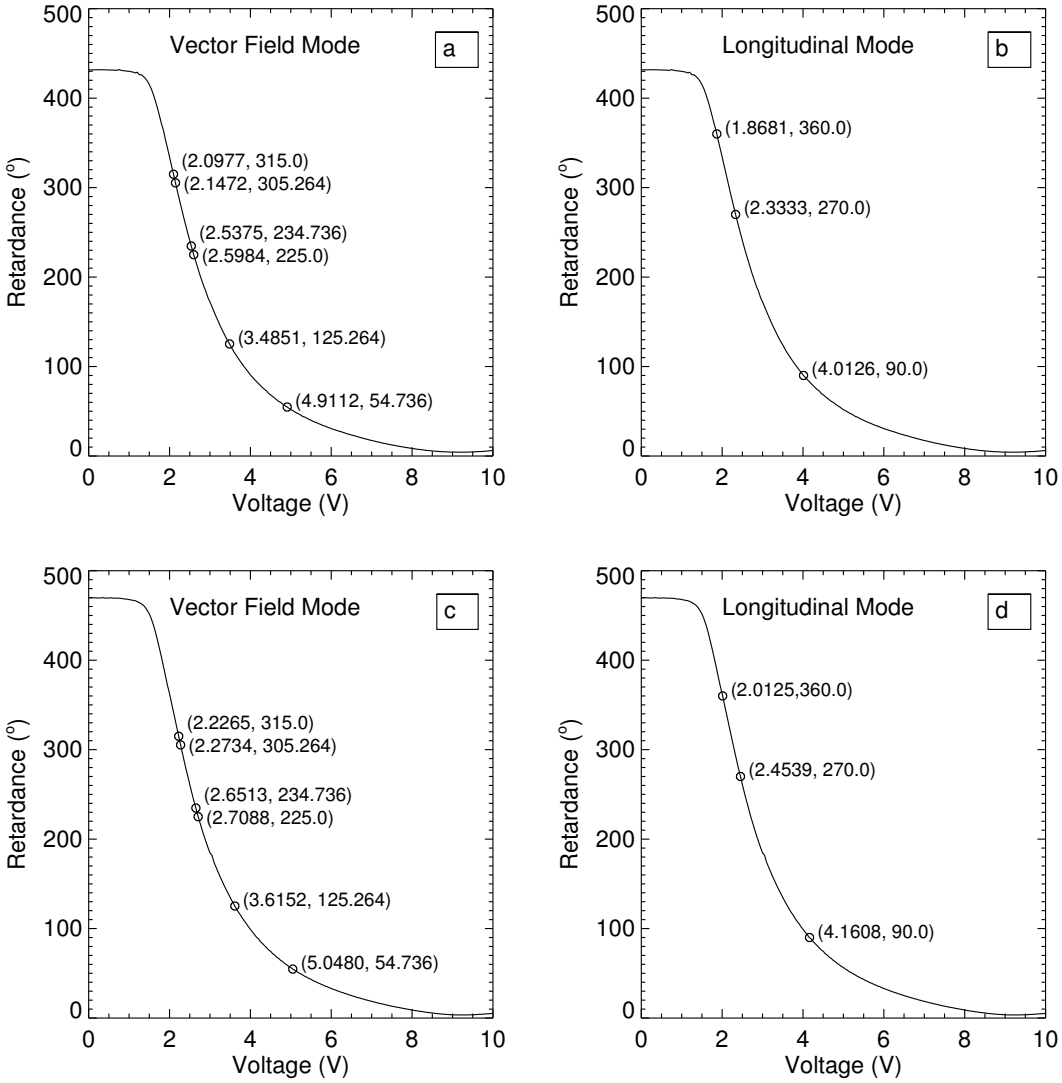

Figure 3.6: Calibration curves of the LCVR1 (top panels) and LCVR2 (bottom panels) at 6173 Å showing retardance as a function of voltage. Left (a and c) and right (b and d) panels show the voltages for the required retardance in vector and longitudinal modes, respectively. Vector mode will be used for the measurement of all the Stokes parameters and longitudinal mode will be used only for measuring Stokes parameters I and V.

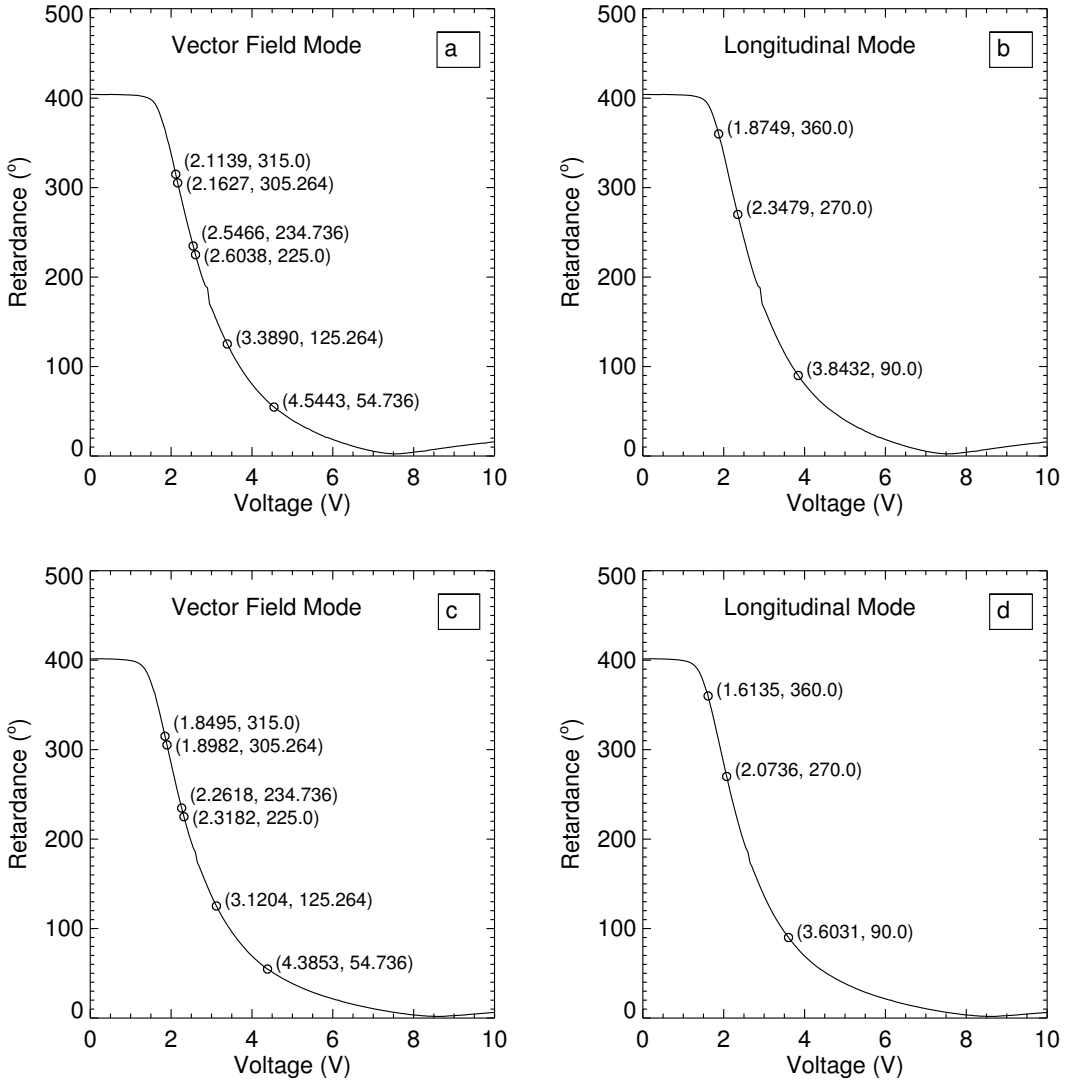

Figure 3.7: Calibration curves of the LCVR1 (top panels) and LCVR2 (bottom panels) at 8542 Å showing retardance as a function of voltage. Left (a and c) and right (b and d) panels show the voltages for the required retardance in vector and longitudinal modes, respectively. Vector mode will be used for the measurement of all the Stokes parameters and longitudinal mode will be used only for measuring Stokes parameters I and V.

Table 3.2: Derived voltages for the required retardance at 6173 Å in the longitudinal mode modulation scheme for both the LCVRs.

δ_1 (°)	Voltage of LCVR1 (V)	δ_2 (°)	Voltage of LCVR2 (V)
360.0	1.868±0.001	090.00	4.161±0.001
360.0	1.868±0.001	270.00	2.454±0.001

Table 3.3: Derived voltages for the required retardance at 8542 Å in the vector field mode modulation scheme for both the LCVRs.

δ_1 (°)	Voltage of LCVR1 (V)	δ_2 (°)	Voltage of LCVR2 (V)
315.0	2.114±0.001	305.264	1.898±0.001
315.0	2.114±0.001	054.736	4.385±0.001
225.0	2.604±0.001	125.264	3.120±0.001
225.0	2.604±0.001	234.736	2.262±0.001

in vector mode modulation scheme (shown by circle on the characteristic curve) and Figures 3.6(b) and 3.6(d) represent the corresponding voltages required for the retardance in longitudinal mode modulation scheme for LCVR1 and LCVR2 at wavelength 6173 Å, respectively. Similarly, panels (a) and (c) of Figure 3.7 represent corresponding voltages required for the retardance in vector mode modulation scheme and panels (b) and (d) of Figure 3.7 depict corresponding voltages required for the retardance in longitudinal mode modulation scheme for LCVR1 and LCVR2 respectively at wavelength 8542 Å.

The retardance and their corresponding voltages calibrated from Figures 3.6 and 3.7 are listed in Table 3.1-3.4 for both the LCVRs according to their respective wavelengths. These values are used for the measurement of Stokes parameters with the polarimeter for MAST.

Table 3.4: Derived voltages for the required retardance at 8542 Å in the longitudinal mode modulation scheme for both the LCVRs.

δ_1 (°)	Voltage of LCVR1 (V)	δ_2 (°)	Voltage of LCVR2 (V)
360.0	1.875±0.001	090.00	3.603±0.001
360.0	1.875±0.001	270.00	2.074±0.001

3.2.6 Characterization of the LCVRs with temperature

Noticeably, equation 3.5 shows that the temperature also influences the retardances of LCVRs. Therefore, we have characterized voltage dependence of retardance of a LCVR at four different temperatures, *i.e.*, 28°C, 30°C, 35°C, and 40°C. Retardance estimated with the application of voltage at a T = 28°C is shown in Figure 3.8. Left and right panels of Figure 3.8 show the retardance without phase-unwrapping and with phase-unwrapping, respectively. Here, it is to be noted that left panel of the Figure 3.8 show two regions, R1 and R2, which need phase-unwrapping for continuous curve. As the retardance required for polarimetry is in the range of 50-360°, we have not performed the phase unwrapping in the higher voltage range (R2), where the retardances are very small. For comparison, data obtained from the manufacturer is also shown in Figure (3.8, right). From the figure it is evident that our measurement is in agreement with that of manufacturer's. However, the minor difference observed in the both the curves is due to change in the wavelength of the light used. Our measurements are performed for a light of wavelength centered at 6173 Å, whereas the data provided by the manufacturer used 6302 Å wavelength.

Figure 3.9 shows the retardance as a function of voltage at different temperatures. As evident from the Figure 3.9 (left), retardance of the LCVR decreases as their temperature increases. At lower voltages (0-2 V), the applied electric field may not be sufficient enough to provide the torque to change the orientation of liquid crystal molecules so it remains parallel to the interfaces, here temperature influence is dominant. However, at higher voltages (V >6 V), torque due to the applied electric field is strong enough to not to influenced by the temperature, i.e., change in retardance due to voltage is dominant than the change in retardance due to temperature. In the intermediate regime (2-6 V), both temperature and voltage play a role in changing the retardance. The effect of temperature on the retardance of the LCVR can be clearly seen in the right panel of Figure 3.9.

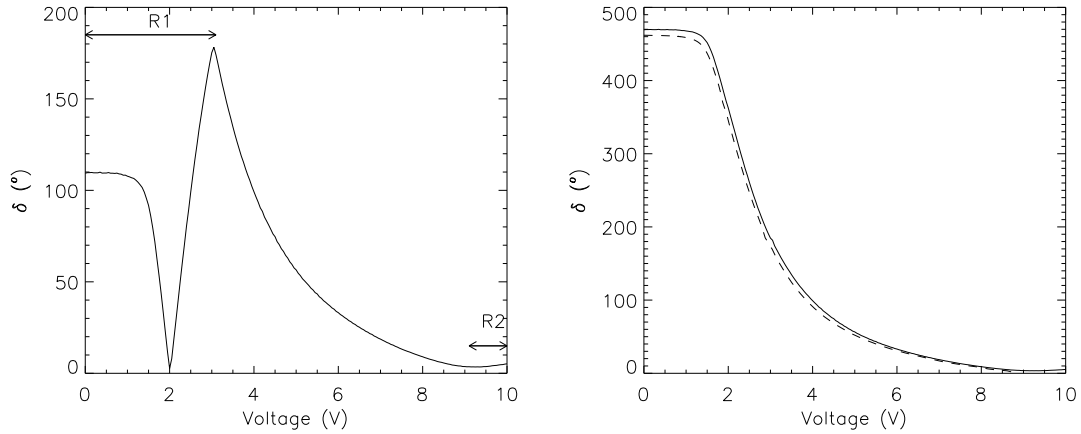

Figure 3.8: **Left:** Retardance vs voltage applied to a LCVR for a wavelength of 6173 Å. Measurements were made in steps of 0.05 V from 0 to 10 V. **Right:** Comparison between the curve provided by the manufacturer (dashed line) of the LCVR and that obtained with our procedure (continuous line). It is evident from the Figure that our measurement is in agreement with that of manufacturer's. However, the minor difference observed in the both the curves is due to change in the wavelength of the light used. Our measurements are performed for a light of wavelength centered at 6173 Å, where as the data provided by the manufacturer is for 6302 Å.

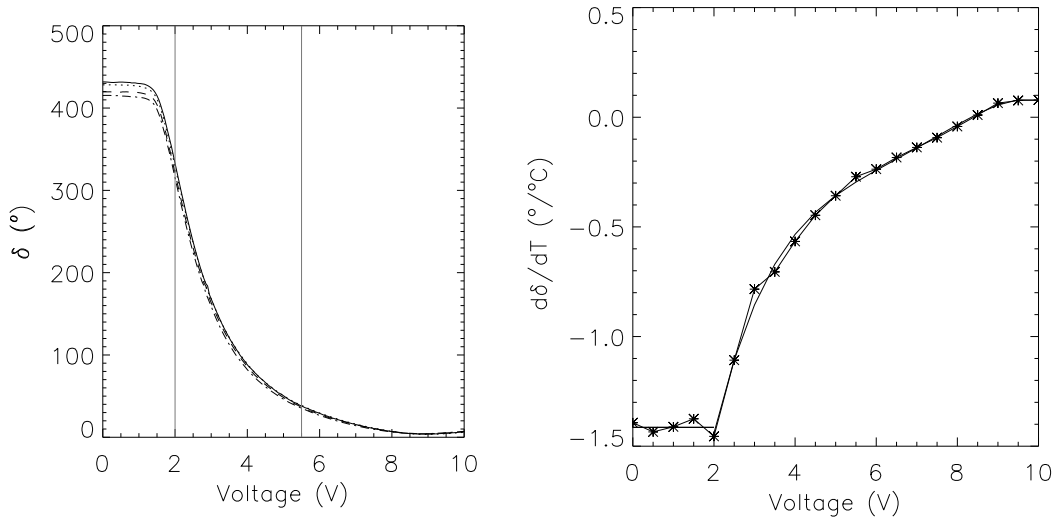

Figure 3.9: **Left:** Variation of the retardance with the applied voltage of LCVR for four different temperatures. Continuous, dotted, dashed and dot-dashed curves are corresponding to temperatures, 28°C, 30°C, 35°C, and 40°C, respectively. Vertical line represents different voltage regimes in which influence of voltage and temperature on retardance varies. **Right:** retardance derivative with respect to the temperature as a function of voltage which shows that LCVR is insensitive to temperature for higher voltages. Thin line with asterisk symbols represents $d\delta/dT$ derived using the data shown in the left panel and the polynomial fit is shown with thick line. This Figure is re produced from Tiwary et al. (2017b).

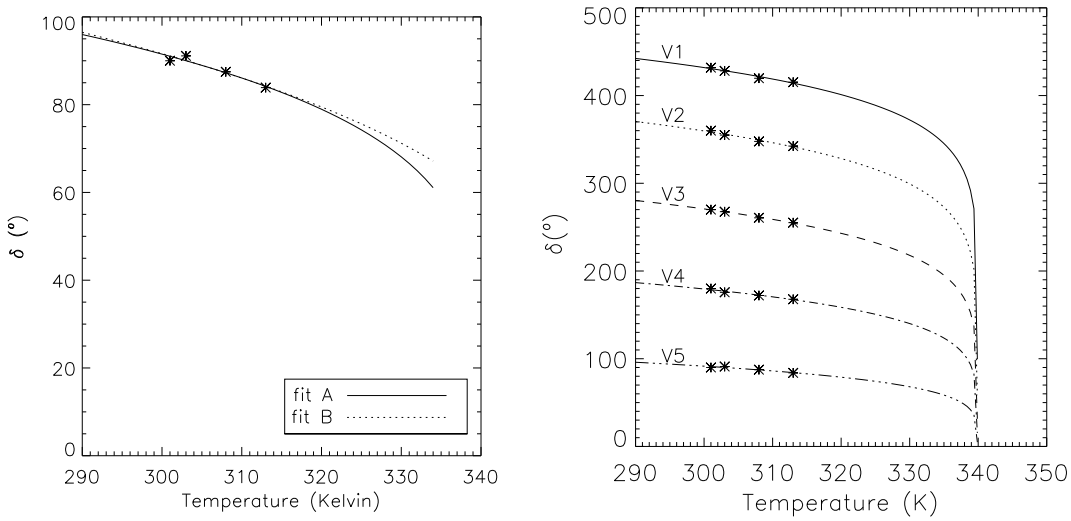

Figure 3.10: **Left:** Temperature Vs. retardance keeping the LCVRs at a voltage corresponding to quarter wave plate (V=3.967 V). Asterisk symbols shows the experimental data and the cuves show the corresponding fits using the two methods (Fit A and Fit B). For Fit A, temperature is fixed at 368 K. For Fit B, all the three parameters are varied to fit the equation 3.5. **Right:** Retardance versus temperature for different voltages: V1=0.0, V2=1.861, V3=2.318, V4=2.918, and V5=3.967 V at a constant T_C**=339.9** K. These voltages corresponds to retardance of maximum, λ, $3\,\lambda/4$, $\lambda/2$, and $\lambda/4$, respectively.

It shows that the LCVR is more sensitive to the temperature when it is operated at low voltages and it is nearly constant in the voltage range 0-2 V.

A relation between temperature sensitivity ($d\delta/dT$) and voltage is obtained for two regions of voltage separately using polynomial fit of the order 1 and 4, respectively. When we fit the entire data with a polynomial fit, the chi-square value is higher. Hence, the data is divided into two regimes (V$\leq$2 and 2<V>10) and used to find an appropriate polynomial fits as shown below.

$$\begin{aligned} \frac{d\delta}{dT} &= -1.41 \quad \forall\, V \leq 2 \\ \frac{d\delta}{dT} &= -4.03 + 1.97\,V - 0.41\,V^2 + 0.04V^3 - 0.0014V^4 \\ &\qquad\qquad \forall \quad 2 < V < 10 \end{aligned} \tag{3.14}$$

Using the equation 3.5, it can be shown that,

$$\frac{dS}{dT} = \frac{1}{\delta_0}\frac{d\delta}{dT} \tag{3.15}$$

The above equation shows that, in order to know the sensitivity of the order parameter (S), it is important to know the δ_0, which depends on the applied voltage. Hence, δ_0 and β are estimated by re-arranging the experimental data as shown in Figure 3.10.

The asterisk symbols in the left panel of Figure 3.10 depict the temperature dependence of the retardance at a fixed voltage 3.967 V (voltage corresponding to quarter wave retardance). The data (temperature Vs. retardance) is fitted to Equation 3.5 in two ways: one in which T_C is fixed at a known value of 368 K (95°C, provided by the manufacturer of LCVR, M/s Meadowlark optics) for this particular LCVR (fit A) and another in which all the parameters are (fit B) obtained from the fit. Fit A yields β=0.395±0.086 and δ_0=178.5±27.4. β value obtained here is more than the expected (Haller 1975). However, a better fit is achieved in the second method, which yields β=0.213±0.004, δ_0=144.1±1.3, and T_C=339.9±1.6 K. As the percentage of deviation in the obtained parameter is smaller, we use the values β, δ_0 and T_C obtained here for further analysis. Using the derived value of T_C (339.9 K or 66.9°C) and the Equation 3, data shown in the Figure 3.10 (right) is extrapolated for retardance as a function of temperature at different voltages (cf. Figure 3.10). As the polarimeter uses voltages in the range of 0-4 V for achieving required retardance, we have shown only these five voltages in the plot.

Critical exponent (β) and maximum retardance δ_0 are also obtained for the voltage range 0-8 V using the equation 3.5 with T_C at 340 K. Figure 3.11 depicts the change in β (top left panel) and δ_0 (top right panel) with voltage along with the 1-σ error bars. Change in β shows larger error at higher voltages. This could be due to the temperature sensitivity of retardance, which is very low at

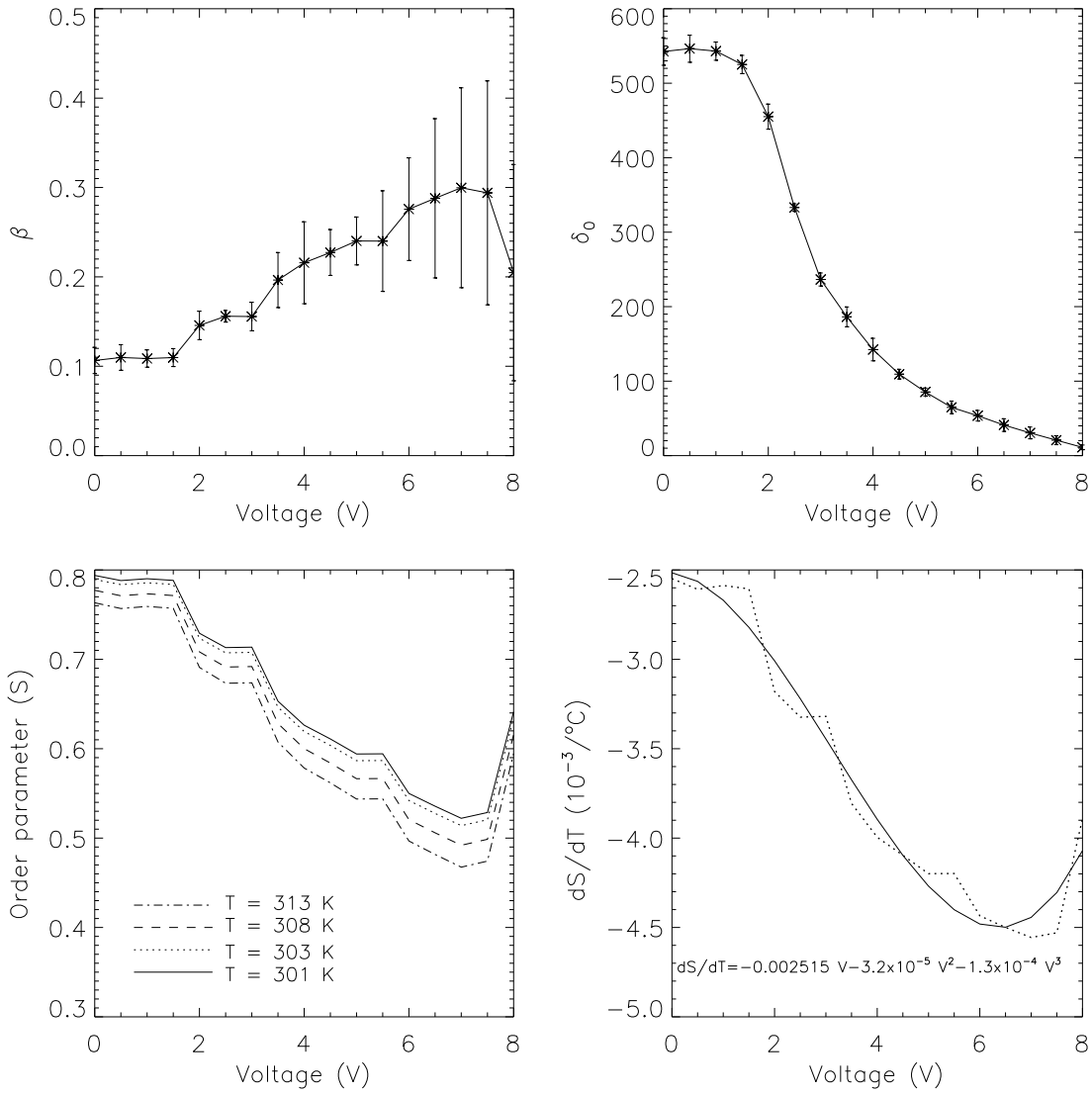

Figure 3.11: **Top Left:** Change in critical exponent (β) with voltage. **Right:** Change in δ_0 with voltage. The error bars corresponding to 1-σ error. **Bottom: Left** Change in order parameter (S) with voltage at different temperatures. **Right:** Change in order parameter (S) with respect to change in temperature (Tiwary et al. 2017a).

higher voltages (cf. Figure 3.9). Also β and δ_0 are almost constant in the low voltage regime (0-2 V). Lower panel of the Figure 3.11 shows the variation of order parameter at different temperatures and voltages and also change in the order parameter with respect to change in temperature.

The estimated order parameter varies between 0.45 and 0.8 for different combination of voltage and temperature and it decreases with an increase in temperature as well with an increase in voltage. It also shows that order parameter is more sensitive to voltage or the applied electric field than the temperature. $\frac{dS}{dT}$ shows linear relation (approximately) with voltage (V). The difference in obtained equations for $\frac{d\delta}{dT}$ and $\frac{dS}{dT}$ could be due to the voltage dependence of the δ_0 as seen in the top right panel of Figure 3.11. $\frac{dS}{dT}$ shows less complex behavior than the $\frac{d\delta}{dT}$. The complexity might have been normalized by the complex behavior of the voltage dependence of δ_0.

At present the LCVRs are kept in a temperature enclosure provided by the vendor. Temperature stability of the enclosure is ± 1°C. For precise polarimetric measurements, it is important to know the change in response matrix due to the fluctuations in the temperature enclosure. Maximum rate of change of the retardance with respect to the temperature is obtained (Figure 3.10) $\sim -1.5°/$°C at 2.0 V (Tiwary et al. 2017a). Thus, $\pm 1.0°$ C variation in temperature causes a maximum change in retardance of -1.5°. Incorporating the maximum change in retardance, the new response matrix can be written as,

$$\mathbf{X}' = \begin{pmatrix} 0.99983 & 0.00017 & 0.01309 & -0.01309 \\ 0.00017 & 0.99983 & -0.01309 & 0.01309 \\ -0.01309 & 0.01309 & 0.99983 & 0.00017 \\ 0.01309 & -0.01309 & 0.00017 & 0.99983 \end{pmatrix}. \tag{3.16}$$

Table 3.5: Polarimetric cross-talk due to change in the temperature stability (δT of the thermal control system.

δT (°C)	Q $\rightarrow$ U cross-talk	Q$\rightarrow$ V cross-talk	$U \rightarrow V$ cross-talk
1.00	1.3×10^{-2}	1.3×10^{-2}	1.7×10^{-4}
0.50	6.5×10^{-3}	6.5×10^{-3}	4.25×10^{-5}
0.25	3.2×10^{-3}	$3,2 \times 10^{-3}$	1.04×10^{-5}

Thus, the error in the measurement of response matrix is,

$$\Delta \mathbf{X} = \mathbf{X} - \mathbf{X}' = \begin{pmatrix} 0.00017 & -0.00017 & -0.01309 & 0.01309 \\ -0.00017 & 0.00017 & 0.01309 & -0.01309 \\ 0.01309 & -0.01309 & 0.00017 & -0.00017 \\ -0.01309 & 0.01309 & -0.00017 & 0.00017 \end{pmatrix},$$

where X is a unit matrix. The matrix elements (3, 2), (4, 2), (4, 3) of X' show the cross-talk among the Stokes parameters Q, U, and V. In this case, the cross-talk from Q to U and Q to V is same and equal to 1.3×10^{-2} and U to V cross-talk is 1.7×10^{-4}. We have calculated the change in cross-talk for different values of temperature accuracy. Table 3.5 summarizes the calculations. A temperature variation of ± 0.25°C (which can be obtained by optimizing the temperature control system) causes an error in retardance of $\pm 0.38°$ (as shown in Table 3.5). A cross-talk of the order of 10^{-3} would be acceptable for our scientific studies. Therefore a temperature control system which can maintain the temperature of LCVRs within ± 0.25°C will be constructed and used for the measurements of the Stokes parameters.

3.2.7 LCVRs: Change in the orientation of the fast axis with the voltage

It is presumed that the angular position of the LCVR fast axis is independent of the voltage, only the retardation changes according to the voltage. But in

practice, it was observed that the position of the fast axis also changes with the voltage (Terrier et al. 2010). In order to see the effect of voltage on the orientation of the fast axis of LCVR, we performed the following experiment. Two polarizers P1 and P2 are placed in a collimated beam keeping P1 at a reference position and intensity is measured by rotating P2 from $0° - 180°$. After knowing the crossed position of the polarizers P1 and P2, LCVR is placed between P1 and P2. The orientation of LCVR is adjusted such that the fast axis of LCVR becomes parallel to polarizer P1 (Figure 3.12). In this configuration, rotating the P2 gives exactly the same kind of intensity variation as in the case of linear polarizers without retarder. Without changing the orientation of the LCVR, we applied different voltages (between 0-10 V) to LCVR and measured the intensity variation by rotating P2. We observed that (Figure 3.12, left) the intensity variation continues to be sinusoidal, with the sinusoid pattern shifted with respect to the reference sinusoid (no LCVR). The difference between the reference position (no LCVR or without voltage) and the actual position for different voltages were measured and plotted against the applied voltage for LCVR1 (see Figure 3.12, right).

As shown in Figure 3.12 (right), the maximum shift obtained in the orientation of the fast axis of LCVR is 8° at 2.5 V. Thus, it is important to know the change in response matrix due to the shift in the orientation of fast axis. The new response matrix due to the change in the orientation of the fast axis (8°) is,

$$\mathbf{X}' = \begin{pmatrix} 0.99454 & 0.03327 & 0.05467 & -0.08248 \\ 0.03327 & 0.99454 & 0.05467 & -0.08248 \\ 0.30782 & -0.20404 & 0.92874 & -0.03252 \\ 0.30782 & -0.20404 & -0.03252 & 0.92874 \end{pmatrix}. \tag{3.17}$$

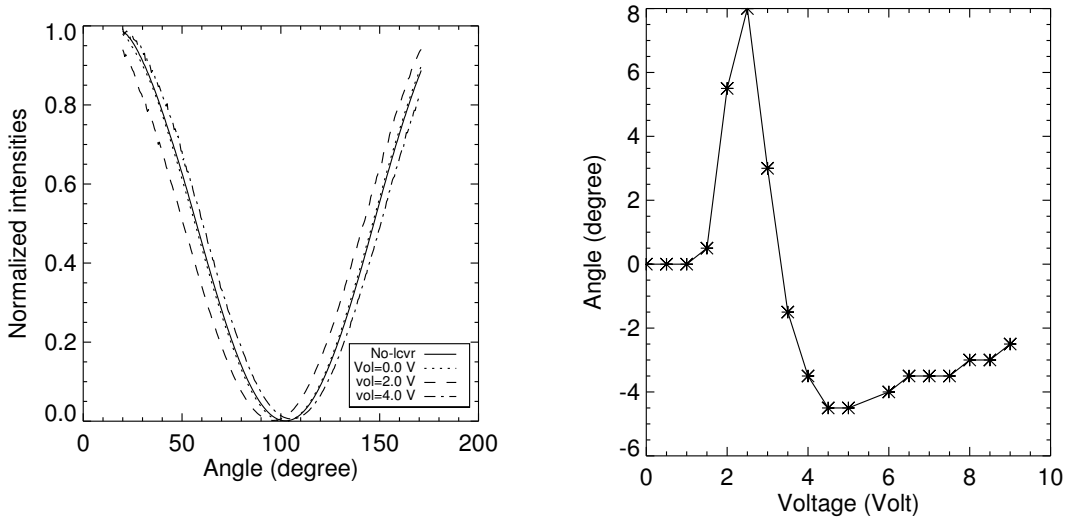

Figure 3.12: Left panel shows the variation of intensity with the change in angular position of polarizer P2 with reference to polarizer P1 for different voltages applied to the LCVR. The right panel shows the shift in the position of the fast axis with the voltage applied to the LCVR in which reference is taken as no LCVR position.

The error in the measurement of modulation matrix is,

$$\Delta\mathbf{X} = \mathbf{X} - \mathbf{X}' = \begin{pmatrix} 0.00546 & -0.03327 & -0.05467 & 0.08248 \\ -0.03327 & 0.00546 & -0.05467 & 0.08248 \\ -0.30782 & 0.20404 & 0.07126 & 0.03252 \\ -0.30782 & 0.20404 & 0.03252 & 0.07126 \end{pmatrix},$$

where X is unity matrix. The matrix elements (3, 2), (4, 2), (4, 3) of X' show the cross talk among the Stokes parameters Q, U, and V. In this case the cross-talk from Q to U and Q to V is same and equal to 2.0×10^{-1} and U to V cross-talk is 3.2×10^{-2}.

As evident from the above analysis the cross-talk in the Stokes measurement resulting from the drift in the LCVR fast axis while applying voltages is considerably large and needs to be taken into account. The theoretical modulation matrix O (as discussed in chapter 2) is modified by including the drift in the fast axis for corresponding voltages. This modified modulation matrix is used for the

demodulation of the observed Stokes profiles as shown by Terrier et al. (2010).

3.3 Summary

The main component of the polarimeter is LCVR which is made of nematic liquid crystals. In this chapter, we have studied the effect of several parameters on the retardance of the LCVR. We have derived the voltages required for the corresponding retardance in the modulation schemes by characterizing all the LCVRs in laboratory setup. The effect of temperature on the retardance of LCVR has been discussed. We also have described the effect of voltage on the orientation of the fast axis of LCVR. All these effects are very important for estimating the final polarimetric accuracy.

Chapter 4

Calibration of the polarimeter

A sensitive spectro-polarimeter is needed to study the magnetic structure of active regions and the small-scale magnetic elements. For polarimetric measurements, good signal-to-noise ratio (S/N) is also needed in relatively short timescales if we have to study the dynamics. Notably, the 50 cm aperture of MAST will provide enough photon flux to permit such studies. We need to calculate the S/N and exposure time at the detector to check whether a sufficient polarimetric sensitivity of ($\geq 0.1\%$) is achievable.

The need to overcome cross-talk effects owing to atmospheric seeing, to gain table uncertainties, or to instrumental polarization has driven the recent developments of new generation solar Stokes polarimeters. The major problem with solar polarimetry is the cross-talk between the components of the Stokes vector due to the oblique reflections in the telescope and any other instrumentation, including the polarimeter itself. In order to achieve better polarimetric accuracy, it is very important to calibrate the polarimetric properties of the telescope and the other optical components coming in the path of polarimeter. In this chapter, we discuss about polarimetric sensitivity and accuracy of the polarimeter.

4.1 Polarimetric sensitivity: Exposure time and Signal-to-noise (S/N)

Polarimetric sensitivity is defined as the noise level above which a real polarization signal can be measured. This is directly related with the S/N of the instrument. It can be calculated by using the reflectance and transmittance of all the optical components in the path of the beam. For MAST, the telescope has nine mirrors with 95 % reflectivity. Therefore the combined transmitted intensity of the beam coming out of the telescope and entering into the back-end instrument will be around 60%. After passing through the adaptive optics, the narrow-band imager and the polarimeter, the transmitted intensity is reduced to 5%. Thus the total number of photons per second (S) reaching to the detector is given by,

$$S = N_{\odot}\phi^2\Delta\lambda A_D T_{mast} \tag{4.1}$$

where $N_{\odot}$ is the number of photons coming from the Sun at 6173 Å per unit time, area, solid angle, and wavelength interval and its estimated value is

$$N_{\odot} = 8.125 \times 10^{18} photons\ cm^{-2} sec^{-1} sr^{-1} nm^{-1},$$

ϕ^2 represents the subtended angular area of the detector pixels on the plane of sky. $\Delta\lambda$ is the wavelength interval falling in one pixel (0.30 arcsec) and can be approximated by the spectral resolution of the instrument $\delta\lambda$ (FWHM≈95 mÅ). A_D is the effective collecting area of the telescope. T_{mast} stands for the transmission of the complete system, by far the most uncertain factor in this equation. While no precise measurements are available, but we estimate it to be $T_{mast} = 0.05$. The photon flux can thus be estimated to be

$$S \approx 3.0 \times 10^6 photons sec^{-1} pixel^{-1}.$$

Exposure time for a single frame: For a 1024×1376 pixel CCD camera with 56 % quantum efficiency, we should be able to detect 1.7×10^6 electrons per pixel. To fill 80 % (in order to avoid any kind of saturation) of the full well capacity (1.8×10^4 electrons) exposure time should be about 10 ms.

Signal-to-noise ratio (S/N): S/N for a single exposure is given by

$$(s/n) = \sqrt{S.t_{exp}} = 172$$

where t_{exp} is the exposure time in seconds. For n number of exposures, S/N for Stokes I measurement is given by

$$(S/N)_I = (s/n).\epsilon_I.\sqrt{N_a.n}$$

S/N for Q, U, and V are equal because all are being measured with same efficiency (discussed in chapter 2), which is given by,

$$(S/N)_Q = (s/n).\epsilon_Q.\sqrt{N_a.n}.$$

where N_a is number of intensity measurement in the modulation scheme; ϵ_Q, and ϵ_I are the modulation efficiency of the I and Q (Iniesta and Pillet 2012).

Noise is the inverse of S/N, so to detect polarization signal upto 10^{-3} noise, we need to have S/N around 1000 for Q, U, V. This can be achieved either by adjusting the number of frame or exposure time or both as per our science requirement.

4.2 Polarimetric accuracy

Polarimetric accuracy describes to what extent the real polarization signals (on the Sun) are actually reproduced by the polarimetric system. Solar polarimetry normally aims at measuring the full set of Stokes parameters (I, Q, U, V). The

accuracy is described by the difference between the ideal and the actual measurements matrix (X), which contains the relative errors to the measurement scale at its diagonal elements, the offsets to the zero point at the I⇒ Q,U,V components and general cross-talk at the other non-diagonal components.

For the ground based solar telescopes, polarimetric accuracy is governed by the following three factors (Del Toro Iniesta 2003):

- Seeing induced polarization due to Earth's atmosphere (denoted by matrix M_A): Intensity variations due to the seeing at the observation site can lead to spurious polarization signals because of the subtraction of intensities obtained at different times.

- Cross-talk introduced by the polarimeter itself (denoted by X): The effects concerning the performance of the polarimeter are taken into account by so called X-matrix or polarimeter response function.

- Instrumental polarization caused by the optical components of telescope (denoted by matrix T): It is important to note that MAST is a nine mirror system with two off-axis parabolic mirrors and 7 plane oblique mirrors. The oblique reflections of these mirrors complicate the measurement as the instrumental polarization corrupts the incoming radiation. Hence a systematic study of the instrumental polarization is needed in order to bring out the corrected Stokes profiles from the observation.

For strong magnetic field observations, as seeing induced polarization is negligible, it can be written as ⇒ $M_A \approx$I (identity matrix) (Del Toro Iniesta 2003). However, for weak magnetic field measurements and high resolution observations, this may not be true. Thus, the final polarimeter output is always given by

$$S_{out} = X.T.S_{sun}.$$

where one has to retrieve the Stokes vector of the incident light from the measurements (S_{out}).

The determination of these matrices is important for polarimetric accuracy. The polarimeter response matrix has been calculated for both the wavelength of interest, which is discussed in detail in the following section.

4.2.1 Experimental determination of response matrix (X) of the polarimeter

The relation between the incoming Stokes vector and measured Stokes vector can be written as,

$$S_{meas} = \mathbf{X}.S_{in}, \tag{4.2}$$

where $\mathbf{X}$ is the 4×4 element response matrix. The response matrix of the polarimeter can be determined experimentally from the measured Stokes parameters of the known input polarizations generated by calibration unit consisting of a zero order quarter wave plate (QWP) and a linear polarizer. We have computed the response matrix of the polarimeter in the laboratory using experimental setup shown in Figure 4.1 for both the wavelengths (6173 Å and 8542 Å).

In order to compute the response matrix of the polarimeter, the calibration unit (CU) is placed in the beam before the polarimeter module as shown in the Figure 4.1. The orientation of the axes has been determined with an accuracy of 0.5° for the linear polarizer and the QWP of CU which has been fixed in a computer controlled rotating mount. To determine $\mathbf{X}$ of the polarimeter, 80 known polarization states are created by rotating QWP from $0° - 160°$ with a step size of 2° and output intensity is measured by the polarimeter using four and six intensity measurement modulation schemes (as discussed in chapter 2). We have computed the response matrix of the polarimeter using both the schemes.

For the configuration shown in Figure 4.1, the input Stokes vector can be

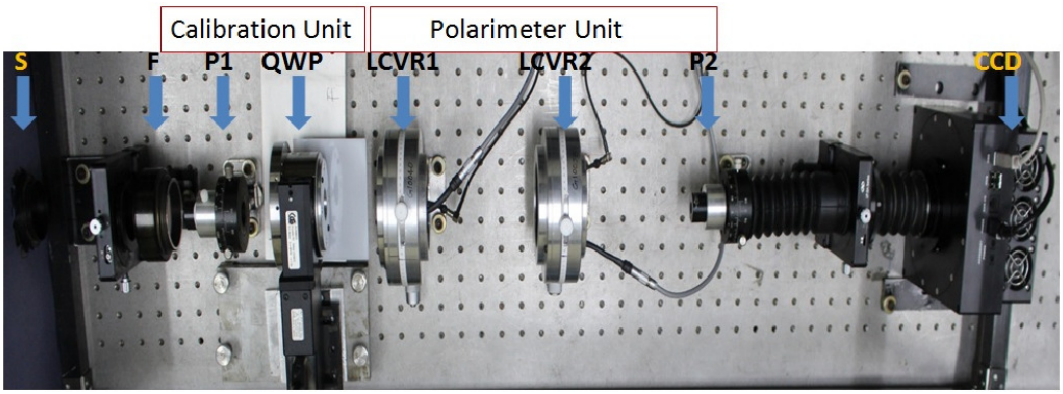

Figure 4.1: Experimental setup for the calibration of response matrix for MAST polarimeter. In this setup, a light beam is collimated using lens L1 and then collimating light passes through an interference filter (F), calibration unit consists of a linear polarizer (P1) and a zero order quarter wave plate (QWP), and polarimeter consists of two LCVRs (LCVR1 and LCVR2) and a linear polarizer (P2). Finally, image is formed by imaging lens on CCD which is placed in the focal plane of the imaging lens.

written as,

$$S_{in} = M_{QWP}(\theta_r, \delta).M_{P1}(\theta_p).[1000]^T,$$

where θ_r and θ_p are the orientation of the retarder and polarizer of the CU relative to the reference axis and δ is the retardance of QWP. In our case, we fixed θ_p at 0°, then the input Stokes parameters for different retarder orientation are given by,

$$\left.\begin{aligned} I &= 1, \\ Q &= cos^2(2\theta) + sin^2(2\theta).cos(\delta), \\ U &= sin(2\theta).cos(2\theta).(1 - cos(\delta)), \\ V &= -sin(2\theta).sin(\delta). \end{aligned}\right\} \tag{4.3}$$

For n orientations of CU retarder, polarimeter response matrix is calibrated from the measurements after rearranging the Stokes vector into n×4 matrices by a solution of the linear problem,

$$S_{meas} = X.S_{in},$$

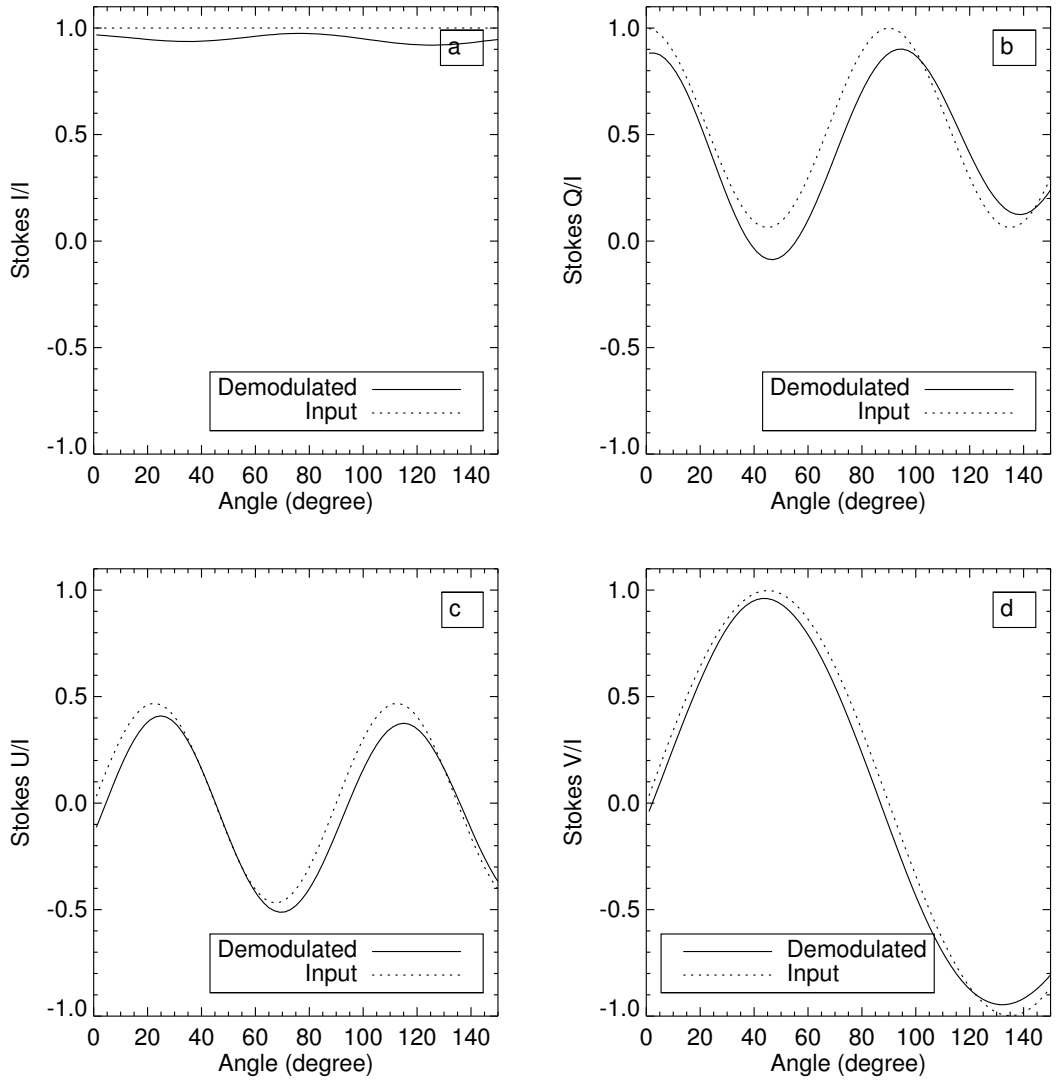

Figure 4.2: Plots of input Stokes parameters and demodulated Stokes parameters calculated at each position angles of QWP of CU for 6173 Å wavelength.

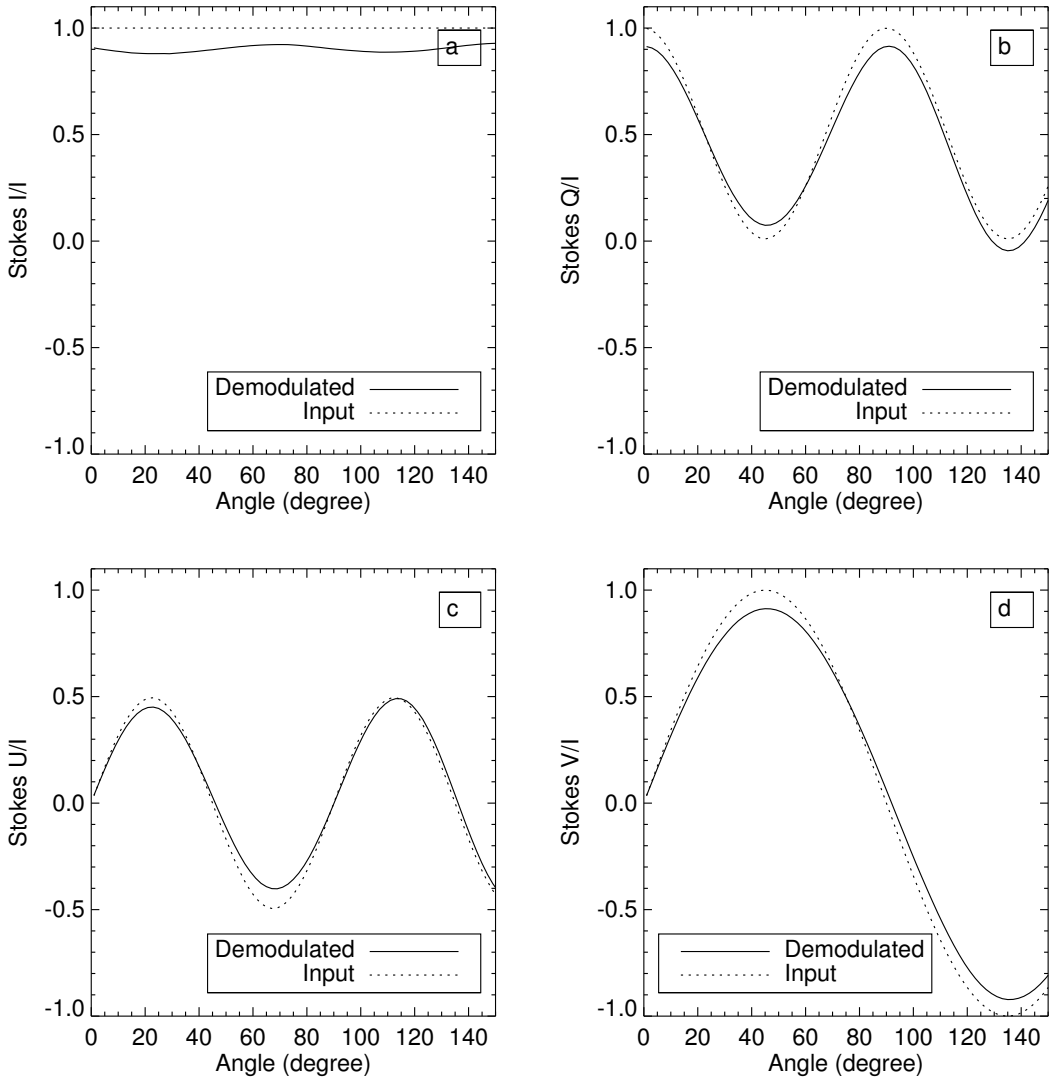

Figure 4.3: Plots of input Stokes parameters and demodulated Stokes parameters calculated at each position angles of QWP of CU for 8542 Å wavelength.

Multiplying by S_{in}^T from the right in above Equation

$$S_{meas}.S_{in}^T = X.S_{in}.S_{in}^T = X.D,$$

where

$$D = S_{in}.S_{in}^T.$$

Therefore, the final expression for response matrix is

$$X = S_{meas}.S_{in}^T.D^{-1}. \tag{4.4}$$

4.2.2 Response matrix for four measurement modulation scheme

We have computed X when Stokes parameters were obtained by four measurement modulation scheme and the other procedures were same as discussed in Section 4.2.1. The response matrix of the polarimeter for 6173 Å is, Hence, response matrix for 6173 Å is determined from the above equation using input and measured Stokes vector can be written as,

$$X_4^{6173} = \begin{pmatrix} 1.0000 & -0.0507 & -0.0054 & -0.0595 \\ -0.0090 & 0.8946 & -0.1618 & -0.0369 \\ -0.0447 & -0.0639 & 0.8314 & 0.0734 \\ -0.0474 & -0.1494 & 0.0647 & 0.9665 \end{pmatrix} \tag{4.5}$$

The uncertainty in the measurement of X arises due to uncertainties in the knowledge of calibration optics parameters. The error in the calibration is obtained by evaluating the total deviation of the fit and is given as

$$\sigma^2 = \frac{1}{N} \sum (S_{meas} - X.S_{in})^2$$

The variance is obtained of the order of 1×10^{-3} in this case. Therefore uncertainty of each of the elements of the response matrix is of the order of 10^{-3}.

Thus, the real incoming Stokes vector S_{in} can be calculated from the observed Stokes vector and measured response matrix as follows,

$$S_{in} = X^{-1}.S_{meas}.$$

The input and the demodulated Stokes parameters at each CU retarder orientation are shown in Figure 4.2.

Similarly, we have determined the response matrix of the polarimeter at 8542 Å wavelength and given by,

$$X_4^{8542} = \begin{pmatrix} 1.0000 & 0.0006 & 0.0349 & -0.0965 \\ -0.0009 & 0.8931 & -0.1053 & 0.0041 \\ -0.0135 & -0.0616 & 0.9073 & -0.1809 \\ 0.0873 & 0.0452 & 0.1948 & 0.9115 \end{pmatrix}, \tag{4.6}$$

where the variance is of the order of 1×10^{-3} correspondingly and plots for the input and demodulated input Stokes parameters are shown in Figure 4.3.

4.2.3 Response matrix for six measurement modulation scheme

Similarly, we have also computed X when Stokes parameters were obtained by six measurement modulation scheme and the other procedures were same as discussed in Section 4.2.1. The response matrix of the polarimeter for 6173 Å is,

$$X_6^{6173} = \begin{pmatrix} 1.0000 & -0.0084 & 0.0153 & -0.0016 \\ 0.0009 & 0.9493 & 0.0265 & 0.1462 \\ -0.0171 & 0.0254 & 0.9573 & 0.0901 \\ 0.0043 & -0.1829 & -0.0808 & 0.9491 \end{pmatrix}. \tag{4.7}$$

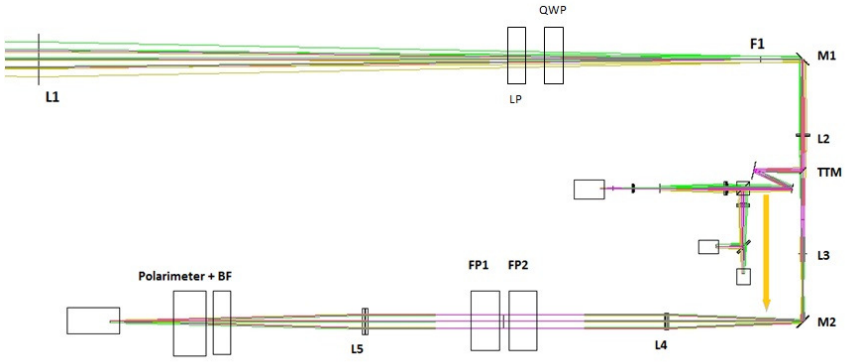

Figure 4.4: Schematic diagram of the narrow-band imaging spectro-polarimeter along with calibration optics. FP1 and FP2 along with blocking filter (BF) forms narrow-band filter. Polarimeter is placed just before the CCD camera for polarization measurements. Lenses and mirrors shown are for re-imaging and for beam steering, respectively. Section 4.2.1 explains the calibration of polarimeter alone using a laboratory source; however, for better polarimetric accuracy, all other optical components along the light path need to be included in the calibration. Hence, a calibration unit consists of linear polariser and a quarter wave plate is placed before the F1 in the F#42.6 beam.

where variance is of the order of 1×10^{-3}.

Similarly, the response matrix of the polarimeter for 8542 Å is,

$$X_6^{8542} = \begin{pmatrix} 1.0000 & 0.0062 & -0.0177 & 0.0044 \\ -0.0056 & 0.9251 & 0.0665 & 0.1308 \\ -0.0652 & 0.0396 & 0.9454 & 0.0791 \\ 0.0344 & -0.1379 & -0.1509 & 0.9176 \end{pmatrix}. \tag{4.8}$$

correspondingly variance is of the order of 1×10^{-3}.

4.2.4 Determination of X with MAST for 6173 Å

In the earlier sections, we have discussed calibration of polarimeter alone using an experimental setup consists of a laboratory source. However, polarimeter is used along with narrow-band filter and other optical components for solar observations. Figure 4.4 shows the schematic of the imaging spectropolarimeter

along with calibration optics. As the polarimeter is placed just before the CCD camera which is used for acquisition of polarization measurements, it is necessary to include all the optical components in the light path in estimating the response matrix. Hence, we place a calibration unit consists of a linear polarizer and a quarter wave plate after L1 in F-42.6 beam. We next calibrated the polarimeter directly using sunlight from the telescope using six measurement modulation schemes. The output from the MAST has to pass through a set of different optical components (as shown in Figure 4.4) compared to the lab setup shown in Figure 4.1. Therefore, we need to determine the response matrix of the polarimeter once again in the same way as discussed earlier to consider the effect of all these optical components on the polarization measurements.

Following previous method, the response matrix determined with the MAST is using six measurement modulation scheme,

$$X_{MAST} = \begin{pmatrix} 1.00000 & 0.06930 & 0.00601 & 0.06087 \\ -3.2410.10^{-7} & 0.82774 & -0.07714 & -0.15418 \\ 1.4901.10^{-8} & 0.10421 & 0.74701 & 0.11685 \\ 7.4506.10^{-9} & 0.138909 & -0.11104 & 0.70949 \end{pmatrix}. \tag{4.9}$$

Note that the matrix elements of X_{MAST} are different than the elements of X_6^{6173} because of the different intervening components in the MAST setup (see Figure 4.4). The input, measured, and demodulated Stokes parameters I, Q, U, and V at each QWP orientation are shown in Figure 4.5. From these figures cross-talk introduced in Stokes Q, U, and V can be easily seen. We need to remove the cross-talk from the telescope itself. Along with the telescope matrix, X_{MAST} will be used to get the real Stokes vector from the measured Stokes vector.

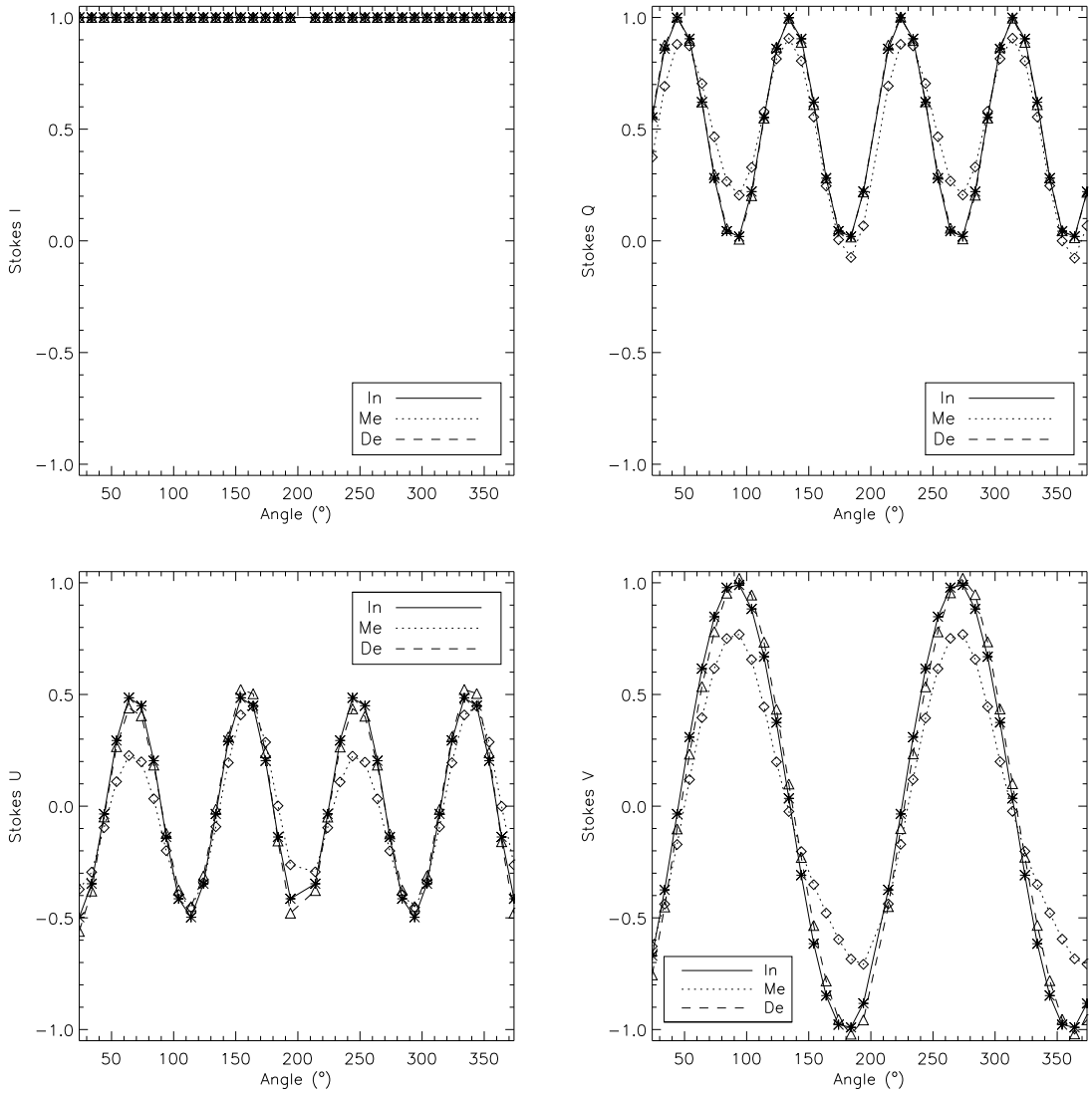

Figure 4.5: Plots of input (In), measured (Me), and demodulated (De) Stokes parameters calculated at each position angles of QWP of CU for 6173 Å wavelength

4.3 Summary

In this chapter, we have discussed about the sensitivity of the polarimeter. In this regard, we have estimated exposure time and number of polarization measurements needed for the required polarimetric sensitivity to achieve the scientific goals of MAST. We also have discussed the several factors which are responsible for the polarimetric accuracy. We have used two separate polarimeters for polarization measurement in the photosphere and chromosphere at two different wavelength 6173 Å and 8542 Å. For both the polarimeters, the response matrices have been experimentally determined in the lab using an experimental setup for both the modulation schemes (four and six measurement). We have also calibrated the polarimeter at the back-end of MAST using direct sunlight coming from quiet Sun to see the polarization effect from the other intervening components in the path to the polarimeter.

Chapter 5

Spectropolarimetric Observations from MAST

5.1 Introduction

Imaging spectropolarimeter consists of narrow-band imager and polarimeter is integrated with MAST after the calibration of each instrument and started providing spectropolarimetric observations. For the present set of observations, we have modulated the polarization first and changed the wavelength later to minimize the seeing influence. As we know that the response time of a Nematic LCVR depends on the direction of voltage change. In increasing of voltage it is faster than decreasing of voltage. The response time of LCVRs (for the change of one polarization state to other) is taken as 22 ms which is the maximum value.

Change in wavelength position requires 100 ms and 200 ms for a spectral sampling of 15 mÅ, and 30 mÅ, respectively as the tuning speed of the FPs is nearly 1000 Vs^{-1} whereas the temperatures of FP1 and FP2 is fixed at 35°C and 28°C, respectively. We need to capture several images for each polarization state to build-up the signal for moderate seeing condition. The number of images can be increased or decreased as per the seeing condition. The exposure time is also

depend on the seeing conditions. As S/N depends on both these factors, we need to adjust between these to increase the temporal cadence of the spectropolarimetric observations. Overall time taken for one modulation cycle (i.e. for obtaining IQUV at one wavelength positions with 20 images) is around 8 seconds considering an exposure time of 60 ms (at 6173 Å). The time cadence of the vector magnetogram varies depending on the number of wavelength positions. For example, the cadence varies from 40 seconds to 216 seconds for 5 to 27 wavelength positions. The number of wavelength points which determine the time cadence can be selected as required by the scientific objectives.

For the initial tests, we have scanned the spectral profile of 6173 Å line with a step of 15 mÅ and 30 mÅ, for a total of 27 and 20 positions, respectively in longitudinal mode. The number of wavelength positions could be considerably reduced by an optimization after inverting the profiles, which will be carried out after further analysis. In the following sections, some of the preliminary observations obtained with the imaging spectropolarimeter are discussed. For these observations polarimeter is operated in longitudinal and vector mode. Further, we also compare our data with the data provided by HMI onboard SDO.

5.2 Spectropolarimetric Observations in Longitudinal Mode

The observations described in this section are obtained for a sunspot in the active region NOAA AR 12436 taken on October 24, 2015 between 4:00 UT and 5:30 UT, when the seeing was moderate. The active region was slightly away from the disk center and located at N09 and W20. FP etalons of the narrow-band imager were sequentially tuned to 27 positions on the 6173Å line, with 15 mÅ wavelength spacing. A pair of two images in left- and right- circular polarizations (LCP & RCP) was obtained by applying appropriate voltages (listed in Table 2.3) to the

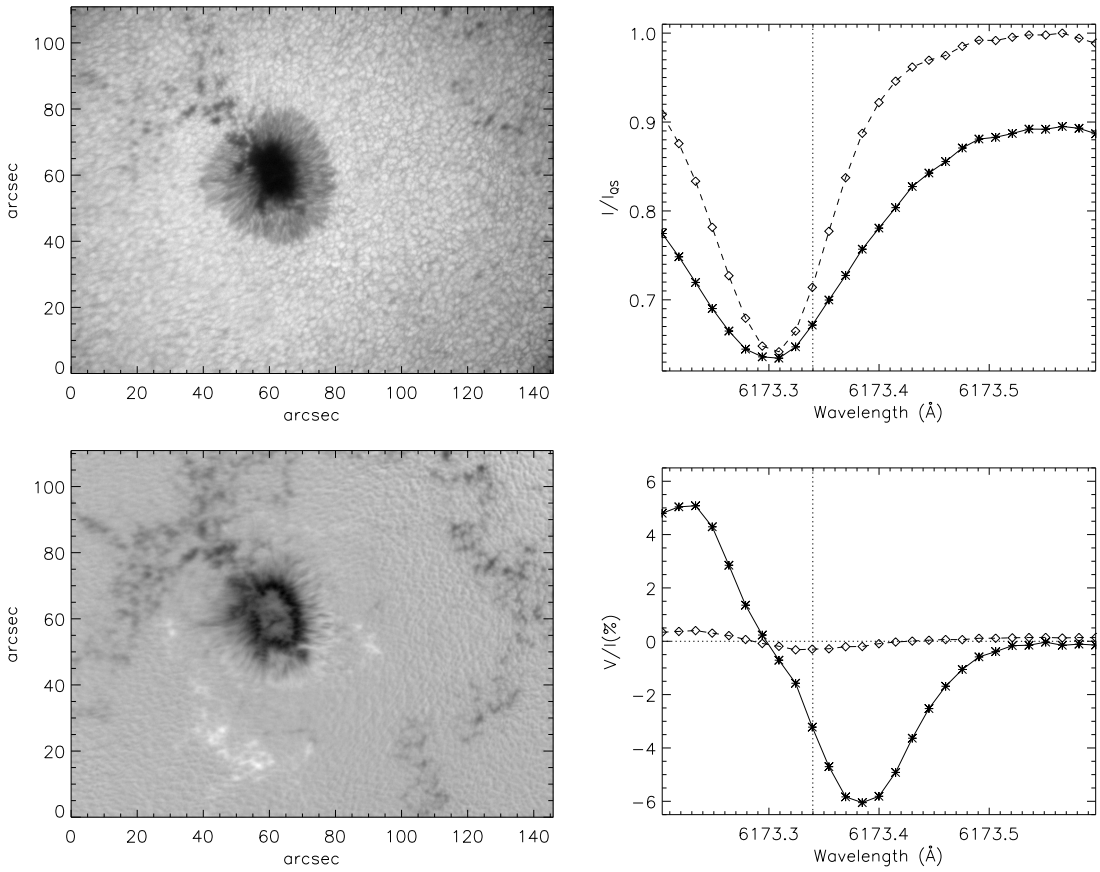

Figure 5.1: LOS mode of observations of the active region NOAA AR 12436 observed on October 24, 2015 between 4:00 UT and 5:30 UT using MAST polarimeter. In the first row, the left figure shows one of the mean intensity images whereas the right figure is for the corresponding mean Stokes I profiles. The Stokes I profile is deduced separately for the magnetic (solid line) and for the non-magnetic (dashed lines) regions whereas in the second row, left figure displays the mean Stokes V image for a wavelength position at +75 mÅ from line center and right plot indicates the mean Stokes V profiles for both the magnetic and non-magnetic regions. Because of the limitation of the voltage tuning of both the etalons in tandem, line profile shifted more toward blue side.This observation is helpful in optimizing the temperature of FP etalons in retrieving the line-profile completely (refer section 5.2.2).

LCVR 1 and 2. For these measurements, the voltage of the LCVR1 is changed alternately, whereas the LCVR2 is kept constant to provide a retardance of 1λ. For each wavelength position, 20 pairs of LCP and RCP images were obtained with an exposure time of 65 ms to increase the signal to noise ratio (SNR). Figure 5.1 shows the results of the above observation. The top left figure shows one of the mean intensity image whereas the right figure is for the corresponding mean Stokes I profiles. The mean Stokes I profile is deduced separately for both the magnetic (solid line, where the V signal is more than 10^{-3}) and for the non-magnetic (dashed line) regions. The broadening of the profile due to the magnetic field is evident in these plots. The bottom left figure displays the mean Stokes V image for a wavelength position at +75 mÅ from line center whereas the right plot indicates the mean Stokes V profile for both the magnetic and non-magnetic regions.

5.2.1 Comparison of Stokes V observations in 6173 Å from SDO/HMI and USO/MAST

We also carried out a comparison of our results with the magnetograms availed from *Helioseismic Magnetic Imager* (HMI) instrument (Scherrer et al. 2012; Schou et al. 2012) onboard the *Solar Dynamics Observatory* (SDO) (Pesnell et al. 2012). For comparison, the images from MAST and HMI were taken at around the same time (04:42 UT on October 24, 2015). The comparison was possible as the spectral line used by both the instruments is same, even though the spectral resolution of each instrument differs. HMI provides both LOS and vector magnetograms. It also provides LCP, RCP with 45 second cadence and Stokes I, Q, U, V images with 12 minute cadence. For the comparison, we have restricted our analysis to HMI LOS magnetograms and Stokes V images, since our linear polarization measurements (Q, U) need further instrumental polarization correction. The stokes V profiles could also get contaminated by the instrumental polariza-

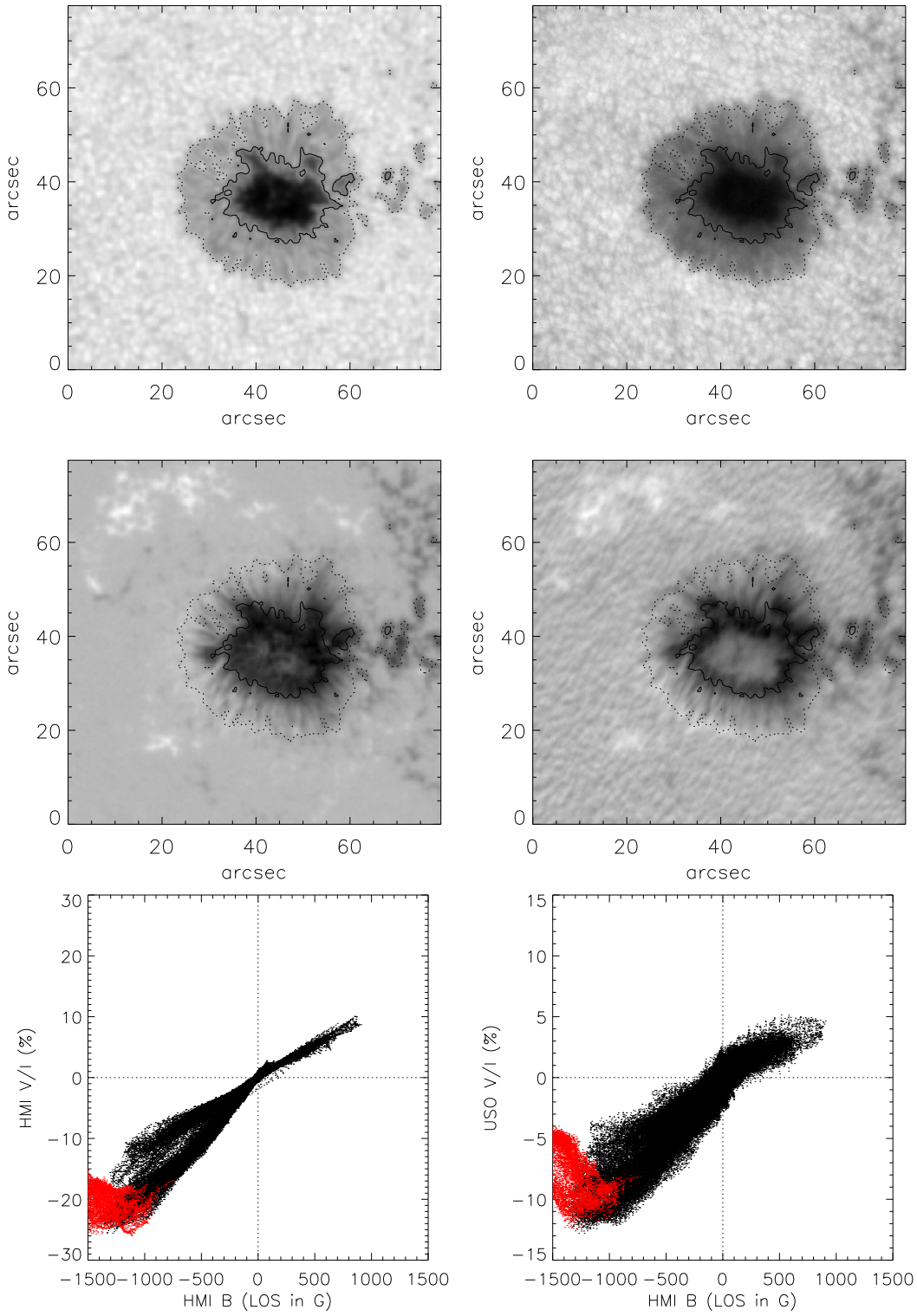

Figure 5.2: Top row: Stokes I image taken by SDO/HMI (left) and USO/MAST (right); Middle row: Stokes V image at wavelength position +75 mÅ from line center taken by SDO/HMI (left) and USO/MAST (right); bottom row: scatter plot made between Stokes V of SDO/HMI and longitudinal magnetic field of SDO/HMI (left) and scatter plot made between Stokes V of USO/MAST and longitudinal magnetic field of SDO/HMI (right).

tion, but the cross-talk from the linear polarization mostly introduce only a bias in Stokes V images. Thus, the present comparison should not get affected.
The image obtained from the HMI is resized, and the MAST image is registered with respect to HMI image. The right and left images in the top panel of Figure 5.2 show the cropped continuum images taken with HMI and MAST instruments, respectively. The images are cropped in such a way that they include the sunspot and a part of the nearby area. The middle panel shows the Stokes V images of HMI (left) and MAST polarimeter (right), respectively for a selected wavelength position +75 mÅ away from the line center. It is evident from the figures that most of the magnetic features in the Stokes V map of HMI matches well with the Stokes V map of MAST polarimeter. The advantage of the space-based observation is clearly visible in the HMI images from the low background features.

Unlike HMI observations, the MAST images are affected by the atmospheric seeing during the image acquisition which results in a considerable I→V cross-talk (Del Toro Iniesta 2003; Lites 1987) thus a higher background noise. This I→V cross-talk is evident from the granulation pattern in Stokes V images of MAST.

The bottom panels of Figure 5.2 are for the Stokes V signal obtained at a wavelength position +75 mÅ (away from the line center) plotted against the HMI LOS magnetic field strength. The plot shown in the left panel is for the HMI Stokes V whereas the right is for the MAST Stokes V at a close by wavelength position against the HMI LOS magnetic field strength. The region shown with the red contain points mostly from the umbra, where the linearity between the Stokes V amplitude and the magnetic field strength doesn't hold. It is evident from Figure 5.2 that other than the scatter which could be partly due to the seeing related I→V cross-talk, the trend matches closely.

We also found a difference of factor of around 2 in the Stokes V signal between the HMI and the MAST images. This can be explained by the influence of finite width of the narrow band filter in scanning the line profile and the difference in the overall instrumental profiles used in the HMI and MAST imager. The

finite width of the filter results in a convolution of the spectral line profile, which introduces an apparent increase in the width and decrease in the depth of the line profile. This effectively reduces the amplitude of the Stokes V signal. In order to check this, we have computed synthetic line profiles using Milne-Eddington inversion code, taking realistic solar atmospheric parameters. Convolution of the Stokes V parameter with the filter profile of 95 mÅ FWHM shows a reduction in the peak of Stokes V amplitude by a factor 2 (*approx.*). This effect can be taken care while inverting the Stokes profiles; *i.e.*, convolution of the synthetic profile with filter profile before fitting that with observed Stokes profiles. Other than the above differences, the overall comparison between HMI and the MAST Stokes V measurements enhances the confidence in our measurements.

5.2.2 Observations of NOAA AR 12529 on April 16, 2016

As evident in the Stokes I profile in the top panel of Figure 5.1, the starting point for the wavelength scanning has a limited coverage in the blue wing side of the 6173 Å line profile. This was due to the limited tuning range of the Fabry-Perot filters, which was restricted due to the maximum voltage which could be applied to the etalons for the operating temperatures of the etalons. As it is important to cover the entire wavelength range in order to obtain the continuum intensity at both sides of the line profile, we have carried out a re-tuning of the etalons to optimally cover the continuum at both the sides. Since the maximum allowed voltage which could be applied to the etalon is restricted, the re-tuning was done by changing the operating temperature. The re-tuning allowed us to start the line profile scan from a shorter wavelength point in the continuum. The following example of the Stokes V scan was carried after the re-tuning of the filters. These observations were taken on April 16, 2016. Here the sunspot in the active region NOAA AR 12529 (N10, W38) was observed with the polarimeter. The observations were obtained between 07:00 UT and 07:30 UT. During data

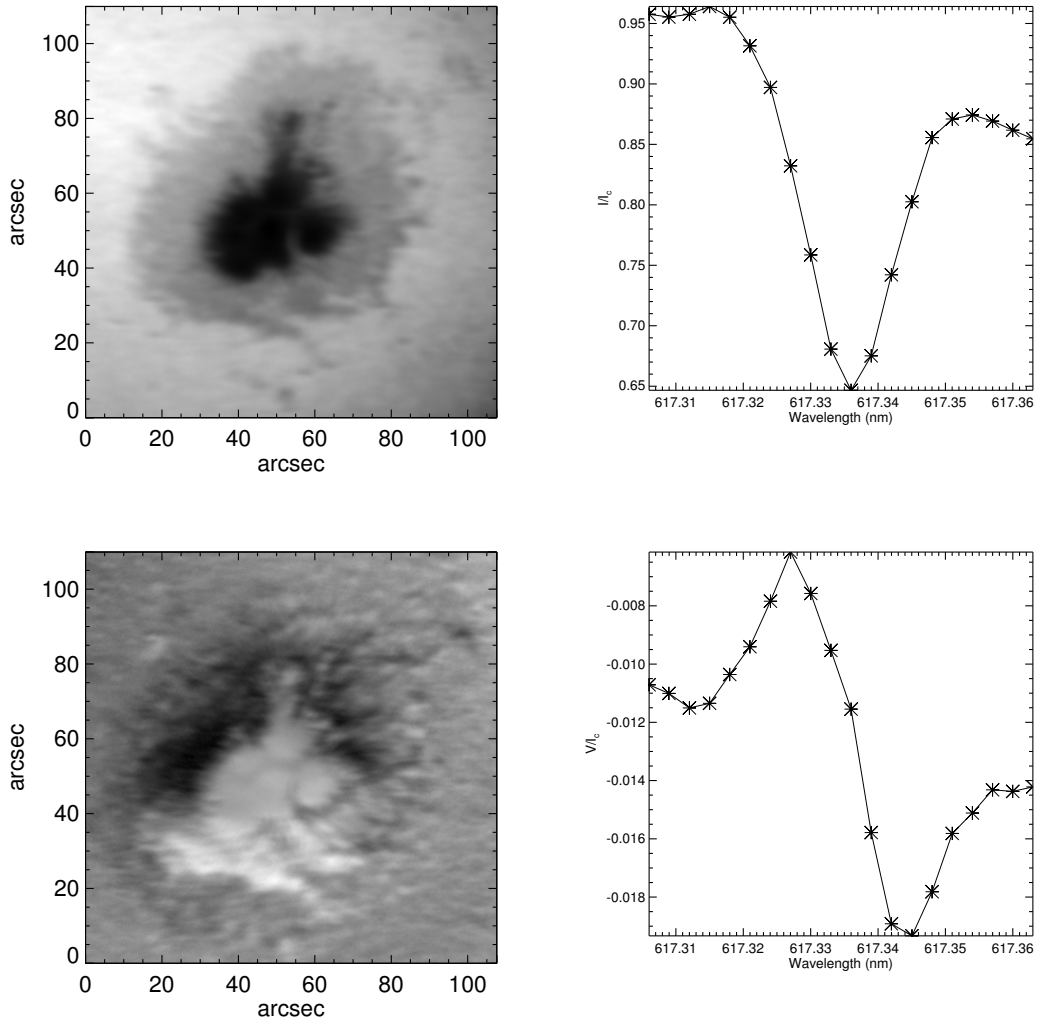

Figure 5.3: Stokes I and V observations of the active region NOAA AR 12529 in the spectral line 6173 Å. Top Row: Mean intensity (Stokes I) image (left) and its mean intensity profile (right). Bottom Row: Mean Stokes V image (left) and its mean profile (right).

acquisition, the seeing was again moderate. Unlike the previous observations, we increased the wavelength spacing to 30 mÅ instead of 27 wavelength positions which resulted in around 20 spectral positions on 6173 Å line for the wavelength scan. Figure 5.3 shows the images for the wavelength position +75 mÅ from the line center and the corresponding mean Stokes V profile (right) for the entire FOV. In this case, the wavelength scan started well in the blue continuum, and the Stokes V signal also covers enough continuum wavelength points.

5.2.3 Inversion of Spectropolarimetric Data with SPIN code

Once a set of Stokes profiles is available, an inversion techniques is needed to infer the magnetic and the thermodynamic properties of the solar atmosphere from the observed Stokes profiles of a particular spectral line. The basic idea of an inversion technique is to fit the synthetic Stokes profiles to the observed ones to retrieve the information about the solar atmosphere.

The inversion codes are based on the solution of the polarized radiative transfer equations (RTE) in the presence of magnetic field after taking in account the Zeeman effect and quantum mechanical corrections. In this technique, the analytical solution of RTE is used to synthesize the Stokes profiles. After synthesis, they are compared with the observed ones using Levenberg-Marquardt (LM) algorithm fitting techniques. In LM algorithm, fitting is initiated by a set of guess parameters. During each subsequent iterative process the free parameters are modified to minimize the difference between the observed and the synthetic Stokes profiles. The final fitted parameters are treated as the model of the solar atmosphere.

A new **Stokes Profile INversion (SPIN)** code has been developed specifically to invert the spectropolarimetric data of the MAST at USO. SPIN code (Yadav et al. 2017) has adopted Milne-Eddington approximations to solve the po-

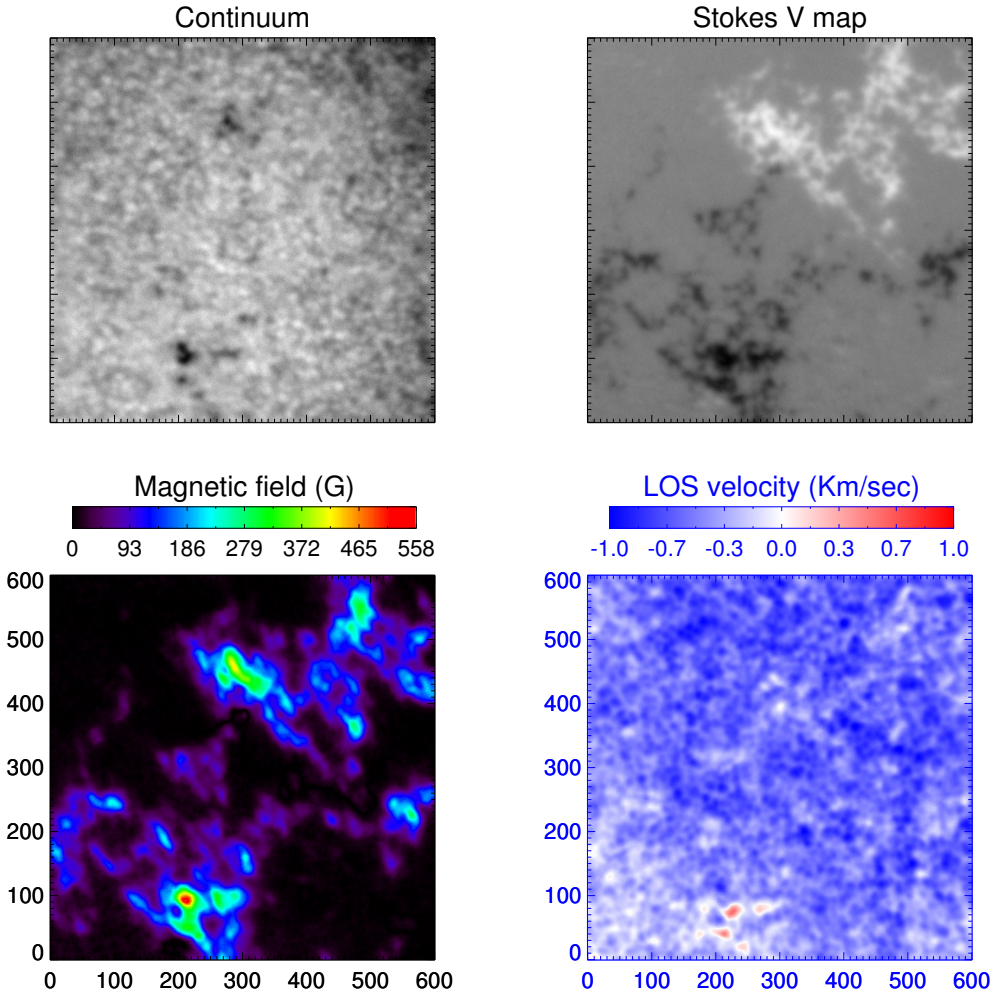

Figure 5.4: Inverted maps of NOAA AR 12648 retrieved from SPIN: The top left figure shows one of the continuum intensity map whereas the right figure is for the Stokes V map at a wavelength position ≈ -125 mÅ from the line center. The bottom left Figure displays the map for the LOS magnetic field whereas the right Figure displays the LOS velocity map.

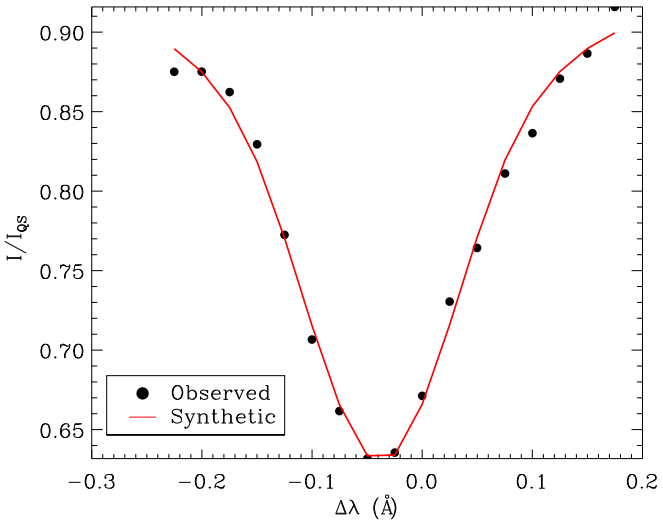

Figure 5.5: The observed and synthetic Stokes I profiles obtained using SPIN for a pixel location (200,100) in a pore shown in Figure 5.4.

larized radiative transfer equation (RTE) and a modified Levenberg-Marquardt algorithm has been employed for the fitting.

The observations described in this section were recorded under moderate seeing for a small pore and an internetwork region in the active region NOAA AR 12648 on April 7, 2017 between 4:35 UT and 4:45 UT. The active region was located at S03 and W05 near disk center. FP etalons of the narrow-band imager were sequentially tuned to 17 positions on the 6173 Å line, with 25 mÅ wavelength spacing. At each wavelength position, 50 pairs of LCP and RCP images were obtained with an exposure time of 60 ms to increase the signal to noise ratio (S/N). Before analyzing the observed Stokes profiles, all Stokes images are dark subtracted and flat fielded using the standard approach. After the dark and flat field correction the Stokes I and V profiles have been inverted using SPIN code. Inverted results are shown in Figures 5.4, 5.5, and 5.6. The top left panel of Figure 5.4 shows one of the continuum intensity map whereas the right panel is for the Stokes V map at a wavelength position ≈ -125 mÅ from the line center. The bottom left panel displays the map for the LOS magnetic field whereas the right

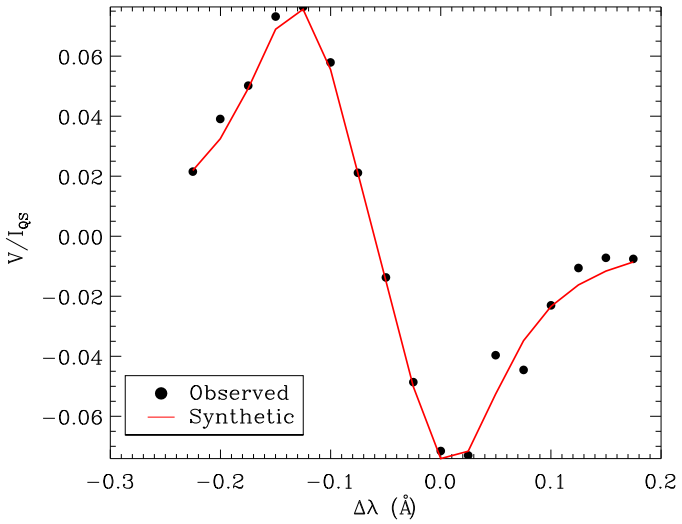

Figure 5.6: The observed and synthetic Stokes V profiles obtained using SPIN for a pixel location (200,100) in a pore shown in Figure 5.4.

Figure displays the LOS velocity map. Figures 5.5 and 5.6 show the observed and synthetic Stokes I and V profiles obtained using SPIN for a pixel location (200,100) in a pore.

5.2.4 Stokes V Observations in 8542 Å

In this section, we report the circular polarization measurements obtained in the spectral line 8542 Å line. The measurements were carried out with the second pair of LCVRs specifically procured for this wavelength. The imager is tuned to the blue wing −150 mÅ from the line center. The LCVR is sequentially switched between voltages corresponding to the modulation voltages for the left and right circular polarizations. A pair of 100 images were obtained for this measurement with an exposure time of 120 ms for each image. In Figure 5.7, left panel shows one of the selected I+V images from these observations, whereas the right panel shows the mean V image at the above wavelength point. A clear Stokes V signal is present in the difference image (Figure 5.7, right). The seeing variations and the long exposure times produce artifacts, which will be expected to be reduced

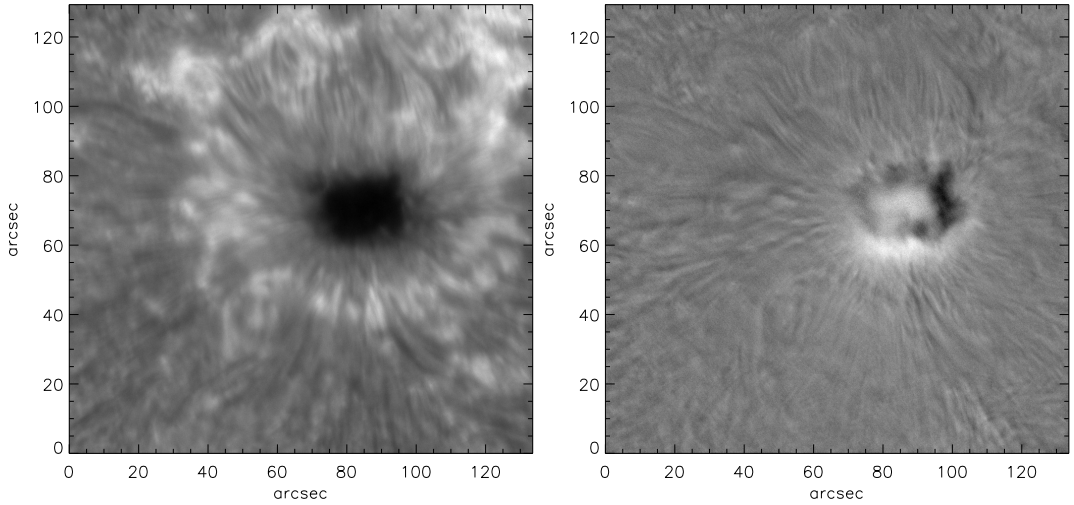

Figure 5.7: LOS observations in the spectral line 8542 Å of the active region NOAA AR 12546 (S07, E19) observed on May 18, 2016 between 08:30 UT and 08:36 UT using MAST polarimeter. Images of I+V (left) and mean Stokes parameter V (right) at a wavelength position −150 mÅ from the line center.

by the ongoing adaptive optics installation. In the above observations, the images were taken only at one wavelength position, but the filter can be tuned over a considerable part of the 8542 Å line profile, which will be done in the future observations. The linear polarization measurement is also planned for this line.

5.3 Preliminary spectropolarimetric observations in vector mode for 6173 Å

By operating the polarimeter in vector mode, we have carried out observations on December 19, 2015. The active region NOAA AR12470 (N15, W07) was observed during the period 06:00 UT and 07:30 UT. Four images were obtained sequentially by applying appropriate voltages (listed in Table 4) to the LCVRs. From the observed intensity images, Stokes, I, Q, U and V images were computed for each wavelength position. Similar to the longitudinal mode the images in vector mode were acquired by scanning the line profile with 15 mÅ spacing and at 27

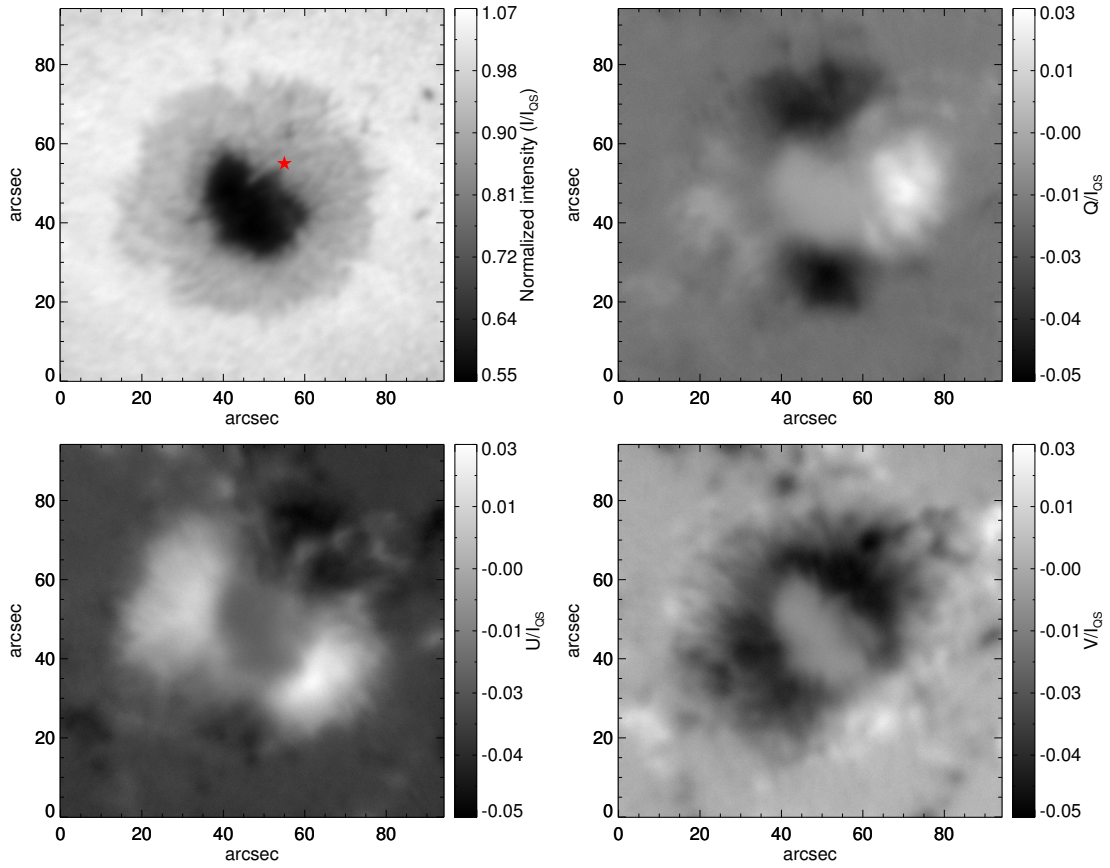

Figure 5.8: Stokes images obtained using vector mode of operation for NOAA AR 12470 at 6173 Å are shown here. Top panels show Stokes I (left), Q (right). Bottom panels show Stokes U (left) and V (right).

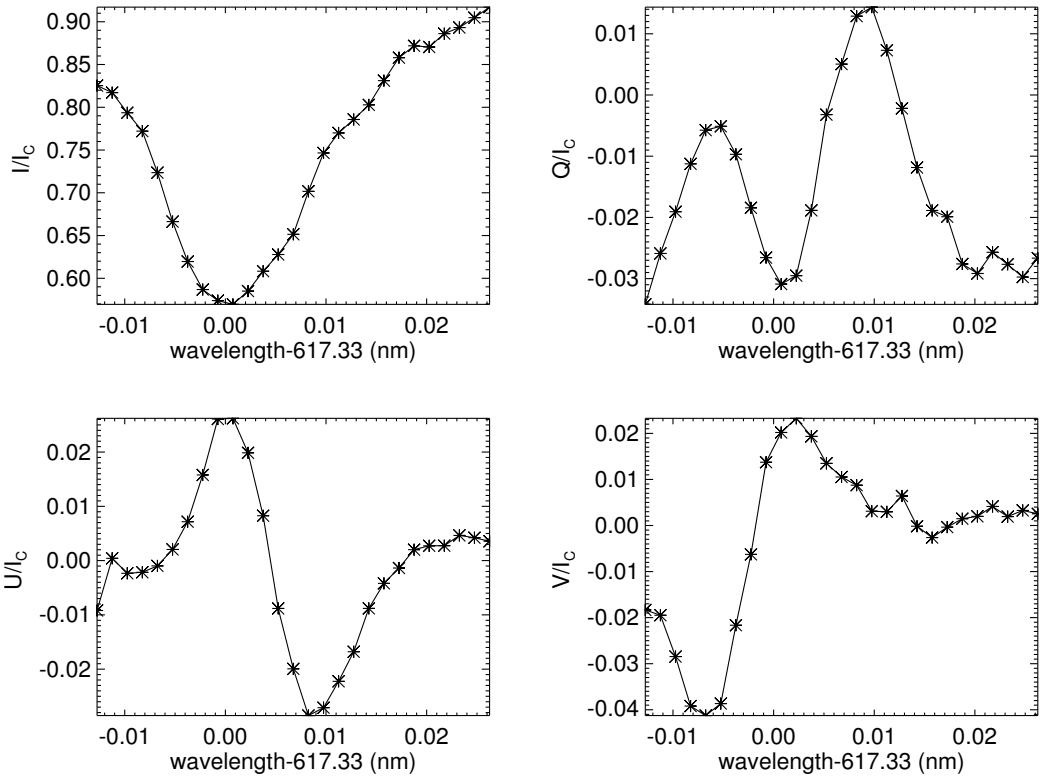

Figure 5.9: Profiles of Stokes parameters I, Q, U, and V at a point in the penumbra of NOAA AR 12470 corresponding to the star mark in Figure 5.8.

wavelength positions. Top left and right panels of Figure 5.8 show the Stokes I, and Q, the bottom left and right panels of Figure 5.8 show the U and V images, respectively. These images of Stokes parameters are shown for a wavelength position at +75 mÅ from line center on the line profile. Figure 5.9 shows respective Stokes profiles for the single point marked by a star in the Stokes I image (Figure 5.8). A thorough analysis and demodulation of the linear polarization measurement requires the knowledge of the instrumental polarization. For this purpose, we are currently introducing a large (50 cm) sheet linear polarizer which can be rotated, in front of the primary mirror (see Figure 6.1). This will enable us to characterize the telescope polarization before extracting the Stokes information from these measurements.

Figure 5.10 shows the images of Stokes parameters I, Q, U, and V before and after the application of response matrix X_{MAST}. This sunspot is a part of an active region NOAA 12645 which was observed on March 31, 2017. The observations were obtained between 04:35 UT and 05:30 UT when the seeing was moderate. The demodulated Stokes parameters are now free from the cross-talk arising due to polarimeter itself and the other components coming in between the calibration unit and polarimeter. However, the cross-talk from the telescope itself will be removed after the determination of telescope matrix as discussed in the next chapter.

5.4 Summary

After the calibration of polarimeter, it is integrated with narrow-band imager. Spectropolarimetric observations using MAST have been made for selected active regions in both photospheric and chromospheric heights. These observations have been used to obtain Stokes parameters both in LOS and vector modes. We have also compared the Stokes I and V observations from MAST with those of HMI as it also observes in same wavelength (6173 Å). Qualitatively, the two observations

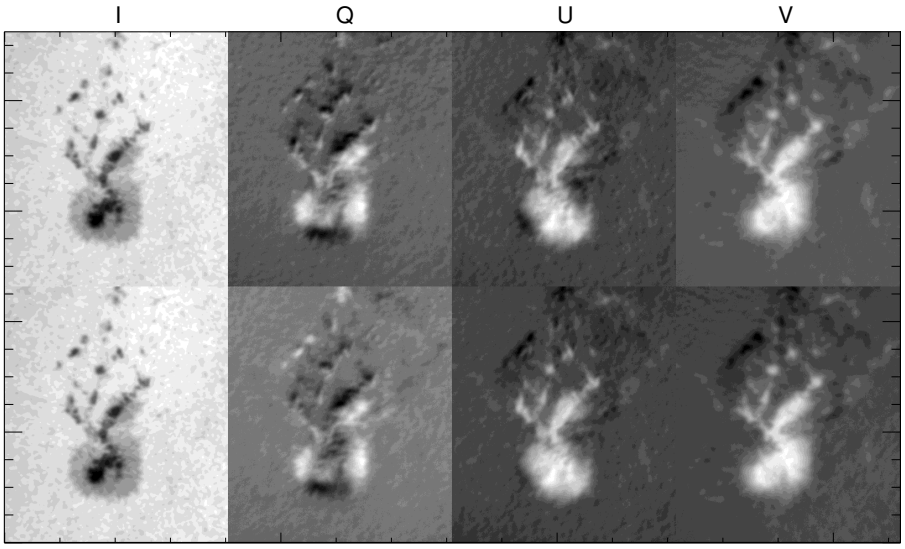

Figure 5.10: Top and bottom rows show the Stokes I, Q, U, and V before and after the application of response matrix X of MAST.

matches well, considering the fact that MAST observations are limited by seeing. The Stokes parameters I and V have been inverted using the SPIN inversion code to estimate the LOS magnetic and velocity fields. For the initial tests, LOS observations were acquired by scanning the line profile of Fe I 6173 Å at 27 wavelength positions with a sample of 15 mÅ. We have a plan to minimize the number of wavelength positions to 8-12 to improve the observation cadence. The vector magnetic field data can be used for scientific purposes after the removal of the instrumental polarization from the all the Stokes profiles.

Chapter 6

Summary and Future Plan

Solar magnetic fields are the fundamental cause of all forms of observed quiet and active phenomena at a large range of temporal and spatial scales. Therefore, measurement of solar magnetic field is very important. In this thesis, we have described the development of an imaging based spectro-polarimeter as a back-end instrument of MAST for measuring the solar magnetic fields in two wavelength 6173 Å and 8542 Å. Major part of the thesis deals with the description of the development of polarimeter. It includes discussion about the characterization of the polarimeter components and calibration of the polarimeter. In addition we have also presented the obtained Stokes parameters by observing solar active regions with our instrument and then compared spectropolarimetric observations from MAST/USO with the observations from HMI/SDO. In the following, we briefly summarize the thesis work, and then discuss the future work.

6.1 Summary

Multi-Application Solar Telescope (MAST), a 50 cm off-axis Gregorian telescope, was installed at Udaipur Solar Observatory (USO), India, which has been made operational recently. For understanding the evolution and dynamics of solar magnetic and velocity fields, an imaging spectropolarimeter has been developed

at USO as one of the back-end instruments of MAST. This system consists of a narrow-band imager and a polarimeter. This instrument is capable for the near simultaneous observations in the spectral lines at 6173 Å and 8542 Å, which are formed in the photosphere and chromosphere, respectively. The focus of this thesis is on the development of a polarimeter for measuring the polarization signal induced in the photosphere and chromosphere. The polarimeter includes a linear polarizer and two sets of Liquid Crystal Variable Retarders (LCVRs). It is known that the retardance of LCVR depends on the voltage and temperature. Voltage at a constant temperature is used for fast modulation.

However, fluctuations in the temperature and voltage reduces the accuracy in the polarimetric measurements. Thus we have characterized LCVRs of the polarimeter for various combinations of voltages and temperatures. Further, to achieve a sufficient polarimetric accuracy of 10^{-3} , it is necessary to measure the response matrix of the polarimeter at regular intervals. The response matrix gives the deviations from the ideal theoretical polarimeter. The measurement of the response matrix of the polarimeter is performed by introducing a calibration unit (CU) consisting of a linear polarizer and a zero order quarter wave plate (QWP). Both elements are placed in computer controlled rotating mounts. The calibration unit is placed just after the folding mirror (M6) of MAST. Thus, during operations with MAST, calibration unit is used to generate known polarization by rotating QWP. The polarimeter response function or X-matrix is determined from a comparison between created input and measured output. The application of the inverse matrix (X^{-1}) on the measured Stokes vector removes the cross-talk arises due to properties of the polarimeter components.

In the thesis, we have presented spectropolarimetric observations of various active regions obtained with the imaging spectropolarimeter for MAST. For verification, we have made comparison of line-of-sight observations of a selected active region obtained from the HMI with that obtained from observations in the spectral line 6173 Å from MAST telescope. We found good agreement between both

the line-of-sight observations, considering the fact that MAST observations are limited by atmospheric seeing.

It is important to note that MAST is a nine mirror system with two off-axis parabolic and seven plane oblique mirrors, the oblique reflections of these mirrors complicate the measurement as the instrumental polarization corrupts the incoming radiation. In order to get the vector magnetic field observed Stokes profiles need to corrected for telescope polarization. We have planned to obtain the telescope polarization matrix both theoretically and experimentally. The thesis is concluded with a discussion on the ongoing experiment for the determination of telescope matrix using a sheet linear polarizer.

6.2 Future Plan

As discussed in the previous chapter, it is very clear that for deriving the vector magnetic field accurately from the observed Stokes profiles it is required to remove the effect of instrumental polarization of the telescope from the observations. It is important to note that MAST is a nine mirror system with two off-axis parabolic and seven plane oblique mirrors, the oblique reflections of these mirrors complicates the measurement as the instrumental polarization corrupts the incoming radiation. We have planned to obtain the instrumental polarization of the telescope both theoretically and experimentally as discussed below.

6.2.1 Instrumental polarization of the telescope

Knowledge of instrumental polarization is important in order to measure the polarization properties of the source accurately by avoiding cross-talk between different Stokes parameters. The following are planned to obtain the polarization induced by MAST telescope.

- We plan to derive the polarization induced by the two parabolic and seven

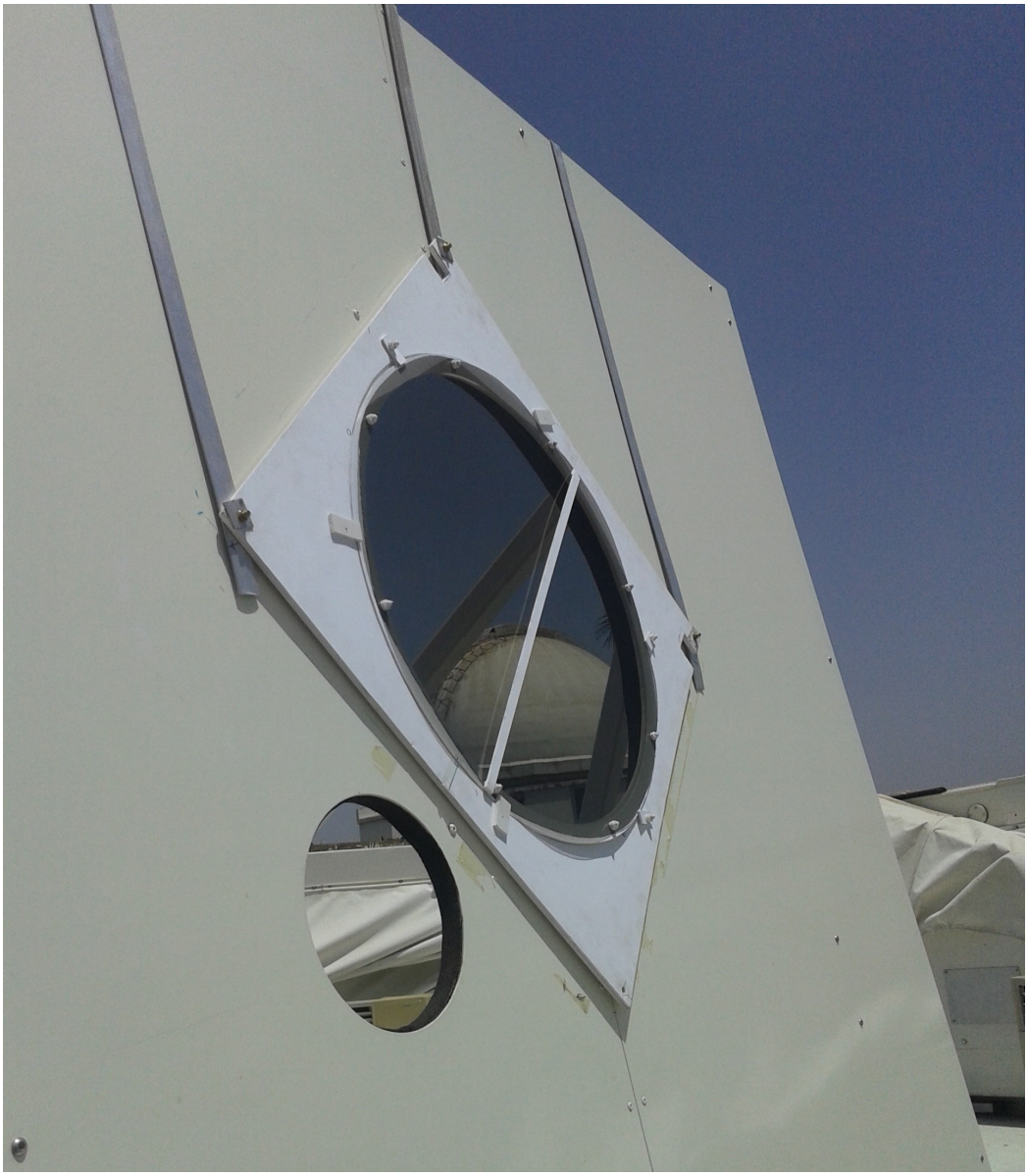

Figure 6.1: Sheet polarizer is placed in a rotating mount on the sunshield of MAST.

flat mirrors analytically by including different parameters of the mirrors. This includes the derivation of Mueller matrices for each of the components.

- We will cross-check these Mueller matrices by using optical design software, ZEMAX^{TM}. We plan to use the ZEMAX for deriving instrumental polarization due to entire optical system, which may be too complicated to derive analytically.

- We plan to verify the derived instrumental polarization experimentally using a sheet polarizer in a rotating mount in front of the primary mirror (Figure 6.1). We will determine the telescope matrix by measuring the different known polarization generated by rotating linear polarizer, with the polarimeter. This experiment has been already started where sheet polarizer with a rotating mount has been mounted on the sunshield as shown in Figure 6.1.

References

Bahcall, J. N.: 2001, *Nature* **412**, 29

Bahcall, J. N., Huebner, W. F., Lubow, S. H., Parker, P. D., and Ulrich, R. K.: 1982, *Reviews of Modern Physics* **54**, 767

Barthol, P., Gandorfer, A., Solanki, S. K., Schüssler, M., Chares, B., Curdt, W., Deutsch, W., Feller, A., Germerott, D., Grauf, B., Heerlein, K., Hirzberger, J., Kolleck, M., Meller, R., Müller, R., Riethmüller, T. L., Tomasch, G., Knölker, M., Lites, B. W., Card, G., Elmore, D., Fox, J., Lecinski, A., Nelson, P., Summers, R., Watt, A., Martínez Pillet, V., Bonet, J. A., Schmidt, W., Berkefeld, T., Title, A. M., Domingo, V., Gasent Blesa, J. L., Del Toro Iniesta, J. C., López Jiménez, A., Álvarez-Herrero, A., Sabau-Graziati, L., Widani, C., Haberler, P., Härtel, K., Kampf, D., Levin, T., Pérez Grande, I., Sanz-Andrés, A., and Schmidt, E.: 2011, *Solar Phys.* **268**, 1

Beck, C., Bellot Rubio, L. R., Kentischer, T. J., Tritschler, A., and Del Toro Iniesta, J. C.: 2010, *Astron. Astrophys.* **520**, A115

Beck, C., Schmidt, W., Kentischer, T., and Elmore, D.: 2005, *Astron. Astrophys.* **437**, 1159

Bello González, N. and Kneer, F.: 2008, *Astron. Astrophys.* **480**, 265

Bendlin, C., Volkmer, R., and Kneer, F.: 1992, *Astron. Astrophys.* **257**, 817

Bhatnagar, A. and Livingston, W.: 2005, *Fundamentals Of Solar Astronomy. Series: World Scientific Series in Astronomy and Astrophysics, ISBN: ¡ISBN¿978-981-238-244-3¡/ISBN¿. WORLD SCIENTIFIC, Edited by Arvind Bhatnagar and William Livingston, vol. 6* 6

Born, M. and Wolf, E.: 1999, *Principles of Optics*, Cambridge University Press, 7 edition

Borrero, J. M. and Ichimoto, K.: 2011, *Living Reviews in Solar Physics* **8**, 4

Capobianco, G., Crudelini, F., Zangrilli, L., Buscemi, C., and Fineschi, S.: 2008

Cavallini, F.: 2006, *Solar Phys.* **236**, 415

Chandrasekhar, S.: 1960, *Radiative transfer*

Collett, E.: 1992, *Polarized light. Fundamentals and applications*

De Gennes, P. G.: 1969, *Physics Letters A* **30**, 454

de Gennes, P. G., Prost, J., and Pelcovits, R.: 1995, *Physics Today* **48**, 70

de Juan Ovelar, M., Snik, F., Keller, C. U., and Venema, L.: 2014, *Astron. Astrophys.* **562**, A8

Del Toro Iniesta, J. C.: 2003, *Introduction to Spectropolarimetry*

del Toro Iniesta, J. C. and Collados, M.: 2000, *Applied Optics* **39**, 1637

Del Toro Iniesta, J. C. and Martínez Pillet, V.: 2012, *Astro Phys. Suppl. Series* **201**, 22

Denis, S., Coucke, P., Gabriel, E., Delrez, C., and Venkatakrishnan, P.: 2008, in *Ground-based and Airborne Telescopes II*, Vol. 7012 of *Proceedings of SPIE International Conference on Optics and Photonics 2015*, p. 701235

Denis, S., Coucke, P., Gabriel, E., Delrez, C., and Venkatakrishnan, P.: 2010, in *Ground-based and Airborne Telescopes III*, Vol. 7733 of *Proceedings of SPIE International Conference on Optics and Photonics 2015*, p. 773335

Denker, C., Balthasar, H., Hofmann, A., Bello González, N., and Volkmer, R.: 2010, in *Society of Photo-Optical Instrumentation Engineers (SPIE) Conference Series*, Vol. 7735 of *Society of Photo-Optical Instrumentation Engineers (SPIE) Conference Series*, p. 6

Durrant, C. J.: 1988, *The atmosphere of the sun*

Foukal, P. V.: 2004, *Solar Astrophysics, 2nd, Revised Edition*

Golub, L. and Pasachoff, J. M.: 2009, *The Solar Corona*

Haller, I.: 1975, *Progress in Solid State Chemistry* **10**, 103

Hanle, W.: 1924, *Zeitschrift fur Physik* **30**, 93

Hecht, E.: 2001, *Optics 4th edition*

Heredero, R. L., Uribe-Patarroyo, N., Belenguer, T., Ramos, G., Sánchez, A., Reina, M., Martínez Pillet, V., and Álvarez-Herrero, A.: 2007, *Applied Optics* **46**, 689

Ichimoto, K., Lites, B., Elmore, D., Suematsu, Y., Tsuneta, S., Katsukawa, Y., Shimizu, T., Shine, R., Tarbell, T., Title, A., Kiyohara, J., Shinoda, K., Card, G., Lecinski, A., Streander, K., Nakagiri, M., Miyashita, M., Noguchi, M., Hoffmann, C., and Cruz, T.: 2008, *Solar Phys.* **249**, 233

Iniesta, J. C. D. T. and Pillet, V. M.: 2012, *The Astrophysical Journal Supplement Series* **201(2)**, 22

Jochum, L., Herrero, P., Collados, M., Martinez Pillet, V., Rodriguez, J., and Lopez, M.: 2003, in S. Fineschi (ed.), *Polarimetry in Astronomy*, Vol. 4843 of

Proceedings of SPIE International Conference on Optics and Photonics 2015, pp 30–38

Kuhn, J. R. and Hawley, S. L.: 1999, *Pub. Astron. Soc. Pac.* **111**, 601

Lagg, A., Lites, B., Harvey, J., Gosain, S., and Centeno, R.: 2015, *ArXiv e-prints*

Landolfi, M. and Landi Degl'Innocenti, E.: 1982, *Solar Phys.* **78**, 355

Lang, K. R.: 2006, *Sun, Earth and Sky*

Leibacher, J. W., Noyes, R. W., Toomre, J., and Ulrich, R. K.: 1985, *Scientific American* **253**, 48

Leighton, R. B., Noyes, R. W., and Simon, G. W.: 1962, *Astrophys. J.* **135**, 474

Leka, K. D. and Rangarajan, K. E.: 2001, *Solar Phys.* **203**, 239

Lites, B. W.: 1987, *Applied Optics* **26**, 3838

Ma, L., Zhou, W., Zhou, G., and Zhang, J.: 2015, *Astron. Astrophys.* **583**, A110

Martinez Pillet, V., Bonet, J. A., Collados, M. V., Jochum, L., Mathew, S., Medina Trujillo, J. L., Ruiz Cobo, B., del Toro Iniesta, J. C., Lopez Jimenez, A. C., Castillo Lorenzo, J., Herranz, M., Jeronimo, J. M., Mellado, P., Morales, R., Rodriguez, J., Alvarez-Herrero, A., Belenguer, T., Heredero, R. L., Menendez, M., Ramos, G., Reina, M., Pastor, C., Sanchez, A., Villanueva, J., Domingo, V., Gasent, J. L., and Rodriguez, P.: 2004, in J. C. Mather (ed.), *Optical, Infrared, and Millimeter Space Telescopes*, Vol. 5487 of *Society of Photo-Optical Instrumentation Engineers (SPIE) Conference Series*, pp 1152–1164

Martínez Pillet, V., Del Toro Iniesta, J. C., Álvarez-Herrero, A., Domingo, V., Bonet, J. A., González Fernández, L., López Jiménez, A., Pastor, C., Gasent Blesa, J. L., Mellado, P., Piqueras, J., Aparicio, B., Balaguer, M., Ballesteros, E., Belenguer, T., Bellot Rubio, L. R., Berkefeld, T., Collados, M., Deutsch,

W., Feller, A., Girela, F., Grauf, B., Heredero, R. L., Herranz, M., Jerónimo, J. M., Laguna, H., Meller, R., Menéndez, M., Morales, R., Orozco Suárez, D., Ramos, G., Reina, M., Ramos, J. L., Rodríguez, P., Sánchez, A., Uribe-Patarroyo, N., Barthol, P., Gandorfer, A., Knoelker, M., Schmidt, W., Solanki, S. K., and Vargas Domínguez, S.: 2011, *Solar Phys.* **268**, 57

Mathew, S. K.: 2009, in S. V. Berdyugina, K. N. Nagendra, and R. Ramelli (eds.), *Solar Polarization 5: In Honor of Jan Stenflo*, Vol. 405 of *Astronomical Society of the Pacific Conference Series*, p. 461

Mathew, S. K., Bayanna, A. R., Tiwary, A. R., Ramya, B., and Venkatakrishnan, P.: 2017, *Accepted in Solar Physics*

Mickey, D. L., Canfield, R. C., Labonte, B. J., Leka, K. D., Waterson, M. F., and Weber, H. M.: 1996, *Solar Phys.* **168**, 229

Mitalas, R. and Sills, K. R.: 1992, *Astrophys. J.* **401**, 759

Pesnell, W. D., Thompson, B. J., and Chamberlin, P. C.: 2012, *Solar Phys.* **275**, 3

Puschmann, K. G.: 2016, *ArXiv e-prints*

Raja Bayanna, A., Mathew, S. K., Venkatakrishnan, P., and Srivastava, N.: 2014, *Solar Phys.* **289**, 4007

Rempel, M. and Schlichenmaier, R.: 2011, *Living Reviews in Solar Physics* **8**, 3

Saleh, B. E. A. and Teich, M. C.: 2007, *JOHN WILEY & SONS, INC.*

Sankarasubramanian, K., Elmore, D. F., Lites, B. W., Sigwarth, M., Rimmele, T. R., Hegwer, S. L., Gregory, S., Streander, K. V., Wilkins, L. M., Richards, K., and Berst, C.: 2003, in S. Fineschi (ed.), *Polarimetry in Astronomy*, Vol. 4843 of *Society of Photo-Optical Instrumentation Engineers (SPIE) Conference Series*, pp 414–424

Scharmer, G. B., Narayan, G., Hillberg, T., de la Cruz Rodríguez, J., Löfdahl, M. G., Kiselman, D., Sütterlin, P., van Noort, M., and Lagg, A.: 2008, *Astrophys. J. Lett.* **689**, L69

Scherrer, P. H., Schou, J., Bush, R. I., Kosovichev, A. G., Bogart, R. S., Hoeksema, J. T., Liu, Y., Duvall, T. L., Zhao, J., Title, A. M., Schrijver, C. J., Tarbell, T. D., and Tomczyk, S.: 2012, *Solar Phys.* **275**, 207

Schou, J., Scherrer, P. H., Bush, R. I., Wachter, R., Couvidat, S., Rabello-Soares, M. C., Bogart, R. S., Hoeksema, J. T., Liu, Y., Duvall, T. L., Akin, D. J., Allard, B. A., Miles, J. W., Rairden, R., Shine, R. A., Tarbell, T. D., Title, A. M., Wolfson, C. J., Elmore, D. F., Norton, A. A., and Tomczyk, S.: 2012, *Solar Phys.* **275**, 229

Socas-Navarro, H., Elmore, D., Pietarila, A., Darnell, A., Lites, B. W., Tomczyk, S., and Hegwer, S.: 2006, *Solar Phys.* **235**, 55

Solanki, S. K.: 2003, *Astron. Astrophys. Rev.* **11**, 153

Spiegel, E. A. and Zahn, J.-P.: 1992, *Astron. Astrophys.* **265**, 106

Stenflo, J. O.: 2015, *Space Sci. Rev.*

Stix, M.: 2004, *The Sun*, Springer-verlag Gmbh, 2 edition

Terrier, P., Charbois, J. M., and Devlaminck, V.: 2010, *Applied Optics* **49**, 4278

Tiwary, A. R., Bayanna, A. R., and Mathew, S. K.: 2017a, *Appl. Opt.* **56(14)**, 4180

Tiwary, A. R., Mathew, S. K., Bayanna, A. R., Venkatakrishnan, P., and Yadav, R.: 2017b, *Solar Physics* **292(4)**, 49

Tomczyk, S., Casini, R., de Wijn, A. G., and Nelson, P. G.: 2010, *Applied Optics* **49**, 3580

Tomczyk, S., Landi, E., Burkepile, J. T., Casini, R., DeLuca, E. E., Fan, Y., Gibson, S. E., Lin, H., McIntosh, S. W., Solomon, S. C., Toma, G., Wijn, A. G., and Zhang, J.: 2016, *Journal of Geophysical Research (Space Physics)* **121**, 7470

Tsuneta, S., Ichimoto, K., Katsukawa, Y., Nagata, S., Otsubo, M., Shimizu, T., Suematsu, Y., Nakagiri, M., Noguchi, M., Tarbell, T., Title, A., Shine, R., Rosenberg, W., Hoffmann, C., Jurcevich, B., Kushner, G., Levay, M., Lites, B., Elmore, D., Matsushita, T., Kawaguchi, N., Saito, H., Mikami, I., Hill, L. D., and Owens, J. K.: 2008, *Solar Phys.* **249**, 167

Ulrich, R. K.: 1970, *Astrophys. J.* **162**, 993

Unno, W. and Kato, S.: 1962, *Pub. Astron. Soc. Japan* **14**, 417

van Driel-Gesztelyi, L. and Green, L. M.: 2015, *Living Reviews in Solar Physics* **12(1)**, 1

Wiegelmann, T., Petrie, G. J. D., and Riley, P.: 2015, *Space Sci. Rev.*

Wiegelmann, T. and Sakurai, T.: 2012, *Living Reviews in Solar Physics* 9(5)

Yadav, R., Mathew, S. K., and Tiwary, A. R.: 2017, *Accepted in Solar Physics*

Zeeman, P.: 1897, *Astrophys. J.* **5**, 332

List of Publications

Publications in Journals

1. **Tiwary, A. R.**, Mathew, Shibu K., Bayanna, A. Raja, Venkatakrishnan, P., Yadav, Rahul, 2017. *Imaging Spectropolarimeter for the Multi-Application Solar Telescope at Udaipur Solar Observatory: Characterization of Polarimeter and Preliminary Observations.* Solar Physics, 292, 49.

2. **Tiwary, Alok Ranjan**, Bayanna, A. Raja, Mathew, Shibu K., 2017 *Estimation of order parameter of a Liquid crystal variable retarder using Hallers approximation.* Applied Optics, 56, 14.

3. Mathew, Shibu K., Bayanna, A. Raja, **Tiwary, Alok Ranjan**, Bireddy, R., Venkatakrishnan, P., 2017. *First observations from the Multi-Application Solar Telescope (MAST) narrow-band imager.* Solar Physics, 292, 106.

4. Yadav, Rahul, Mathew, Shibu K., **Tiwary, Alok Ranjan**, 2017, *SPIN: an inversion code for the photospheric spectral line*, Solar Physics, 292, 105.

Publications attached with thesis

1. **Tiwary, A. R.**, Mathew, Shibu K., Bayanna, A. Raja, Venkatakrishnan, P., Yadav, Rahul, 2017. *Imaging Spectropolarimeter for the Multi-Application Solar Telescope at Udaipur Solar Observatory: Characterization of Polarimeter and Preliminary Observations.* Solar Physics, 292, 49.

2. **Tiwary, A. R.**, Bayanna, A. Raja, Mathew, Shibu K., 2017 *Estimation of order parameter of a Liquid crystal variable retarder using Hallers approximation.* Applied Optics, 56, 14.

Solar Phys (2017) 292:49
DOI 10.1007/s11207-017-1076-5

Imaging Spectropolarimeter for the Multi-Application Solar Telescope at Udaipur Solar Observatory: Characterization of Polarimeter and Preliminary Observations

Alok Ranjan Tiwary[1,2] · Shibu K. Mathew[1] · A. Raja Bayanna[1] · P. Venkatakrishnan[1] · Rahul Yadav[1]

Received: 18 August 2016 / Accepted: 1 March 2017

Abstract The *Multi-Application Solar Telescope* (MAST) is a 50 cm off-axis Gregorian telescope that has recently become operational at the *Udaipur Solar Observatory* (USO). An imaging spectropolarimeter is being developed as one of the back-end instruments of MAST to gain a better understanding of the evolution and dynamics of solar magnetic and velocity fields. This system consists of a narrow-band filter and a polarimeter. The polarimeter includes a linear polarizer and two sets of liquid crystal variable retarders (LCVRs). The instrument is intended for simultaneous observations in the spectral lines 6173 Å and 8542 Å, which are formed in the photosphere and chromosphere, respectively. In this article, we present results from the characterization of the LCVRs for the spectral lines of interest and the response matrix of the polarimeter. We also present preliminary observations of an active region obtained using the spectropolarimeter. For verification purposes, we compare the Stokes observations of the active region obtained from the *Helioseismic Magnetic Imager* (HMI) onboard the *Solar Dynamics Observatory* (SDO) with that of MAST observations in the spectral line 6173 Å. We find good agreement between the two observations, considering the fact that MAST observations are limited by seeing.

Keywords Instrumentation · Polarimeter · Polarization · Magnetic fields

1. Introduction

Solar activity is driven by the spatio-temporal distribution of the magnetic field (*e.g.* Solanki, 2003; Borrero and Ichimoto, 2011; Stix, 2004). Precise measurements of the magnetic field in the solar atmosphere are therefore of fundamental importance. For more than a century, the Zeeman effect (Zeeman, 1897) has been recognized as the most authentic tool to derive the magnetic field of sunspots and pores in the photosphere (Stenflo, 2015, and references therein). With the advancement of instrumentation capabilities, we can now measure the

A.R. Tiwary
atiwary@prl.res.in

1 Udaipur Solar Observatory, Physical Research Laboratory, Udaipur, Rajasthan, 313001, India

2 Indian Institute of Technology, Gandhinagar 382424, Gujarat, India

Published online: 27 March 2017

Zeeman signals of a small-scale structure in the photosphere as well as in the chromosphere (Trujillo Bueno, 2014; Wiegelmann, Petrie, and Riley, 2015). However, the Zeeman effect becomes insensitive for estimates of the weak field in the corona. Therefore, we rely on the Hanle effect (Hanle, 1924) for coronal magnetic field measurements. In special cases, these two effect can be combined to obtain magnetic field measurements in different atmospheric layers of the Sun (Lagg *et al.*, 2015).

In the presence of a magnetic field, light becomes polarized and depolarized. The polarization of light is described in terms of the Stokes parameters I, Q, U, and V (Chandrasekhar, 1960; Born and Wolf, 1999), where I gives the total intensity, Q and U represent the linear polarization, and V represents the circular polarization. The spectropolarimeter consists of a filtergraph/spectrograph and a polarimeter and is employed to derive the solar vector magnetic fields by measuring Stokes I, Q, U, and V. Generally, two different techniques have been commonly used for spectral analysis: (1) imaging-based (filter), and (2) slit-based. For a polarization analysis, either a single-beam polarimeter or a dual-beam polarimeter is employed. In imaging-based spectropolarimetry, 2D images are obtained in a sequence by tuning a narrow-band filter to different wavelengths along the spectral line profile of interest. Modern imaging spectropolarimeters employ either a single or a multiple Fabry–Perot (FP) etalon as narrow-band filters because of their high transmission and fast tuning capability. A few examples of the currently working imaging spectropolarimeters are the *GREGOR Fabry–Perot instrument* (GFPI; Denker *et al.*, 2010, Puschmann, 2016, and references therein), the KIS/IAA *Visible Imaging Polarimeter* (VIP; Beck *et al.*, 2010), the *CRisp Imaging Spectro-Polarimeter* (CRISP, Scharmer *et al.*, 2008), the Göttingen spectropolarimeter (Bendlin, Volkmer, and Kneer, 1992; Bello González and Kneer, 2008), the *Interferometric BIdimensional Spectrometer* (IBIS; Cavallini, 2006), and the *Imaging Vector Magnetograph* (IVM; Mickey *et al.*, 1996). The *Imaging Magnetograph eXperiment* (IMaX; Martínez Pillet *et al.*, 2011), which has flown onboard the *Sunrise* balloon mission (Barthol *et al.*, 2011), is another example of an imaging spectropolarimeter using a voltage-tunable lithium niobate Fabry–Perot etalon. These instruments differ in the number of etalons and the optical configuration (telecentric or collimated). On the other hand, a slit-based spectropolarimeter obtains the spectrum by scanning the required field of view (FOV) in sequence. Examples of slit-based spectropolarimeters are the *Diffraction Limited Spectro-Polarimeter* (DLSP; Sankarasubramanian *et al.*, 2003), the *POlarimetric LIttrow Spectrograph* (POLIS; Beck *et al.*, 2005), the *Spectro-Polarimeter for Infrared and Optical Regions* (SPINOR; Socas-Navarro *et al.*, 2006), and spectropolarimeter of the *Solar Optical Telescope* (SOT) onboard the *Hinode* spacecraft (Ichimoto *et al.*, 2008; Tsuneta *et al.*, 2008). Based on the scientific requirement, either of the two techniques described above are preferred. However, with the advances in technology, these two techniques yield similar results.

In order to measure the vector magnetic field in the solar atmosphere, we have developed an imaging spectropolarimeter for the *Multi-Application Solar Telescope* (MAST) (Denis *et al.*, 2008, 2010; Mathew, 2009) that has recently been installed at the lake site of the Udaipur Solar Observatory (USO). It is an off-axis Gregorian telescope with a 50 cm aperture. Along with adaptive optics system, the telescope is designed to provide near diffraction-limited observations. One of the scientific objectives of MAST is to study the evolution of the vector magnetic field in the solar atmosphere at different heights and its connection to various solar activities. The imaging spectropolarimeter for MAST consists of a narrow-band imager (Raja Bayanna *et al.*, 2014) and a polarimeter, which are used to measure the Stokes vector at two different wavelengths, *i.e.* at 6173 Å and 8542 Å, corresponding to photospheric and chromospheric heights, respectively.

This article is organized in the following manner. Section 2 describes the design of the polarimeter and the modulation scheme to measure the Stokes vector. The characterization of the liquid crystal variable retarders (LCVRs) with voltage and temperatures are discussed in Section 3. In Section 4 we explain the response matrix of the polarimeter derived using an experimental setup in the laboratory. Preliminary observations obtained with our instrument are presented in Section 5. A summary of the article is provided in Section 6.

2. Polarimeter Schematic and Components

A polarimeter measures the polarization of light by modulating the input polarization into measurable intensities. In general, the polarization analysis can be made in two ways (Del Toro Iniesta, 2003, and references therein): (a) Temporal polarization modulation, or single-beam polarimetry. Here, the different polarization measurements are obtained sequentially. The time gap between the measurements could introduce seeing-related spurious signals in the difference image (Lites, 1987; Leka and Rangarajan, 2001). This can be minimized either by compensating for the atmospheric turbulence by adaptive optics, or by implementing a very fast modulation scheme, wherein one modulation cycle is completed before atmospheric seeing changes completely, or by both. However, this imposes stringent requirements of the polarization modulator. (b) Spatial polarization modulation or dual-beam polarimetry (Lites, 1987) can also be used for the polarization analysis. Here the orthogonal polarization states are separated by means of the polarizing beam splitter or displacer, and the two beams are recorded simultaneously. This cancels out the fluctuations in the Stokes I to the other Stokes parameters that is caused by atmospheric seeing (Martínez Pillet *et al.*, 2011). Since both the beams are used for the final computation of the Stokes parameters, this method improves the signal-to-noise ratio (S/N) by a factor of $\sqrt{2}$ as compared to the single-beam polarimetry. However, different optical paths for the measurements of two polarization states might introduce a systematic error. This places a stringent requirement on the quality of the two optical paths in the experimental setup. It also requires a larger area of the detector to accommodate a larger FOV.

Although dual-beam polarimetry is more advantageous than single-beam polarimetry, we preferred to use the single-beam setup to perform the polarization analysis over a larger FOV. The fast modulation scheme with liquid crystal variable retarders along with a matching fast camera readout enable us to complete the modulation cycle before the seeing changes significantly. With a suitably large format camera and a polarizing beam displacer, we plan to implement the dual-beam spectropolarimetry at MAST at a later stage.

The main components of the MAST polarimeter are LCVRs for polarization modulation and a Glan–Thompson polarizer as analyzer. Many recent polarization modulators also use liquid crystals, in which retardance (as in nematic liquid crystals) or fast axis (as in ferroelectric liquid crystals) can be changed by applying voltages (Heredero *et al.*, 2007, and references therein). These modulators allow us to implement fast modulation schemes by avoiding mechanical motions and beam wobble as in the case of rotating retarders (Heredero *et al.*, 2007). In MAST, two sets of LCVRs along with a linear polarizer are used to obtain the Stokes parameters. LCVRs for the MAST polarimeter are custom-made nematic liquid crystal devices with an aperture size of 80 mm, procured from Meadowlark Optics, USA. Figure 1 shows the schematic of the MAST polarimeter. The fast axes of LCVR1 and LCVR2 are fixed at 0° and 45° with respect to the linear polarizer (LP), respectively. Light from the telescope enters through LCVR1, passes through LCVR2, and exits from the LP. Both LCVRs and the LP are mounted on rotating mounts to adjust for the angles. The

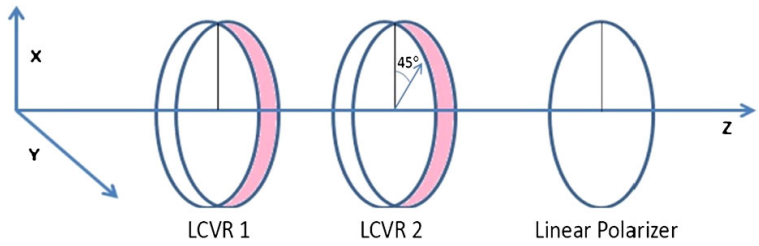

Figure 1 Schematic layout of the polarimeter for MAST. The fast axis of the first liquid crystal variable retarder (LCVR1) and the second liquid crystal variable retarder (LCVR2) are kept at 0° and 45° with respect to the linear polarizer.

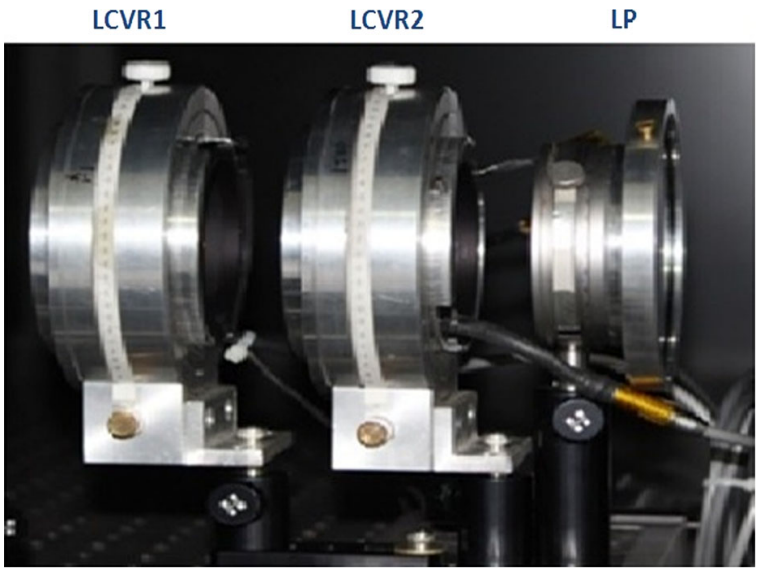

Figure 2 Imaging polarimeter for MAST at USO. From left to right, we show LCVR1, LCVR2, and the linear polarizer. LCVR1 and LCVR2 are kept at 0° and 45° with respect to the linear polarizer (LP), respectively.

photograph of the installed system is shown in Figure 2. The temperature of the LCVRs is actively controlled using flexible heaters that are fixed on the holder; a temperature sensor in a closed loop provides a thermal stability of $\pm 1°$C.

The retardance of the LCVR can be changed by applying voltages. The modulation voltages for the LCVRs are supplied from a Meadowlark digital interface. The amplitude of the basic 2 kHz square waveform can be adjusted by an input DC voltage or counts provided from the software through a USB computer interface. Modulation voltages in the range of 0 – 10 V with 16-bit accuracy can be applied to the LCVRs from this interface. C-programs have been written for the image acquisition in synchronization with the modulation voltages. The modulation scheme employed here is described in the following subsection.

2.1. Modulation Scheme for the MAST Polarimeter

As discussed in the previous section, the MAST polarimeter consists of two LCVRs and a linear polarizer. The Stokes vector of input light ($\boldsymbol{S}_{\rm in}$) at LCVR1 and the Stokes vector of output light at LP ($\boldsymbol{S}_{\rm out}$) are related using the Mueller-matrix formalism by the following equation:

$$\boldsymbol{S}_{\rm out} = \mathbf{M}_{\rm P}\mathbf{M}_{\rm LC2}(\gamma, \theta_2)\mathbf{M}_{\rm LC1}(\delta, \theta_1)\boldsymbol{S}_{\rm in} = \mathbf{M}_S\boldsymbol{S}_{\rm in}, \tag{1}$$

where $\mathbf{M}_{\rm P}$, $\mathbf{M}_{\rm LC1}(\delta, \theta_1)$, and $\mathbf{M}_{\rm LC2}(\gamma, \theta_2)$ are the Mueller matrices of the linear polarizer, LCVR1 and LCVR2, respectively. The fast axes of LCVR1 and LCVR2 with respect to the transmission axis of the linear polarizer is represented by θ_1 and θ_2, respectively. The retardance of LCVR1 and LCVR2 are given by δ and γ, respectively. $\mathbf{M}_S$ is the resulting Mueller matrix of the polarimeter for a particular value of δ, γ, θ_1, and θ_2.

Using the Mueller matrix of the retarder and polarizer in the Equation (1), we can express the intensity I, measured at the CCD, as a linear combination of all the input Stokes parameters,

$$I_j = \boldsymbol{S}^0_{\rm out} = 1\boldsymbol{S}^0_{\rm in} + a_j \boldsymbol{S}^1_{\rm in} + b_j \boldsymbol{S}^2_{\rm in} + c_j \boldsymbol{S}^3_{\rm in}, \tag{2}$$

where the parameters $[1, a_j, b_j, c_j]$ are the first row of $\mathbf{M}_S$, which depends on θ_1, θ_2, δ, and γ. Here j runs over the number of observations (from 1 to n). From Equation (2), we can measure n number of intensities for different combinations of retardances and fast axis orientations of the two LCVRs. However, it is always preferred to have a minimum number of intensity measurements to infer all the Stokes parameters (del Toro Iniesta and Collados, 2000). For vector polarimetry, at least four measurements ($n \geq 4$) are needed, while longitudinal polarimetry can be made with only two measurements ($n \geq 2$). For n intensity measurements, a modulation scheme is therefore fully characterized by a $(n \times 4)$ modulation matrix $\mathbf{O}$ built from the n first rows of $\mathbf{M}_S$,

$$I_{\rm meas} = \mathbf{O}\boldsymbol{S}_{\rm in}. \tag{3}$$

The Stokes vector is derived using the equation

$$\boldsymbol{S}_{\rm in} = \mathbf{O}^{-1}\mathbf{I}_{\rm meas} = \mathbf{D}I_{\rm meas}. \tag{4}$$

If $n = 4$, then $\mathbf{O}$ is a 4×4 matrix, so its inverse will be unique. If $n = 6$, however, then $\mathbf{O}$ is 6×4 matrix, which is not a square matrix, and its inverse will not be unique. Hence, when $\mathbf{D}$ is not a square matrix, it is determined using the equation (del Toro Iniesta and Collados, 2000)

$$\mathbf{D} = \left(\mathbf{O}^{\rm T}\mathbf{O}\right)^{-1}\mathbf{O}^{\rm T}. \tag{5}$$

The efficiency of the modulation scheme is defined as

$$e_i = \left(n \sum_{j=1}^{n} \mathbf{D}^2_{ij}\right)^{-1/2}, \tag{6}$$

where, e_1, e_2, e_3, and e_4 are the efficiencies for measuring the Stokes parameter I, Q, U, and V, respectively.

For a four-measurement modulation scheme ($n = 4$),

$$I_{\rm meas} = \begin{bmatrix} I_1 \\ I_2 \\ I_3 \\ I_4 \end{bmatrix} = \mathbf{O} \begin{bmatrix} S^0_{\rm in} \\ S^1_{\rm in} \\ S^2_{\rm in} \\ S^3_{\rm in} \end{bmatrix}, \tag{7}$$

where $\mathbf{O}$ is the modulation matrix, given as

$$\mathbf{O} = \begin{pmatrix} 1 & a_1 & b_1 & c_1 \\ 1 & a_2 & b_2 & c_2 \\ 1 & a_3 & b_3 & c_3 \\ 1 & a_4 & b_4 & c_4 \end{pmatrix}. \tag{8}$$

For the polarimeter configuration shown in Figure 1, the orientation of the fast axes of LCVR1 and LCVR2 is fixed at $\theta_1 = 0°$, and $\theta_2 = 45°$, respectively (Martinez Pillet *et al.*,

Table 1 Four-measurement modulation scheme (Martinez Pillet *et al.*, 2004) for vector polarimetry.

δ (°)	γ (°)	Measured intensity $I_{\rm meas}$
315.0	305.264	$I_1 = I + Q/\sqrt{3} + U/\sqrt{3} + V/\sqrt{3}$
315.0	54.736	$I_2 = I + Q/\sqrt{3} - U/\sqrt{3} - V/\sqrt{3}$
225.0	125.264	$I_3 = I - Q/\sqrt{3} - U/\sqrt{3} + V/\sqrt{3}$
225.0	234.736	$I_4 = I - Q/\sqrt{3} + U/\sqrt{3} - V/\sqrt{3}$

Table 2 Six-measurement modulation scheme (Tomczyk *et al.*, 2010) for vector polarimetry.

δ (°)	γ (°)	Measured intensity $I_{\rm meas}$
180.0	360.0	$I_1 = I + Q$
180.0	180.0	$I_2 = I - Q$
090.0	090.0	$I_3 = I + U$
090.0	270.0	$I_4 = I - U$
180.0	090.0	$I_5 = I + V$
180.0	270.0	$I_6 = I - V$

2004). Using different combinations of retardances of LCVR1 and LCVR2, *i.e.*, δ and γ, four- and six-measurement modulation schemes are implemented for vector polarimetry at MAST. The modulation schemes of the four and six measurements are listed in Tables 1 and 2.

The modulation matrix (**O**) for the four measurement modulation scheme is given by

$$\mathbf{O} = \begin{pmatrix} 1 & 0.57735 & 0.57735 & 0.57735 \\ 1 & 0.57735 & -0.57735 & -0.57735 \\ 1 & -0.57735 & -0.57735 & 0.57735 \\ 1 & -0.57735 & 0.57735 & -0.57735 \end{pmatrix}. \tag{9}$$

For this modulation scheme, the maximum efficiencies are determined from Equations (5) and (6) as $e_1 = 1$, $e_2 = 0.57735$, $e_3 = 0.57735$, and $e_4 = 0.57735$.

Similarly, the modulation matrix for the six-measurement modulation scheme can be expressed as a 6×4 matrix,

$$\mathbf{O} = \begin{pmatrix} 1 & 1 & 0 & 0 \\ 1 & -1 & 0 & 0 \\ 1 & 0 & 1 & 0 \\ 1 & 0 & -1 & 0 \\ 1 & 0 & 0 & 1 \\ 1 & 0 & 0 & -1 \end{pmatrix}. \tag{10}$$

For this modulation scheme, the maximum efficiencies are determined as $e_1 = 1$, $e_2 = 0.57735$, $e_3 = 0.57735$, and $e_4 = 0.57735$. These are the maximum efficiencies that an ideal polarimeter system can have (del Toro Iniesta and Collados, 2000).

The two modulation schemes provide equal modulation efficiencies for the measurement of Q, U, and V (Del Toro Iniesta and Martínez Pillet, 2012). Either of these modulation schemes can be used for the measurement of all the Stokes parameters in vector polarimetry. Measurement of all the Stokes parameters is required to obtain the vector magnetic field, while the longitudinal magnetic field can only be obtained from Stokes I and V. The

Table 3 Modulation scheme for longitudinal polarimetry.

δ (°)	γ (°)	Measured intensity I_{meas}
360.0	90.0	$I_1 = I - V$
360.0	270.0	$I_2 = I + V$

longitudinal measurement can be obtained by two intensity measurements. The modulation scheme for longitudinal polarimetry is listed in Table 3.

The relation between the incoming Stokes vector and the measured Stokes vector is given as (Beck *et al.*, 2005)

$$\boldsymbol{S}_{\text{meas}} = \mathbf{X}.\boldsymbol{S}_{\text{in}}, \tag{11}$$

where $\mathbf{X}$ is the 4×4 square matrix known as response matrix, which includes all the processes for polarimetric measurement such as properties of optical components, modulation schemes, and their demodulation (de Juan Ovelar *et al.*, 2014; Beck *et al.*, 2005). Furthermore, $\mathbf{X}$ can be expressed as

$$\mathbf{X} = \mathbf{DO}. \tag{12}$$

In the response matrix of an ideal polarimeter, the diagonal elements will be unity and the off-diagonal elements will be zero. However, in practice, the off-diagonal elements of the response matrix will have non-zero values that represent the cross-talk between the Stokes parameters that is introduced for several reasons (de Juan Ovelar *et al.*, 2014).

3. Characterization of the LCVRs

The LCVR retardance can be tuned by applying voltages. The voltage dependence of the LCVR retardance is given by the equation (Saleh and Teich, 2007)

$$\delta = \frac{2\pi d}{\lambda}\left(\left(\frac{\sin^2(\Theta)}{n_{\text{o}}^2} + \frac{\cos^2(\Theta)}{n_{\text{e}}^2}\right)^{-\frac{1}{2}} - n_{\text{e}}\right), \tag{13}$$

where n_{o} and n_{e} are the refractive indices of the ordinary and extraordinary beam, and the equilibrium tilt angle Θ for liquid crystal molecules depends on the applied voltage, which is described by

$$\Theta = 0, \quad \forall V \leq V_{\text{C}} = \frac{\pi}{2} - 2\tan^{-1}\left(\exp\left(-\frac{V - V_{\text{C}}}{V_0}\right)\right), \quad \forall V > V_{\text{C}},$$

where V is the applied voltage, V_{C} is the critical voltage at which the tilting process begins, and V_0 is a constant.

The change in the LCVR retardance that is due to temperature can be expressed by a semi-empirical formula (Li, Gauzia, and Wu, 2004; Capobianco *et al.*, 2008),

$$\delta = \delta_0 A = \delta_0\left(1 - \frac{T}{T_{\text{C}}}\right)^{\alpha}, \tag{14}$$

where δ_0 is the retardance for $A = 1$; A denotes an order parameter that describes the orientational order of the nematic liquid crystal. For completely random and isotropic liquid

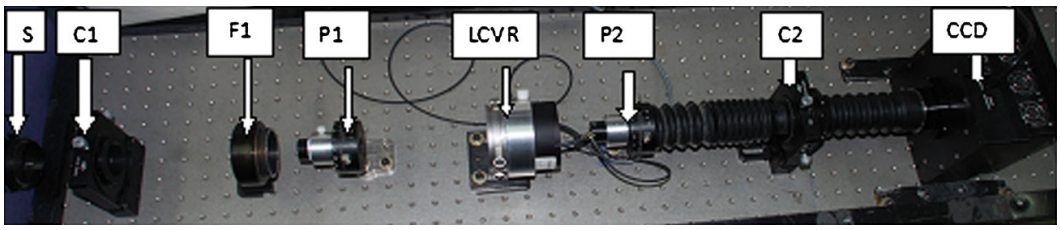

Figure 3 Experimental setup for the calibration of LCVRs: In this setup, a light beam coming from a pinhole source is collimated using a lens C1. Then the collimating light passes through an interference filter (F1), linear polarizer (P1), and LCVR, whose fast axis is kept at 45° with respect to P1. Finally, light is imaged by the imaging lens (C2) on the CCD, which is placed in the focal plane of the imaging lens after passing through analyzer P2.

crystals, $A = 0$, while for a perfectly aligned sample, $A = 1$ (Haller, 1975). For a typical liquid crystal sample, A is in the range of 0.3 to 0.8 and generally decreases with temperature (de Gennes, Prost, and Pelcovits, 1995; Shin-Tson Wu, 2001). In particular, a sharp drop of A to zero value is observed when the system undergoes a phase transition from the liquid crystal phase into the isotropic phase. Thus, T_C is the nematic–isotropic transition temperature and α is the critical exponent related to the phase transition. In order to use the LCVRs in the modulation scheme discussed in the previous section, it is important to exactly know the retardance and its dependence on voltage and temperature.

3.1. Experimental Setup and Theory

The experimental setup for the characterization of LCVRs is shown in Figure 3. We used a stabilized DC lamp as a white-light source (S) along with a diffuser to obtain uniform intensity. A lens (C1) is placed in front of the pinhole to collimate the light. An interference filter (F1) is used to select the particular wavelength for which characterization of the LCVRs is carried out. The LCVR is placed in between two Glan–Thompson polarizing prisms (P1 and P2). Glan–Thompson polarizing prisms offer a high extinction ratio (1×10^{-6}) and high transmittance for a wavelength band between 3500 – 23000 Å (Hecht, 2001). Another lens (C2) is placed after the analyzer (P2) to image the beam onto a CCD camera to measure the intensity of the output light. The incoming light is linearly polarized by the polarizer P1. After being retarded by the LCVR, whose fast axis is at 45°, the light is analyzed by the second polarizer P2. Polarizer P2 is mounted on a computer-controlled rotation stage to measure the intensities at two different orientations. The Stokes vector $\boldsymbol{S}_{\text{out}}$ after P2 can be written as

$$\boldsymbol{S}_{\text{out}} = \mathbf{M}_{\text{POL}}\mathbf{M}_R(\delta)\boldsymbol{S}_{\text{in}}, \tag{15}$$

where $\boldsymbol{S}_{\text{in}} = [1\ 1\ 0\ 0]^{\text{T}}$ represents the light that is linearly polarized by the polarizer P1. $\mathbf{M}_R(\delta)$ and $\mathbf{M}_{\text{POL}}$ are the Mueller matrices for the LCVR and the polarizer P2, respectively. $\mathbf{M}_R(\delta)$ and $\mathbf{M}_{\text{POL}}$ can be written as

$$\mathbf{M}_R(\delta) = \begin{pmatrix} 1 & 0 & 0 & 0 \\ 0 & \cos^2 2\phi + \sin^2 2\phi \cos\delta & \sin 2\phi \cos 2\phi (1 - \cos\delta) & -\sin 2\phi \sin\delta \\ 0 & \sin 2\phi \cos 2\phi (1 - \cos\delta) & \sin^2 2\phi + \cos^2 2\phi \cos\delta & \cos 2\phi \sin\delta \\ 0 & \sin 2\phi \sin\delta & -\cos 2\phi \sin\delta & \cos\delta \end{pmatrix}, \tag{16}$$

$$\mathbf{M}_{\mathrm{POL}}(\theta) = \frac{1}{2}\begin{pmatrix} 1 & \cos 2\theta & \sin 2\theta & 0 \\ \cos 2\theta & \cos^2 2\theta & \sin 2\theta \cos 2\theta & 0 \\ \sin 2\theta & \sin 2\theta \cos 2\theta & \sin^2 2\theta & 0 \\ 0 & 0 & 0 & 0 \end{pmatrix}, \tag{17}$$

where ϕ is the orientation of the fast axis with respect to P1, δ is the retardance of the LCVR due to the voltage applied, and θ is the orientation angle of P2 with respect to P1.

Substituting $\mathbf{M}_R$, $\mathbf{M}_{\mathrm{POL}}$ and $\boldsymbol{S}_{\mathrm{in}}$ in Equation (15), the output intensity (I_{out}) measured by the CCD is

$$I_{\mathrm{out}} = \frac{1}{2}\left[1 + \cos 2\theta\left(\cos^2 2\phi + \sin^2 2\phi \cos\delta\right) + \sin 2\theta \sin 2\phi \cos 2\phi (1 - \cos\delta)\right]. \tag{18}$$

In our setup, we always keep $\phi = 45°$. Hence, Equation (18) becomes

$$I_{\mathrm{out}} = \frac{1}{2}[1 + \cos 2\theta \cos\delta]. \tag{19}$$

For $\theta = 0°$, where P2 is parallel to P1, the output intensity is

$$I^0_{\mathrm{out}} = \frac{1}{2}[1 + \cos\delta]. \tag{20}$$

For $\theta = 90°$, where P2 crosses P1, the output intensity is

$$I^{90}_{\mathrm{out}} = \frac{1}{2}[1 - \cos\delta]. \tag{21}$$

Using Equations (20) and (21), the LCVR retardance can be obtained as

$$\delta = \cos^{-1}\left(\frac{I^0_{\mathrm{out}} - I^{90}_{\mathrm{out}}}{I^0_{\mathrm{out}} + I^{90}_{\mathrm{out}}}\right). \tag{22}$$

Thus, by measuring the intensities I_{out} for two different angles, $\theta = 90°$ and $\theta = 0°$, by rotating the polarizer P2, the retardance δ of the LCVR can be estimated for different voltages. However, this requires prior knowledge of the transmission axis of the polarizers and the fast axis of the LCVR. Hence, we determined the transmission axis of the polarizers and the fast axis of the LCVR using the same experimental setup before we carried out the characterization of the LCVR.

3.2. Determination of the Crossed Position of Polarizers

In order to precisely align the axis of the polarizers P1 and P2, the LCVR shown in Figure 3 was removed from the optical path. By keeping polarizer P1 at a fixed position, polarizer P2 was rotated from 0° to 180° with respect to P1 with a step size of 1° using a computer-controlled rotation stage. For each angle, the intensity was measured using the CCD. The plot between the angle and the measured intensity is shown in Figure 4. Initially, when P1 and P2 are in parallel position, the intensity is maximum. The intensity starts decreasing with the increase in the angle between them. At crossed position, we obtain the minimum intensity, which further starts increasing with the increase in the angle between P1 and P2. This satisfies the equation

$$\mathbf{M}_{\mathrm{P1}}\left(\theta = 0°\right).\mathbf{M}_{\mathrm{P2}}\left(\theta = 90°\right) = 0.$$

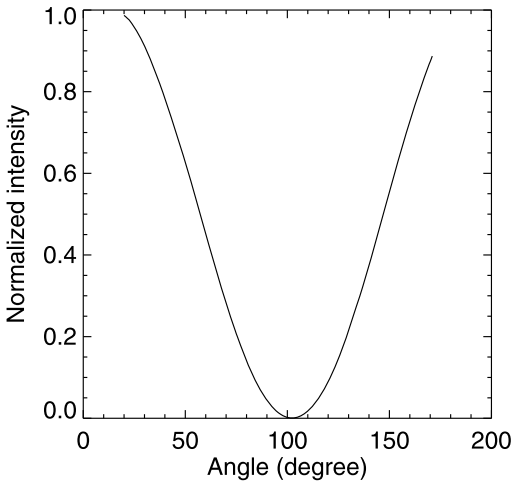

Figure 4 Intensity variation with rotation of polarizer P2 with respect to polarizer P1. The minimum intensity gives the angle at which the two polarizers cross each other.

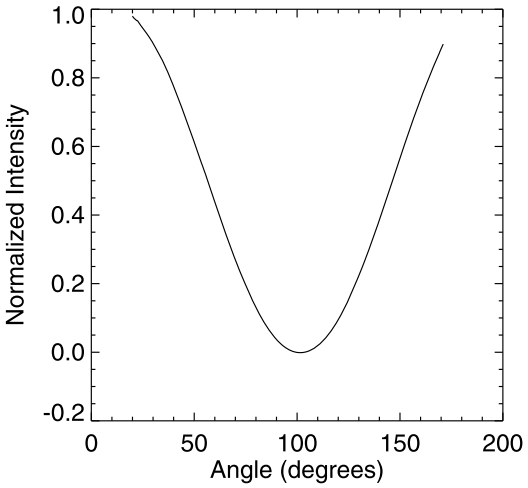

Figure 5 Intensity variation with rotation of the fast axis of the LCVR. The minimum intensity gives the position where the fast axis of the LCVR is parallel to the polarizer P1.

3.3. Determination of the Fast Axis of the LCVR

Knowing the position at which polarizers P1 and P2 cross, we proceed to determine the fast axis of the LCVR. For this purpose, polarizers P1 and P2 were kept in crossed position and the LCVR was again placed between them. After this, the output intensity was measured by rotating the LCVR. Figure 5 shows the plot between the measured intensity and the angle of the LCVR with respect to P1. The angle at which the minimum intensity is observed is the angle at which the fast axis of LCVR is parallel to P1. By knowing this angle, we rotated the fast axis of the LCVR to 45° with respect to P1 for further characterization of the LCVR. This procedure can be easily understood by solving the following Mueller matrix equation:

$$\mathbf{M}_{\mathrm{P1}}\left(\theta = 0^{\circ}\right).\mathbf{M}_{\mathrm{LCVR}}\left(\phi = 0^{\circ}, \delta\right).\mathbf{M}_{\mathrm{P2}}\left(\theta = 90^{\circ}\right) = 0.$$

3.4. LCVRs: Voltage Versus Retardance

After determining the position at which the polarizers are crossed as well as fast axis of LCVRs, we characterized the dependence of the voltage on the retardance of the LCVRs using the following procedure. Keeping the polarizers P1 and P2 in crossed position and the fast axis of LCVR at 45° with respect to P1, we applied voltages from 0 to 10 V in steps of 0.05 V to the LCVR. At each voltage, five images were taken, and we computed

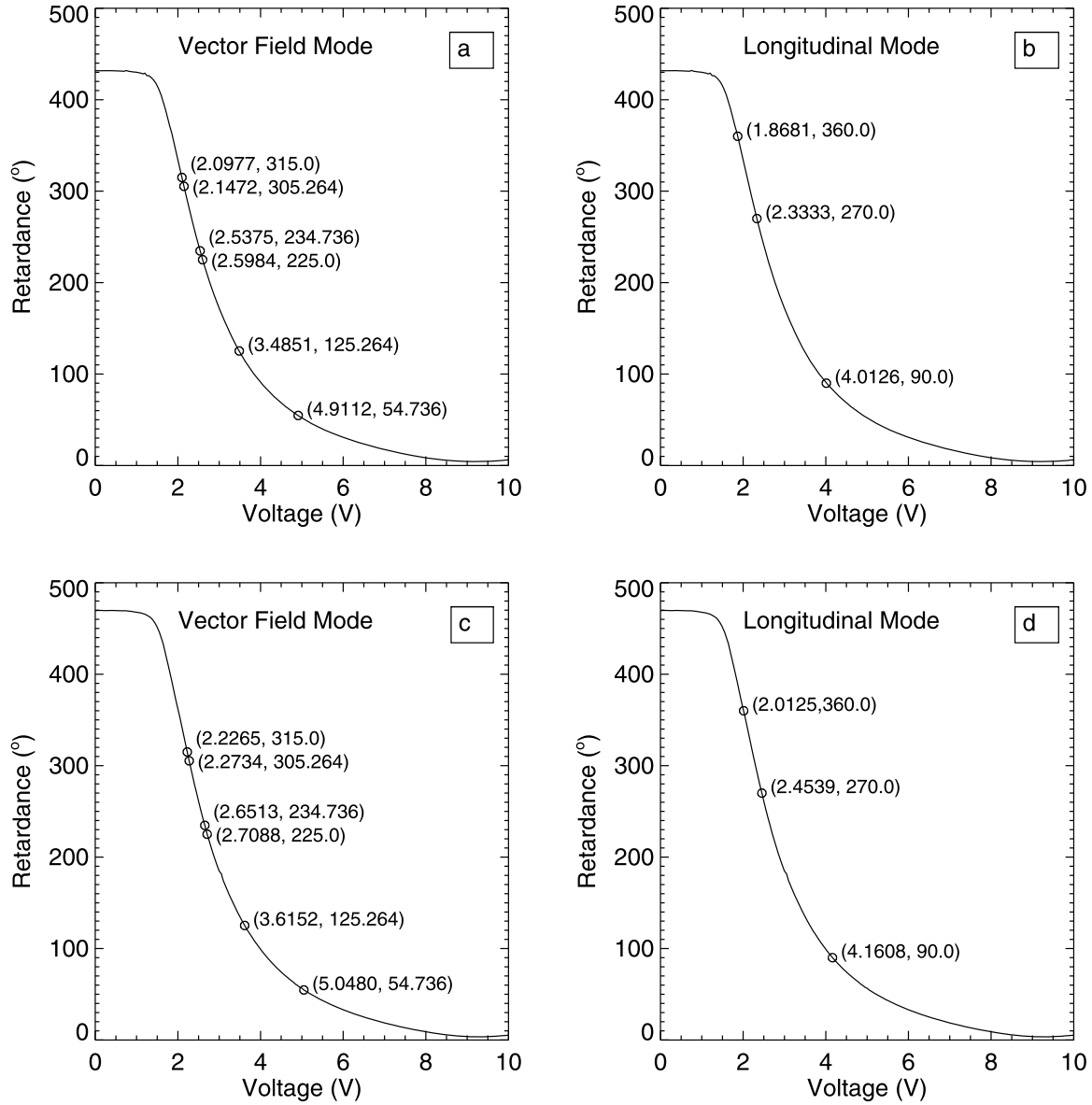

Figure 6 Calibration curves of LCVR1 (top panels) and LCVR2 (bottom panels) at 6173 Å showing retardance as a function of voltage. The left (a and c) and right (b and d) panels show the voltages for the required retardance in vector and longitudinal modes, respectively. Vector mode will be used for the measurement of all the Stokes parameters, and longitudinal mode will be used only for measuring the Stokes parameters I and V.

the mean intensity to obtain $I^{90}_{\rm out}$. Following the same procedure, $I^{0}_{\rm out}$ as a function of voltage was obtained by rotating P2 such that P1 and P2 are in parallel position. In both cases, the temperature of the LCVR was kept constant at 28°C.

With the measured $I^{0}_{\rm out}$ and $I^{90}_{\rm out}$ at each voltage, the retardance is calculated using Equation (22). The LCVR retardance (LCVR1 and LCVR2) with voltage for 6173 Å and 8542 Å is plotted and shown in Figure 6 and 7, respectively. The characteristics plots between retardance and voltage are used to estimate the voltages required in the two modulation schemes (vector and longitudinal). Figures 6 (a) and 6 (c) represent the corresponding voltages required for the retardance in vector-mode modulation scheme (shown by the circle on the characteristic curve), and Figures 6 (b) and 6 (d) represent the corresponding voltages required for the retardance in longitudinal-mode modulation scheme for LCVR1 and LCVR2 at 6173 Å.

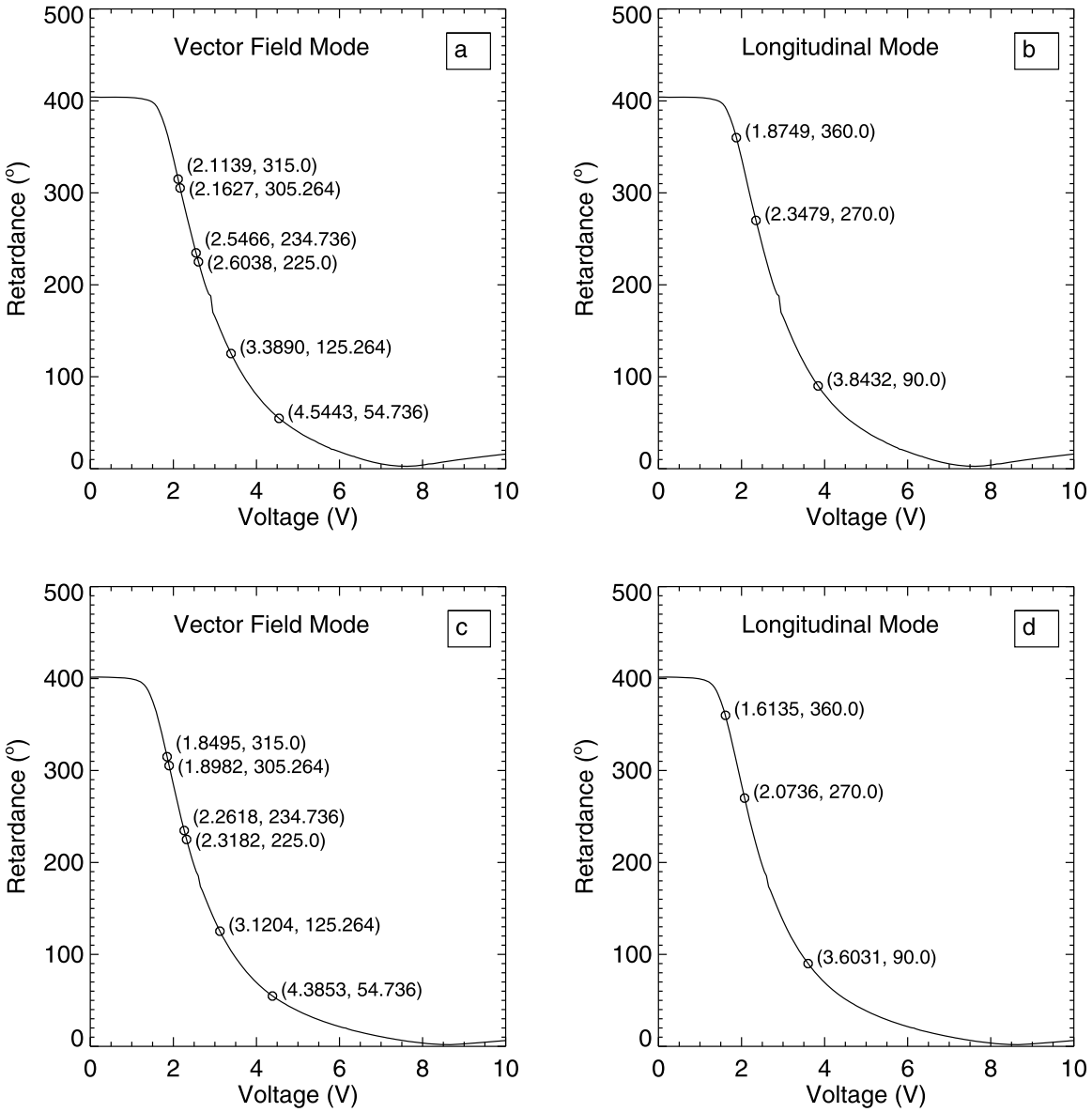

Figure 7 Calibration curves of LCVR1 (top panels) and LCVR2 (bottom panels) at 8542 Å showing retardance as a function of voltage. The left (a and c) and right (b and d) panels show the voltages for the required retardance in vector and longitudinal modes, respectively. Vector mode will be used for the measurement of all the Stokes parameters, and longitudinal mode will be used only for measuring the Stokes parameters I and V.

Table 4 Obtained voltages for the required retardance at 6173 Å in the vector field mode modulation scheme for the two LCVRs.

δ_1 (°)	Voltage of LCVR1 (V)	δ_2 (°)	Voltage of LCVR2 (V)
315.0	2.0977	305.264	2.2734
315.0	2.0977	054.736	5.0480
225.0	2.5984	125.264	3.6152
225.0	2.5984	234.736	2.6513

Similarly, panels (a) and (c) of Figure 7 represent the corresponding voltages required for the retardance in vector-mode modulation scheme, and panels (b) and (d) of Figure 7 repre-

Table 5 Obtained voltages for the required retardance at 6173 Å in the longitudinal mode modulation scheme for the two LCVRs.

δ_1 (°)	Voltage of LCVR1 (V)	δ_2 (°)	Voltage of LCVR2 (V)
360.0	1.8681	090.00	4.1608
360.0	1.8681	270.00	2.4539

Table 6 Obtained voltages for the required retardance at 8542 Å in the vector field mode modulation scheme for the two LCVRs.

δ_1 (°)	Voltage of LCVR1 (V)	δ_2 (°)	Voltage of LCVR2 (V)
315.0	2.1139	305.264	1.8982
315.0	2.1139	054.736	4.3853
225.0	2.6038	125.264	3.1203
225.0	2.6038	234.736	2.2618

Table 7 Obtained voltages for the required retardance at 8542 Å in the longitudinal-mode modulation scheme for the two LCVRs.

δ_1 (°)	Voltage of LCVR1 (V)	δ_2 (°)	Voltage of LCVR2 (V)
360.0	1.8749	090.00	3.6031
360.0	1.8749	270.00	2.0736

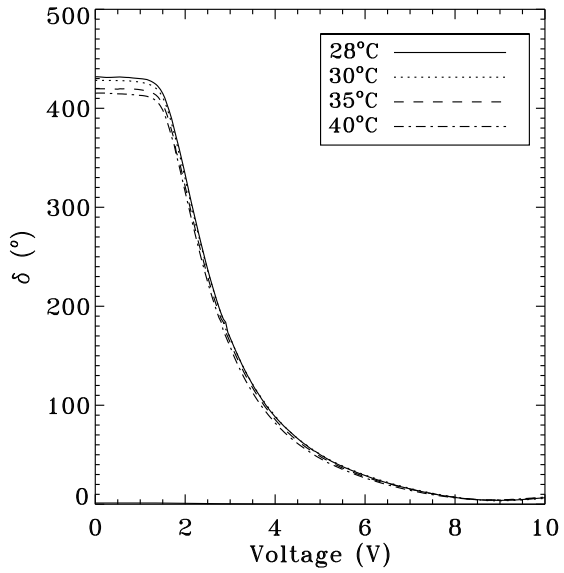

Figure 8 Retardance variation with the applied LCVR voltage for four different temperatures. It is evident that as temperature increases, the LCVR retardance decreases.

sent the corresponding voltages required for the retardance in longitudinal-mode modulation scheme for LCVR1 and LCVR2 at 8542 Å, respectively.

The retardance and their corresponding voltages calibrated for 6173 Å from Figure 6 are listed in Tables 4 and 5 while the corresponding voltages for 8542 Å from Figure 7 are listed in Tables 6 and 7. These values are used for the measurement of the Stokes parameters with the polarimeter for MAST.

Table 8 Polarimetric cross-talk due to change in the temperature stability (δT) of the thermal control system.

δT (°C)	$Q \rightarrow U$ cross-talk	$Q \rightarrow V$ cross-talk	$U \rightarrow V$ cross-talk
1.00	1.3×10^{-2}	1.3×10^{-2}	1.7×10^{-4}
0.50	6.5×10^{-3}	6.5×10^{-3}	4.25×10^{-5}
0.25	3.2×10^{-3}	$3,2 \times 10^{-3}$	1.04×10^{-5}

3.5. LCVRs: Temperature Versus Retardance

As it is evident from Equation (14) that the temperature also influences retardance of LCVRs, we have characterized the voltage dependence of an LCVR retardance at four different temperatures, *i.e.*, 28°C, 30°C, 35°C, and 40°C. Figure 8 shows a change in LCVR retardance with the voltage at different temperatures. As is evident from Figure 8, the LCVR retardance decreases as the temperature increases. The effect of temperature on the LCVR retardance can be clearly seen in Figure 9. It shows that the LCVR is more sensitive to the temperature when it is operated at low voltages (0 – 4 V) (Li, Gauzia, and Wu, 2004; Capobianco *et al.*, 2008). The greatest change in the retardance with a temperature of $\sim -1.5°/°\mathrm{C}$ is observed at 2.0 V. At present, the LCVRs are kept in a temperature enclosure provided by the vendor. The temperature stability of the enclosure is $\pm 1°\mathrm{C}$.

For precise polarimetric measurements, it is important to know the change in response matrix that is due to the fluctuations in the temperature enclosure. As mentioned above, a $\pm 1.0°\mathrm{C}$ variation in temperature causes a change in retardance of $-1.5°$ at most. Incorporating the change in retardance, the new response matrix can be written as

$$\mathbf{X}' = \begin{pmatrix} 0.99983 & 0.00017 & 0.01309 & -0.01309 \\ 0.00017 & 0.99983 & -0.01309 & 0.01309 \\ -0.01309 & 0.01309 & 0.99983 & 0.00017 \\ 0.01309 & -0.01309 & 0.00017 & 0.99983 \end{pmatrix}. \tag{23}$$

Thus, the error in the measurement of response matrix is

$$\Delta\mathbf{X} = \mathbf{X} - \mathbf{X}' = \begin{pmatrix} 0.00017 & -0.00017 & -0.01309 & 0.01309 \\ -0.00017 & 0.00017 & 0.01309 & -0.01309 \\ 0.01309 & -0.01309 & 0.00017 & -0.00017 \\ -0.01309 & 0.01309 & -0.00017 & 0.00017 \end{pmatrix},$$

where $\mathbf{X}$ is the unity matrix. The matrix elements $(3, 2)$, $(4, 2)$, and $(4, 3)$ of $\mathbf{X}'$ show the cross-talk among the Stokes parameters Q, U, and V. In this case, the cross-talk from Q to U and Q to V is the same and equal to 1.3×10^{-2}, and the U to V cross-talk is 1.7×10^{-4}. As the expected polarimetric accuracy is poorer, we calculated the change in polarimetric accuracy for different values of temperature accuracy. Table 8 summarizes the calculations. For a temperature variation of $\pm 0.25\,°\mathrm{C}$ (which can be obtained by optimizing the temperature control system), an error in retardance of $\pm 0.38°$ is caused (as shown in Table 8), and the cross-talk is on the order of 10^{-3}, which would be acceptable for our scientific studies. Therefore a temperature control system that can maintain an LCVR temperature within $\pm 0.25\,°\mathrm{C}$ will be constructed and used for the measurements of the Stokes parameters.

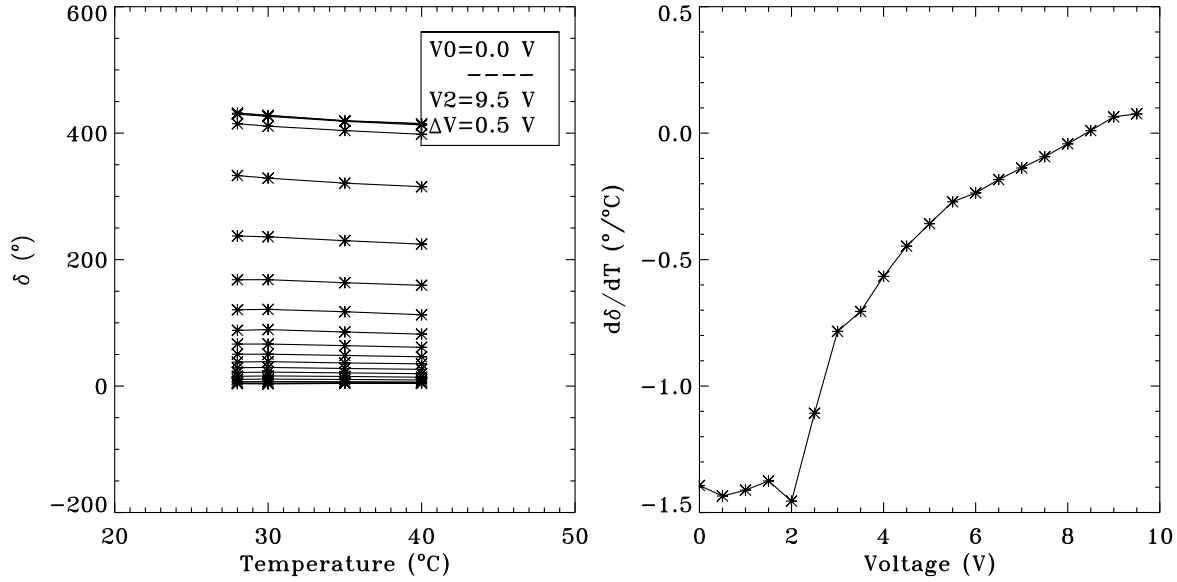

Figure 9 Left: change in retardance with the change in temperature for different voltages. Right: retardance derivative with respect to the temperature as a function of voltage, which shows that the LCVR is insensitive to temperature for higher voltages.

3.6. LCVRs: Change in the Orientation of the Fast Axis with the Voltage

It is presumed that the angular position of the LCVR fast axis is independent of the voltage; only the retardation changes according to the voltage. In practice, however, it is observed that the position of the fast axis also changes with the voltage (Terrier, Charbois, and Devlaminck, 2010). In order to see the effect of voltage on the orientation of the fast axis of the LCVR, we performed the following experiment. Two polarizers P1 and P2 were placed in a collimated beam keeping P1 at a reference position, and the intensity was measured by rotating P2 from 0 – 180°. After determining the position at which polarizers P1 and P2 cross, the LCVR was placed between P1 and P2. The orientation of the LCVR was adjusted such that the fast axis of the LCVR was parallel to polarizer P1 (Figure 10). In this configuration, rotating P2 gives exactly the same type of intensity variation as in the case of crossed linear polarizers. Without changing the orientation of the LCVR, we applied different voltages (between 0 – 10 V) to the LCVR and measured the intensity variation by rotating P2. We observed that (Figure 10, left) the intensity variation is again sinusoidal, and the sinusoid pattern for different voltages is shifted with respect to the reference sinusoid (no LCVR). The difference between the reference position (no LCVR or without voltage) and the actual position for different voltages was measured and plotted against the applied voltage for the LCVR (see Figure 10, right).

As shown in Figure 10 (right), the maximum shift obtained in the orientation of the fast axis of the LCVR is 8° at 2.5 V. This shows that it is important to know the change in the response matrix that is due to the shift in the orientation of the fast axis. The new response matrix caused by the change in the orientation of the fast axis (8°) is

$$\mathbf{X}' = \begin{pmatrix} 0.99454 & 0.03327 & 0.05467 & -0.08248 \\ 0.03327 & 0.99454 & 0.05467 & -0.08248 \\ 0.30782 & -0.20404 & 0.92874 & -0.03252 \\ 0.30782 & -0.20404 & -0.03252 & 0.92874 \end{pmatrix}. \tag{24}$$

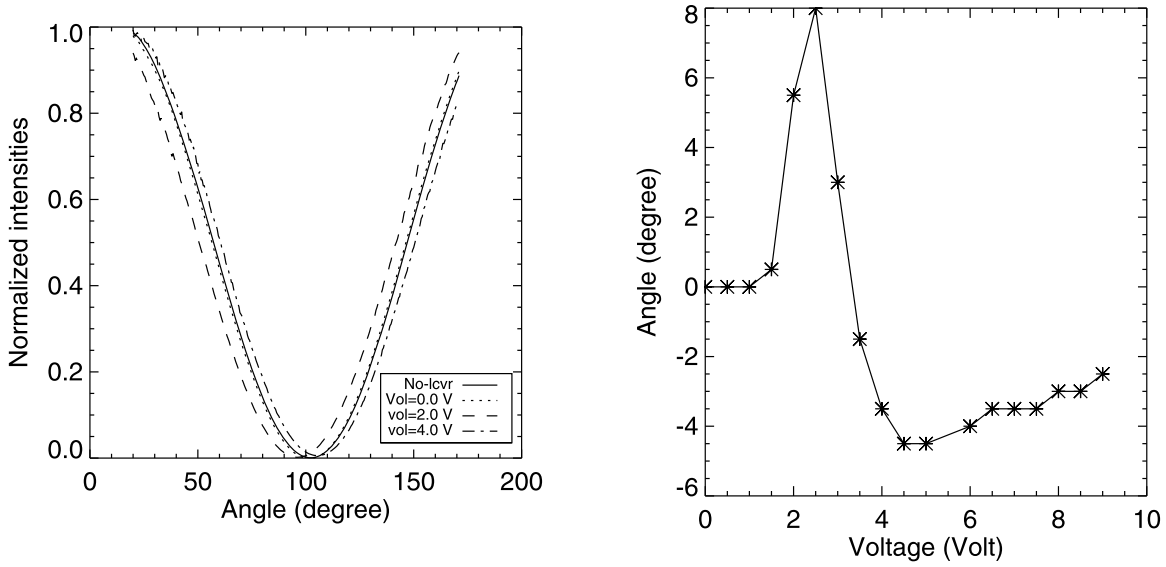

Figure 10 The left panel shows the intensity variation with the change in angular position of polarizer P2 with reference to polarizer P1 for different voltages applied to the LCVR. The right panel shows the shift in position of the fast axis with the voltage applied to the LCVR, in which reference is taken as the LCVR (without voltage) position.

The measurement error of the modulation matrix is

$$\Delta\mathbf{X} = \mathbf{X} - \mathbf{X}' = \begin{pmatrix} 0.00546 & -0.03327 & -0.05467 & 0.08248 \\ -0.03327 & 0.00546 & -0.05467 & 0.08248 \\ -0.30782 & 0.20404 & 0.07126 & 0.03252 \\ -0.30782 & 0.20404 & 0.03252 & 0.07126 \end{pmatrix},$$

where $\mathbf{X}$ is the unity matrix. The matrix elements $(3,2)$, $(4,2)$, and $(4,3)$ of $\mathbf{X}'$ show the cross-talk among the Stokes parameters Q, U, and V. In this case, the cross-talk from Q to U and Q to V is the same and equal to 2.0×10^{-1}, and the U to V cross-talk is 3.2×10^{-2}.

As is evident from this analysis, the cross-talk in the Stokes measurement resulting from the drift in the LCVR fast axis while applying voltages is considerably large and needs to be taken into account. The theoretical modulation matrix $\mathbf{O}$ (Equation 9) is modified by including the drift in the fast axis for corresponding voltages. This modified modulation matrix is used for the demodulation of the observed Stokes profiles (Terrier, Charbois, and Devlaminck, 2010).

4. Experimental Determination of the Polarimeter Response Matrix

As discussed in Section 2.1, the relation between the incoming Stokes vector and the measured Stokes vector can be written as

$$\boldsymbol{S}_{\text{meas}} = \mathbf{X}.\boldsymbol{S}_{\text{in}}, \tag{25}$$

where $\mathbf{X}$ is the 4×4 element response matrix. The response matrix of the polarimeter can be determined experimentally from the measured Stokes parameters of the known input polarizations that are generated by a calibration unit consisting of a zero-order quarter-wave plate (QWP) and a linear polarizer. We computed the response matrix of the polarimeter

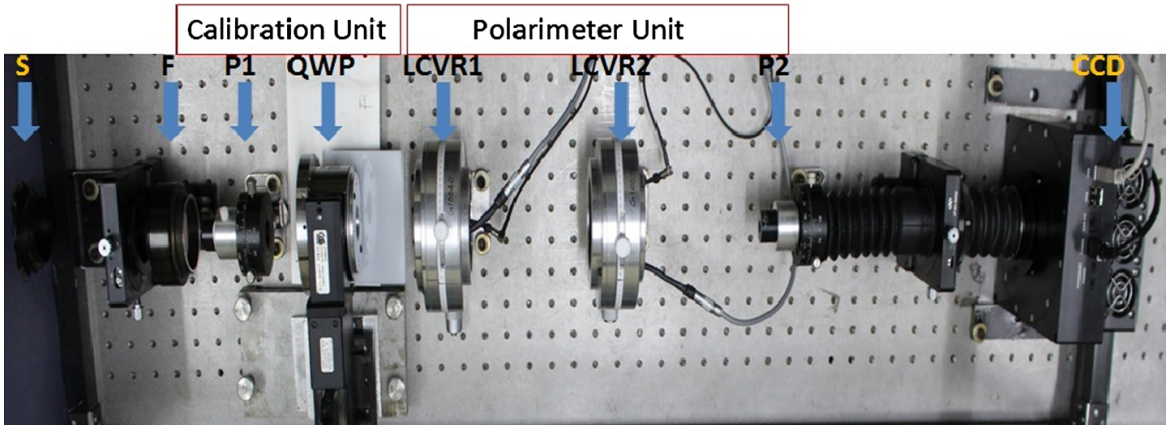

Figure 11 Experimental setup for the calibration of the response matrix for the MAST polarimeter. In this setup, a light beam is collimated using lens L1, and then collimating light passes through an interference filter (F). The calibration unit consists of a linear polarizer (P1) and a zero-order quarter-wave plate (QWP), and the polarimeter consists of two LCVRs (LCVR1 and LCVR2) and a linear polarizer (P2). Finally, an image is formed by the imaging lens on the CCD, which is placed in the focal plane of the imaging lens.

in the laboratory using the experimental setup shown in Figure 11 for the two wavelengths (6173 Å and 8542 Å).

To calibrate the response matrix, the calibration unit (CU) was placed in the beam before the polarimeter module, as shown in Figure 8. The orientation of the axes was determined with an accuracy of $\pm 1^\circ$ for the linear polarizer, and $\pm 0.5^\circ$ for the QWP of the CU, which was fixed on a computer-controlled rotating mount. To determine $\mathbf{X}$ of the polarimeter, 80 known polarization states were created by rotating QWP from $0-160^\circ$ with a step size of 2° and measured by the polarimeter using the four-intensity-measurement modulation scheme (Table 1) and the six-measurement modulation scheme (Table 2), as discussed in Section 2.1. We computed the response matrix of the polarimeter using both schemes. Here, we discuss in detail the response matrix calibration using the four-measurement modulation scheme. For the configuration shown in Figure 11, the input Stokes vector can be written as

$$\boldsymbol{S}_{\text{in}} = \mathbf{M}_{\text{QWP}}(\theta_r, \delta).\mathbf{M}_{\text{P1}}(\theta_p).[1 \quad 0 \quad 0 \quad 0]^{\text{T}},$$

where θ_r and θ_p are the orientation of the retarder and polarizer of the CU relative to the reference axis, and δ is the QWP retardance. In our case, we fixed θ_p at 0°. The input Stokes parameters for different retarder orientation are then given by

$$\left.\begin{aligned} I &= 1, \\ Q &= \cos^2(2\theta) + \sin^2(2\theta).\cos(\delta), \\ U &= \sin(2\theta).\cos(2\theta).\big(1 - \cos(\delta)\big), \\ V &= -\sin(2\theta).\sin(\delta). \end{aligned}\right\} \tag{26}$$

For n orientations of the CU retarder, the polarimeter response matrix is calibrated from the measurements after rearranging the Stokes vector into $n \times 4$ matrices by a solution of the linear problem,

$$\boldsymbol{S}_{\text{meas}} = \mathbf{X}.\boldsymbol{S}_{\text{in}}.$$

Multiplying by $\boldsymbol{S}_{\text{in}}^{\text{T}}$ from the right in this equation,

$$\boldsymbol{S}_{\text{meas}}.\boldsymbol{S}_{\text{in}}^{\text{T}} = X.\boldsymbol{S}_{\text{in}}.\boldsymbol{S}_{\text{in}}^{\text{T}} = \mathbf{X}.\mathbf{D},$$

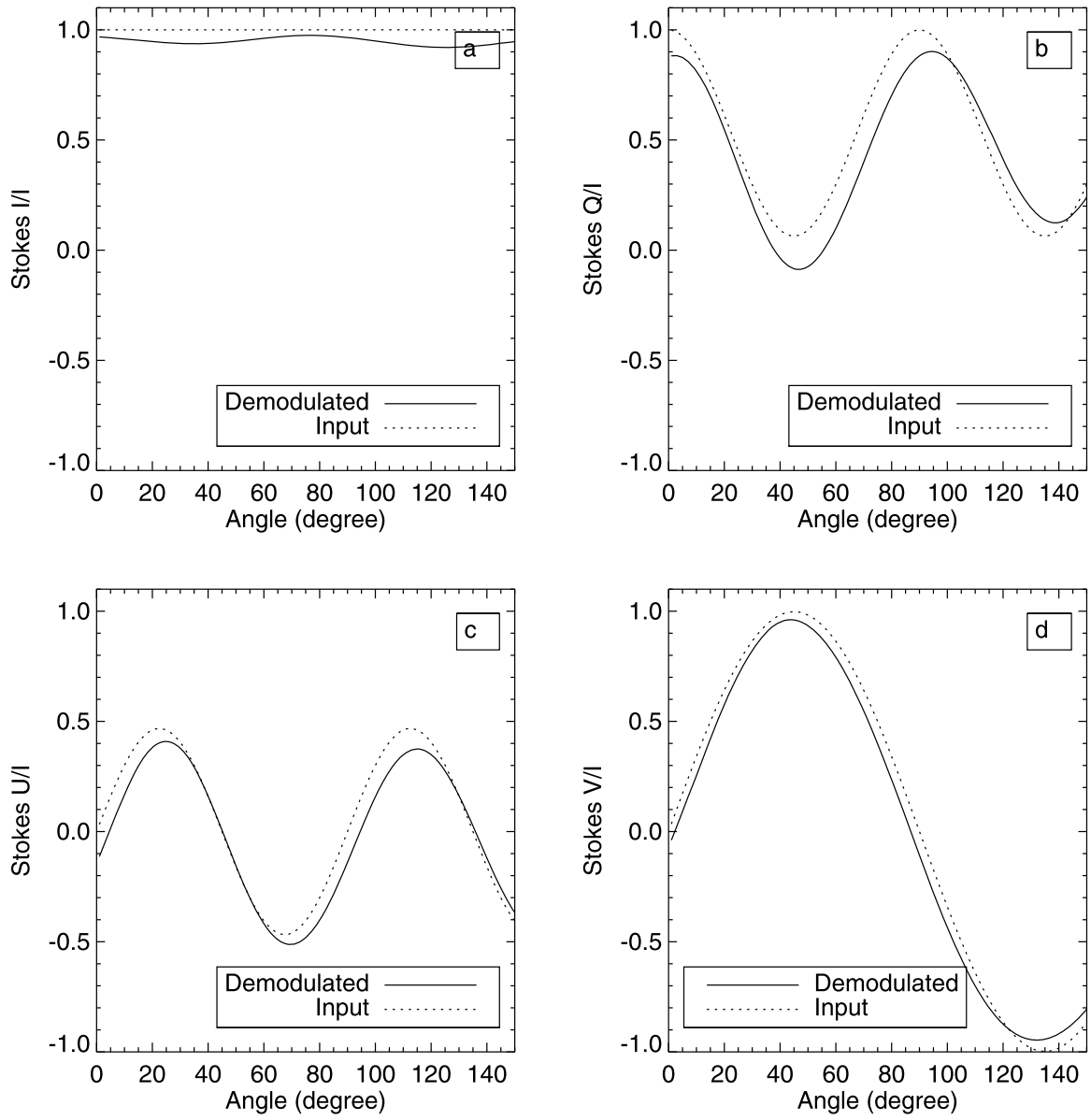

Figure 12 Plots of input Stokes parameters and demodulated Stokes parameters calculated at each position angle of the QWP of the CU for 6173 Å.

where

$$\mathbf{D} = \boldsymbol{S}_{\rm in}.\boldsymbol{S}_{\rm in}^{\rm T}.$$

Therefore, the final expression for response matrix is

$$\mathbf{X} = \boldsymbol{S}_{\rm meas}.\boldsymbol{S}_{\rm in}^{\rm T}.\mathbf{D}^{-1}. \tag{27}$$

Hence, the response matrix for 6173 Å is determined from the above equation using the input, and the measured Stokes vector is given by

$$\mathbf{X}_4^{6173} = \begin{pmatrix} 1.0000 & -0.0507 & -0.0054 & -0.0595 \\ -0.0090 & 0.8946 & -0.1618 & -0.0369 \\ -0.0447 & -0.0639 & 0.8314 & 0.0734 \\ -0.0474 & -0.1494 & 0.0647 & 0.9665 \end{pmatrix}. \tag{28}$$

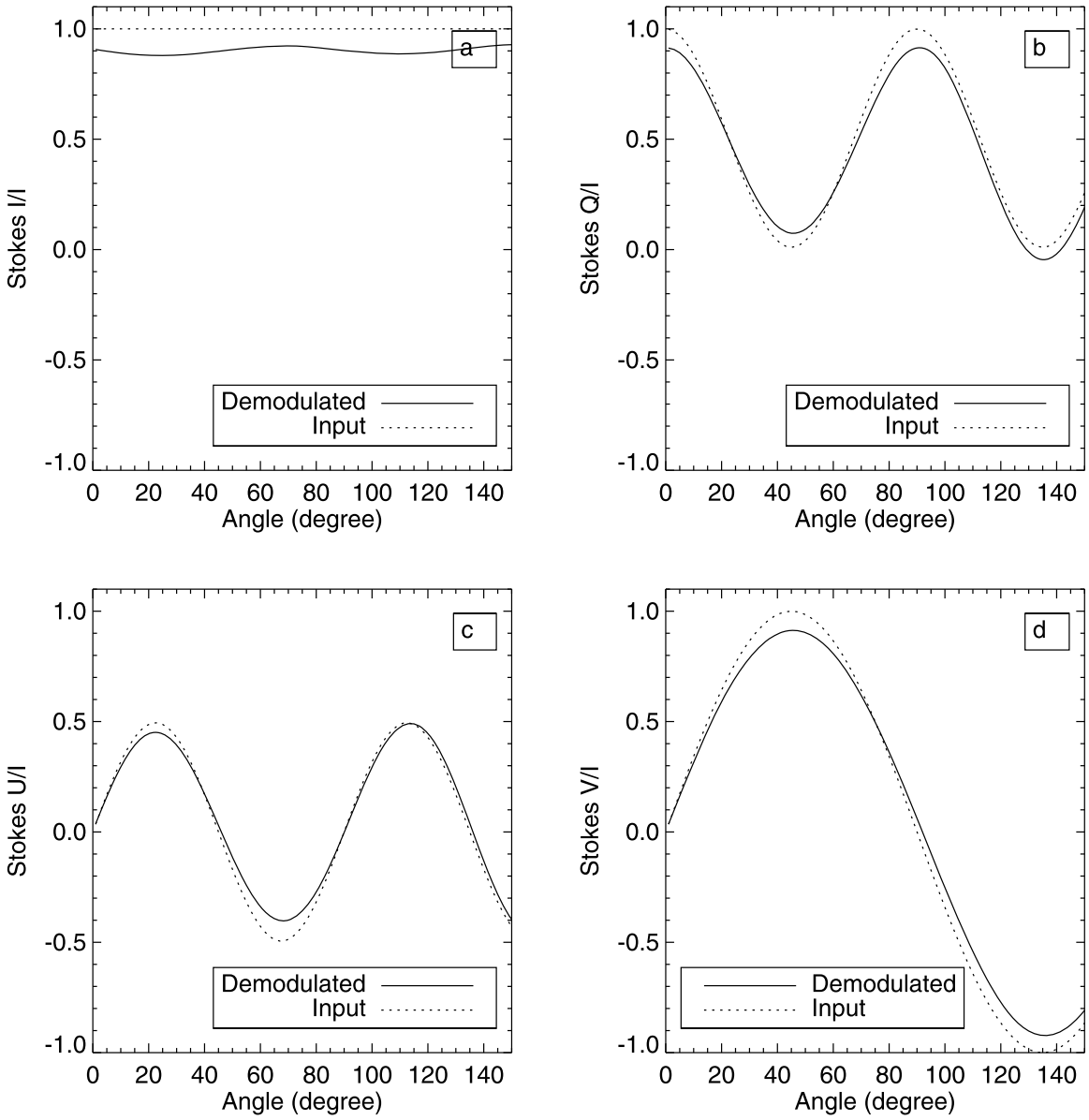

Figure 13 Plots of input Stokes parameters and demodulated Stokes parameters calculated at each position angle of the QWP of the CU for 8542 Å.

Thus, the real incoming Stokes vector $\boldsymbol{S}_{\rm in}$ can be calculated from the observed Stokes vector and the measured response matrix as

$$\boldsymbol{S}_{\rm in} = \mathbf{X}^{-1}.\boldsymbol{S}_{\rm meas}.$$

The input and the demodulated Stokes parameters at each CU retarder orientation are shown in Figure 12.

Similarly, we determined the response matrix of the polarimeter at 8542 Å, given by

$$\mathbf{X}_4^{8542} = \begin{pmatrix} 1.0000 & 0.0006 & 0.0349 & -0.0965 \\ -0.0009 & 0.8931 & -0.1053 & 0.0041 \\ -0.0135 & -0.0616 & 0.9073 & -0.1809 \\ 0.0873 & 0.0452 & 0.1948 & 0.9115 \end{pmatrix}, \tag{29}$$

and plots for the input and demodulated input Stokes parameters are shown in Figure 13.

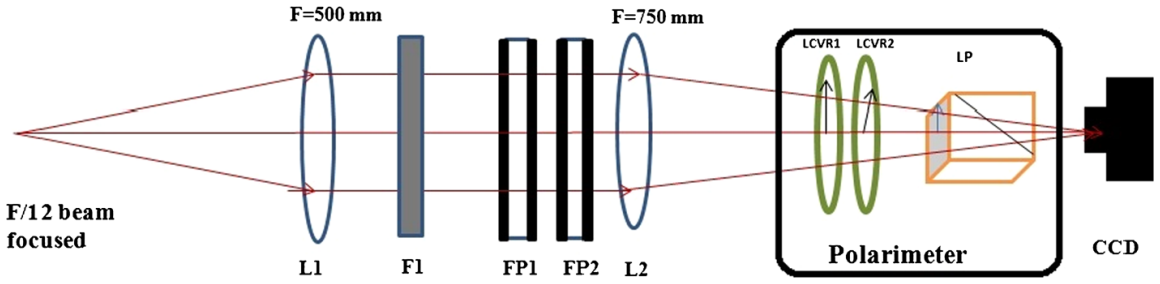

Figure 14 Schematic diagram of the imaging polarimeter for MAST. In this setup, an F/12 beam from the telescope is collimated using lens L1. The collimating beam passes through the narrow-band imager and consists of two Fabry–Perot etalons (FP1 and FP2) and the prefilter F1. The polarimeter consist of two LCVRs, and a Glan–Thompson polarizer is kept in between the CCD and the imaging lens (L2) in the converging beam. The F-number of the converging beam is 18.

4.1. Response Matrix for the Six-Measurement Modulation Scheme

Similarly, we also computed **X** when the Stokes parameters were obtained by the six-measurement modulation scheme and the other procedures were the same as discussed above. The response matrix of the polarimeter for 6173 Å is

$$\mathbf{X}_6^{6173} = \begin{pmatrix} 1.0000 & -0.0084 & 0.0153 & -0.0016 \\ 0.0009 & 0.9493 & 0.0265 & 0.1462 \\ -0.0171 & 0.0254 & 0.9573 & 0.9491 \\ 0.0043 & -0.1829 & -0.0808 & 0.9491 \end{pmatrix}. \tag{30}$$

Similarly, the response matrix of the polarimeter for 8542 Å is

$$\mathbf{X}_6^{8542} = \begin{pmatrix} 1.0000 & 0.0062 & -0.0177 & 0.0044 \\ -0.0056 & 0.9251 & 0.0665 & 0.1308 \\ -0.0652 & 0.0396 & 0.9454 & 0.0791 \\ 0.0344 & -0.1379 & -0.1509 & 0.9176 \end{pmatrix}. \tag{31}$$

5. Preliminary Observations of Stokes Profiles

Preliminary observations were obtained using the imaging spectropolarimeter for MAST, consisting of a narrow-band imager and a polarimeter. The narrow-band imager is designed around two z-cut $LiNbO_3$ Fabry–Perot etalons placed in tandem to provide a better spectral resolution. The wavelength characterization of the components of the narrow-band imager is described in a previous article (Raja Bayanna *et al.*, 2014). The integration and test results of the imager obtained with MAST will be presented in a separate article (Mathew *et al.*, 2017). The full-width at half maximum (FWHM) of the FP combination is $\sim$95 mÅ at 6173 Å with an effective free-spectral range (FSR) of 6 Å. A blocking filter of 2.5 Å is introduced to restrict the FP channel of the desired wavelength. For the Ca II 8542 Å line we used only one etalon, with 175 mÅ FWHM. As explained earlier, the polarimeter consists of two LCVRs and a linear polarizer (Glan–Thompson polarizer).

The optical setup of the spectropolarimeter is shown in Figure 14. The F-12 beam from the telescope and its re-imaging optics was collimated using a lens (L1) of focal length 500 mm. The FPs were placed in this collimated beam in order to reduce the wavelength shift produced by the finite incidence angle arising from the FOV. The collimated output through

the FPs was imaged using a lens (L2) of focal length 750 mm, which forms a plate scale of $0.145''$ pixel^{-1} at the CCD plane. The polarimeter was placed in this converging beam after the lens L2, to accommodate the smaller Glan–Thompson polarizer. The acceptance angles of the LCVRs are large enough to work with the resultant F-18 beam. Since the z-cut etalons with a small incidence angle produce negligible polarization effects, we did not separately consider the effect of the etalons in the polarization measurements. The fast axes of the first and second LCVRs were kept at 0° and 45° with respect to the polarization axis of the linear polarizer, as described in Section 2. The temperatures of the LCVRs were kept at 28 °C.

For the present set of observations, we first modulated the polarization and then the wavelength to minimize the influence of seeing. The response time of the LCVRs (for the change of one polarization state to next) is 22 ms. A change in wavelength position requires 100 ms and 200 ms for a spectral sampling of 15 mÅ and 30 mÅ, respectively, as the tuning speed of the FPs is nearly 1000 V s^{-1}.

We captured 20 images for each polarization state to build up the signal. The overall time taken for one modulation cycle (*i.e.* for obtaining IQUV at one wavelength position) is around 8 seconds considering an exposure time of 60 ms (at 6173 Å). Depending on the number of wavelength positions, the time cadence of the vector magnetogram varies; for example, the cadence varies from 40 seconds to 216 seconds for 5 to 27 wavelength positions, respectively. The number of wavelength points that determine the time cadence can be selected as required by the scientific objectives. A cadence of more than a minute is sufficient to study the evolution of active regions and the energy build-up due to the foot-point motions (Wiegelmann and Sakurai, 2012, and references therein). Magnetograms (by tuning the filter to a single wavelength position) can be obtained in a 10-second cadence, which could be used for studying the magnetic field evolution of small-scale moving magnetic features seen around the sunspot (Ma *et al.*, 2015, and references therein). A six-wavelength step scan, which takes around 50 seconds, can reproduce the line profile as seen in SDO/HMI, which is suitable to retrieve the vector magnetic field, as long as the horizontal speed of the moving feature is below 3 km s^{-1}.

For the initial tests, we scanned the spectral profile of the 6173 Å line with a step of 15 mÅ and 30 mÅ for a total of 27 and 20 positions, respectively, in longitudinal and vector modes. The number of wavelength positions could be considerably reduced by an optimization after inverting the profiles, which will be carried out after further analysis. We obtained observations in longitudinal and vector modes as described in Section 2.1.

5.1. Longitudinal Mode

The observations described in this section were obtained for a sunspot in Active Region NOAA AR 12436 taken on 24 October 2015 between 4:00 UT and 5:30 UT, when the seeing was moderate. The active region (AR) was located slightly away from the disk center at N09 and W20. FP etalons of the narrow-band imager were sequentially tuned to 27 positions on the 6173 Å line, with 15 mÅ wavelength spacing. A pair of two images in left- and right-circular polarizations (LCP and RCP) was obtained by applying appropriate voltages (listed in Table 5) to LCVR 1 and 2. For these measurements, the voltage of LCVR1 is changed alternately, while LCVR2 is kept constant to provide a retardance of 1λ. For each wavelength position, 20 pairs of LCP and RCP images were obtained with an exposure time of 65 ms to increase the S/N. Figure 16 shows the results of the above observation. The top left panel shows one of the mean intensity images, and the right panel shows the corresponding mean Stokes I profiles. The mean Stokes I profile is deduced separately for the magnetic (solid line, where the V signal is higher than 10^{-3}) and for the non-magnetic (dashed line) regions.

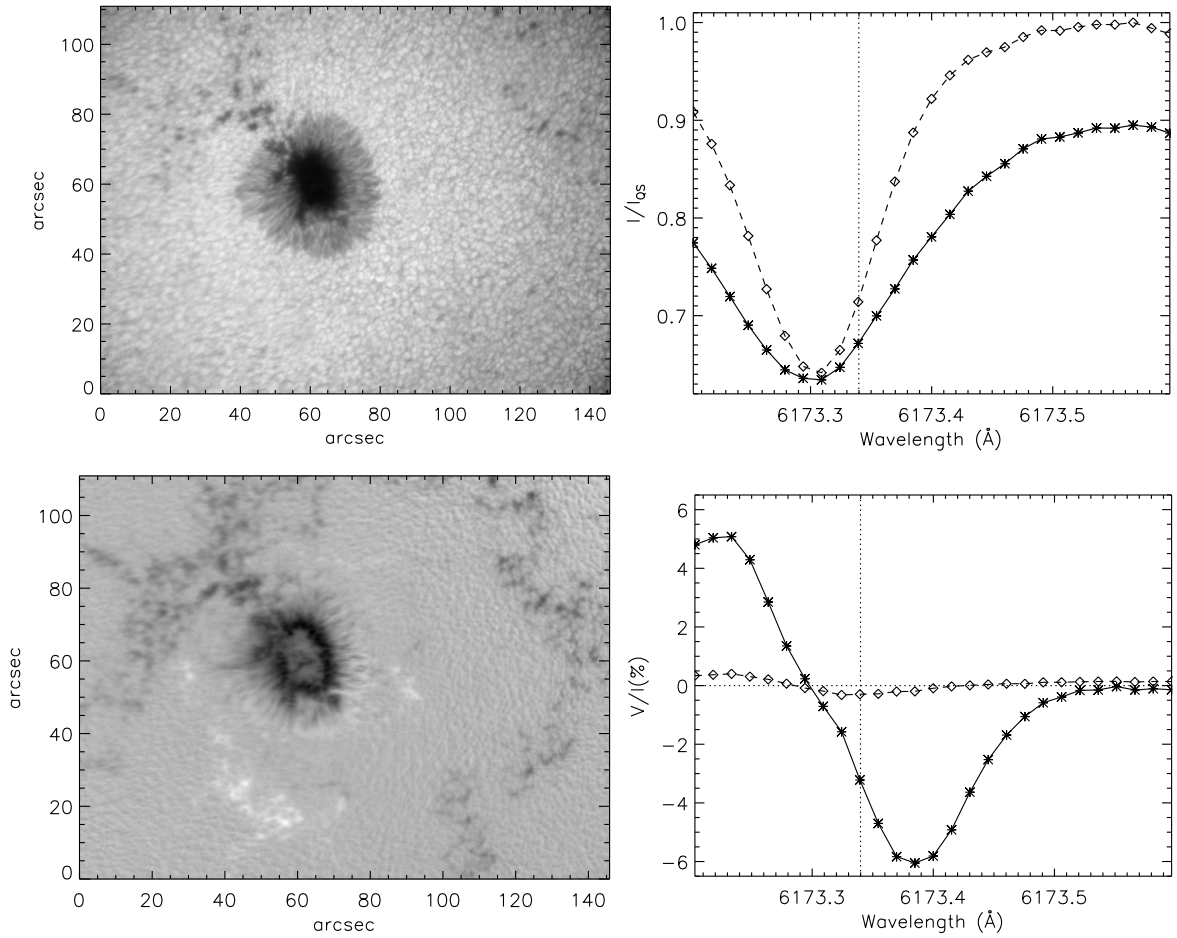

Figure 15 LOS mode of observations of NOAA AR 12436 observed on 24 October 2015 between 4:00 UT and 5:30 UT using the MAST polarimeter. In the first row, the left panel shows one of the mean intensity images, while the right panel shows the corresponding mean Stokes I profiles. The Stokes I profile is deduced separately for the magnetic (solid line) and for the non-magnetic (dashed lines) regions, while in the second row, the left panel displays the mean Stokes V image for a wavelength position at +75 mÅ from line center and the right plot indicates the mean Stokes V profile for both the magnetic and non-magnetic regions. Because the voltage tuning of the two etalons in tandem is limited, the line profile is shifted more toward the blue side.

The broadening of the profile caused by the magnetic field is evident in these plots. The bottom left panel displays the mean Stokes V image for a wavelength position at +75 mÅ from line center, and the right plot indicates the mean Stokes V profile for the magnetic and non-magnetic regions.

5.2. Comparison of Stokes V Images from SDO/HMI and USO/MAST

We also carried out a comparison of our results with the magnetograms obtained from the *Helioseismic Magnetic Imager* (HMI) instrument (Scherrer *et al.*, 2012; Schou *et al.*, 2012) onboard the *Solar Dynamics Observatory* (SDO) (Pesnell, Thompson, and Chamberlin, 2012). For comparison, the images from MAST and HMI were taken at around the same time (04:42 UT on 24 October 2015). The comparison was possible as the spectral line used by the two instruments is the same, even though the spectral resolution of each instrument differs. SDO/HMI provides both LOS and vector magnetograms. It also provides LCP and RCP with a 45-second cadence and Stokes I, Q, U, V images with a 12-minute cadence. For our present comparison, we constrained only SDO/HMI LOS magnetograms and Stokes V

images, since our polarization measurements need further instrumental polarization corrections. Even though the stokes V profiles might also be contaminated by the instrumental polarization, as the cross-talk from the linear polarization mostly introduce only a bias in Stokes V images, the present comparison is not expected to be affected.

The magnetogram obtained from the SDO/HMI was resized, and the USO/MAST image was registered with respect to the SDO/HMI map. The right and left images in the top panel of Figure 16 show the cropped continuum images taken with the SDO/HMI and USO/MAST instruments, respectively. The images are cropped in such a way that they include the sunspot and a part of the nearby area. The middle panel shows the Stokes V images of SDO/HMI (left) and the USO/MAST polarimeter (right) for a selected wavelength position $+75$ mÅ (from the line center). It is evident from these panels that most of the magnetic features in the Stokes V map of SDO/HMI match the Stokes V map of the USO/MAST polarimeter well. The advantage of the space-based observation is clearly visible in the SDO/HMI images, as is evident from the low-background features.

Unlike SDO/HMI observations, the USO/MAST images are affected by the atmospheric seeing during the image acquisition, which results in considerable $I \rightarrow V$ cross-talk (Del Toro Iniesta, 2003; Lites, 1987) and in turn a higher background noise. This $I \rightarrow V$ cross-talk is evident from the granulation pattern in the Stokes V images of USO/MAST.

The bottom panels show the Stokes V signal obtained at a wavelength position $+75$ mÅ (from the line center) plotted against the SDO/HMI LOS magnetic field strength. The plot in the left panel shows the USO/MAST Stokes V, and the right panel shows the SDO/HMI Stokes V at a close-by wavelength position against the SDO/HMI LOS magnetic field strength. The region shown in red contains points mostly from the umbra, where the linearity between the Stokes V amplitude and the magnetic field strength does not hold. Figure 16 clearly shows that except for the scatter, which might be partly due to the seeing-related $I \rightarrow V$ cross-talk, the trend matches closely.

We also found a factor of around two in the Stokes V signal between the SDO/HMI and the USO/MAST images. This can be explained by the influence of the finite width of the narrow-band filter in scanning the line profile and the difference in the overall instrumental profiles used in the HMI and MAST imagers. The finite width of the filter causes a convolution of the spectral line profile, which introduces an apparent increase in the width and a decrease in the depth of the line profile. This effectively reduces the amplitude of the Stokes V signal. In order to check this, we computed synthetic line profiles using the M – E inversion code for realistic solar atmospheric parameters. The convolution of the Stokes V parameter with the filter profile of 95 mÅ FWHM shows a reduction in the peak of Stokes V amplitude by a similar factor, *i.e.*, 2. This effect can be taken into account while inverting the Stokes profiles; *i.e.*, convolution of the synthetic profile with the filter profile is carried out before fitting the profile with observed Stokes profiles. Except for these differences, the overall comparison between the SDO/HMI and the USO/MAST Stokes V measurements provides confidence in our measurements.

5.3. Vector Mode

By operating the imaging polarimeter in vector mode, we carried out observations on 19 December 2015. NOAA AR12470 (N15, W07) was observed during the period 06:00 UT and 07:30 UT. Four images were obtained sequentially by applying appropriate voltages (listed in Table 4) to the LCVRs. From the observed intensity images, Stokes, I, Q, U and V images were computed for each wavelength position. Similar to the longitudinal mode, the images in vector mode were acquired by scanning the line profile with 15 mÅ spacing

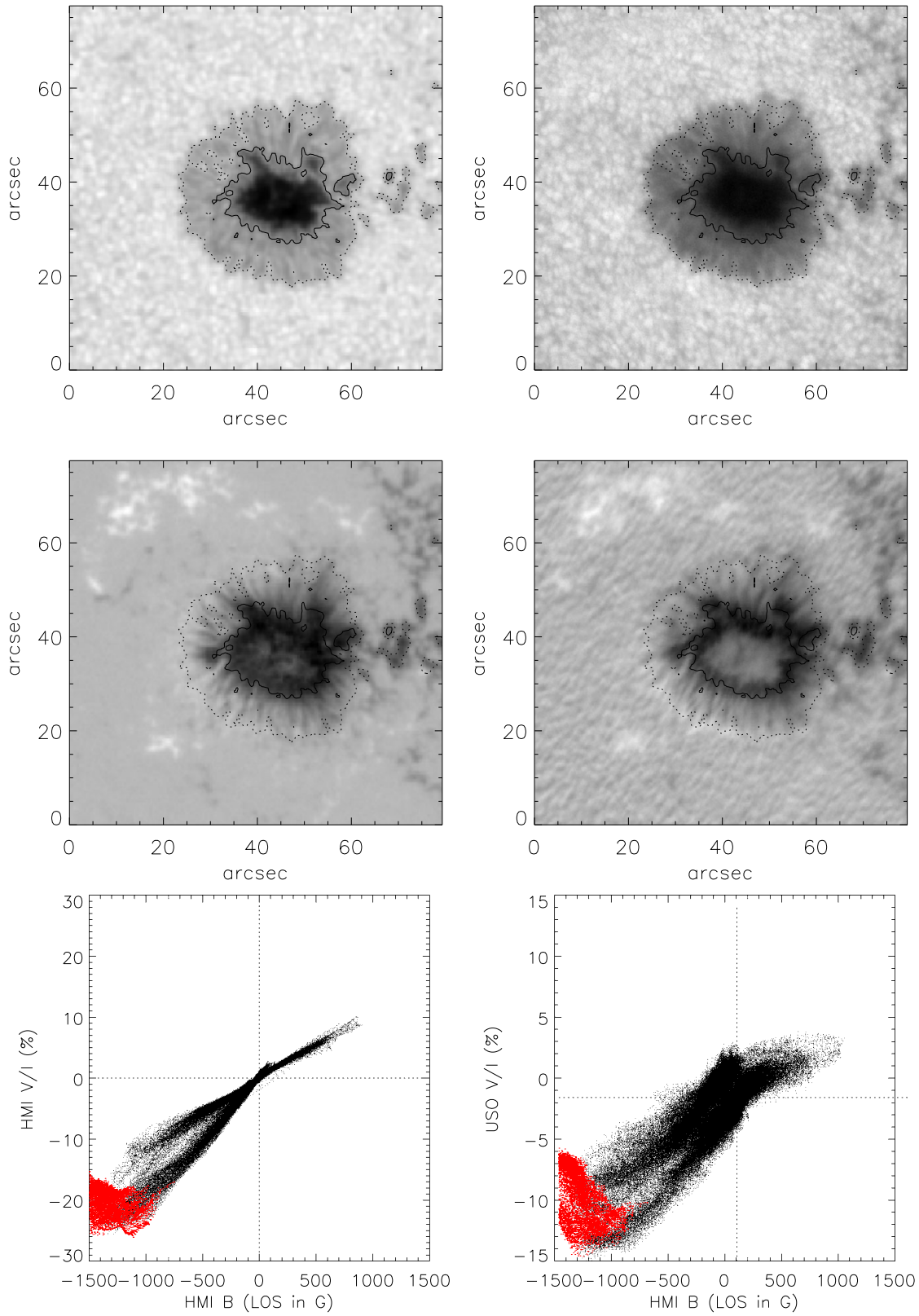

Figure 16 Top row: Stokes I image taken by SDO/HMI (left) and USO/MAST (right); Middle row: Stokes V image at wavelength position +75 mÅ from line center taken by SDO/HMI (left) and USO/MAST (right); bottom row: scatter plot made between Stokes V of SDO/HMI and longitudinal magnetic field of SDO/HMI (left) and scatter plot made between Stokes V of USO/MAST and longitudinal magnetic field of SDO/HMI (right).

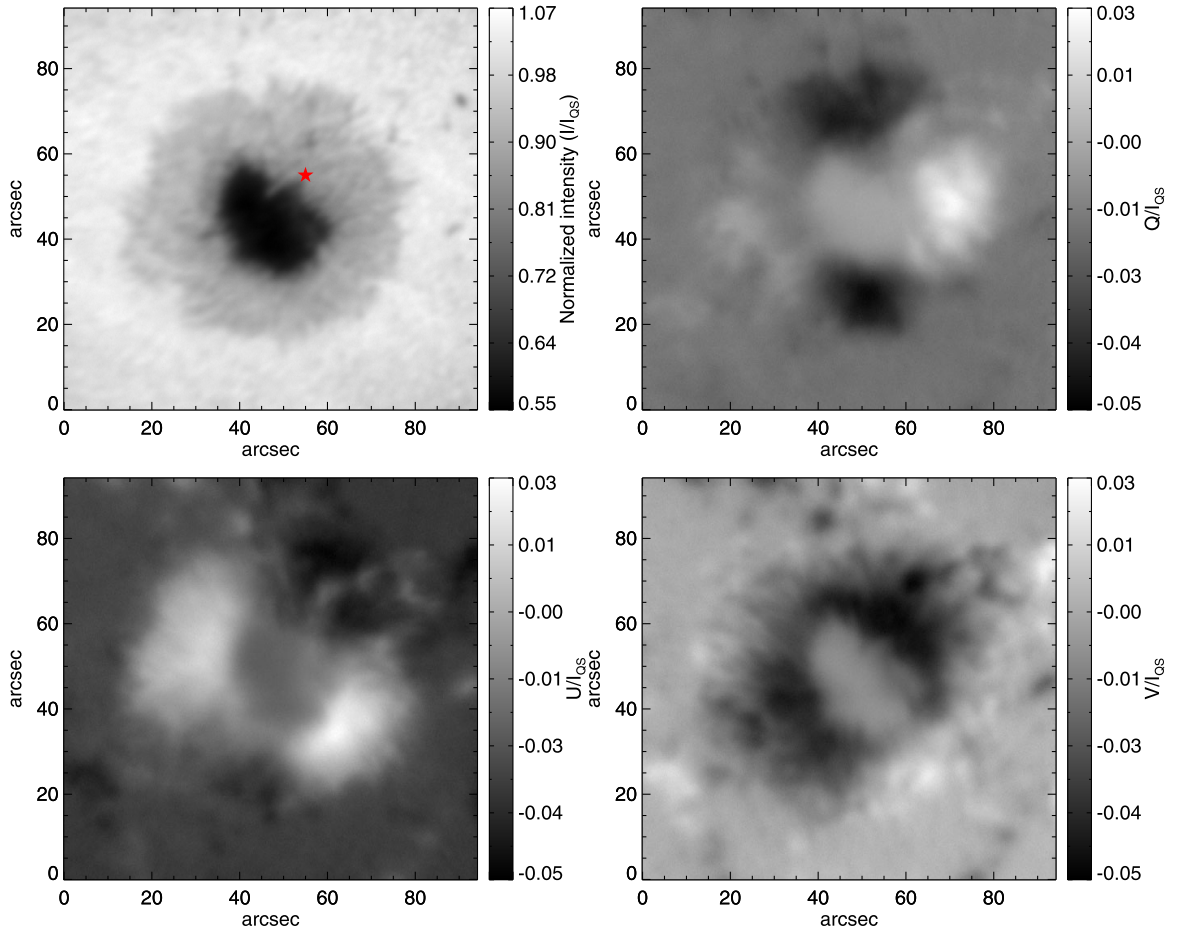

Figure 17 Stokes images obtained using vector mode of operation for NOAA AR 12470 at 6173 Å. The top panels show Stokes I (left) and Q (right) images. The bottom panels show Stokes U (left) and V (right) images.

and at 27 wavelength positions. Figure 17 shows the images at 6173 Å. The top left and right panels shows the Stokes I and Q images, the bottom left and right panels show the U and V images. The Stokes U, Q, and V images are shown for a wavelength position at $+75$ mÅ from line center on the line profile.

Figure 18 shows the respective Stokes profiles for the single point marked by a star in Stokes I image from Figure 17. A thorough analysis and demodulation of the linear polarization measurement requires knowing the instrumental polarization. For this purpose, we are currently introducing a large (50 cm) sheet linear polarizer that can be rotated in front of the primary mirror. This will enable us to characterize the telescope polarization before extracting the Stokes information from these measurements.

5.4. Observations on 16 April 2016

As evident in the Stokes I profile in the top panel of Figure 15, the starting point for the wavelength scanning has a limited coverage in the blue wing side of the Fe I 6173 Å line profile. This was due to the limited tuning range of the Fabry–Perot filters, which was restricted by the maximum voltage that could be applied to the etalons and by the operating temperatures of the etalons. As it is important to cover the entire wavelength range in order to obtain the continuum intensity at both sides of the line profile, we retuned the etalons to optimally cover the continuum at both sides. Since the maximum allowed voltage that

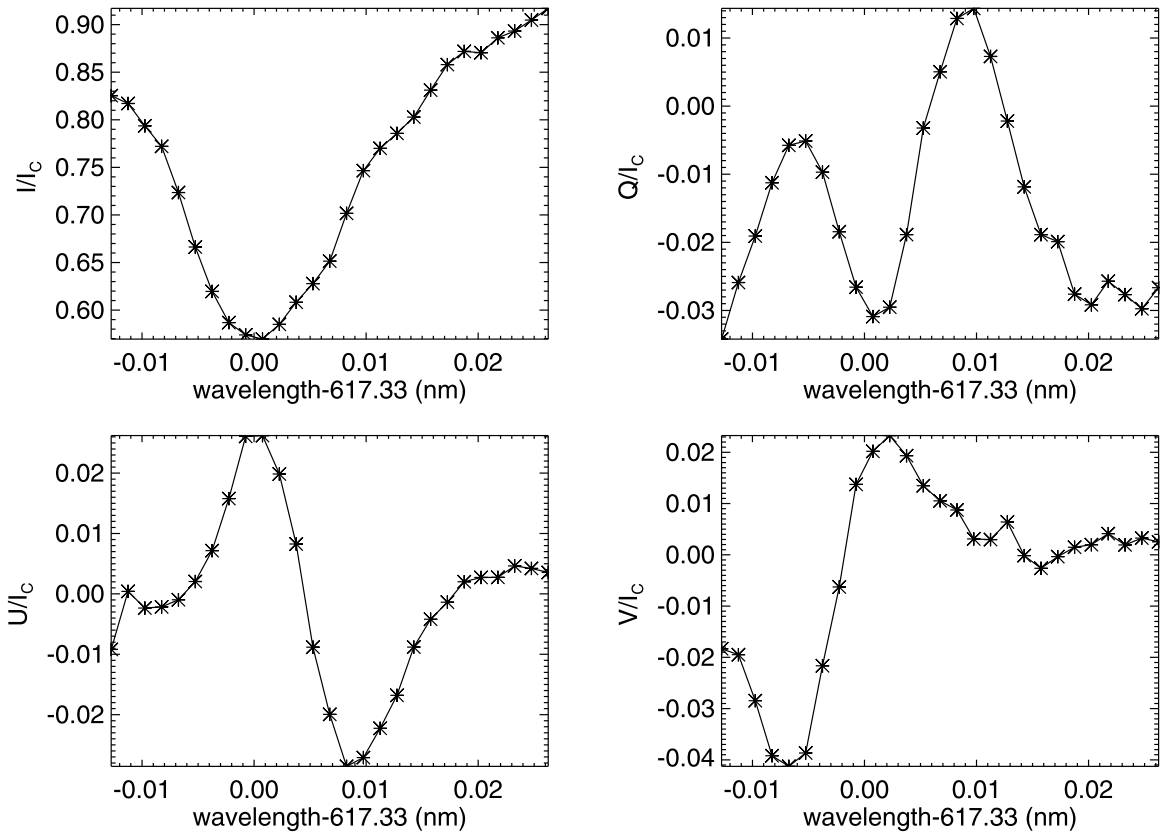

Figure 18 Profiles of Stokes parameters I, Q, U, and V at a point in the penumbra of NOAA AR 12470 corresponding to the star mark in Figure 17.

could be applied to the etalon is restricted, the retuning was done by changing the operating temperature. The retuning allowed us to start the line profile scan from a wavelength point farther out blue in the continuum. The following example of the Stokes V scan was carried out after the retuning of the filters. These observations were taken on 16 April 2016. Here the sunspot in NOAA AR 12529 (N10, W38) was observed with the polarimeter. The observations were obtained between 07:00 UT and 07:30 UT. During data acquisition, the seeing was again moderate. Unlike the previous observations, instead of 27 wavelength positions, we increased the wavelength spacing to 30 mÅ, which resulted in around 20 spectral positions on the 6173 Å line for the wavelength scan. Figure 19 shows the images for the wavelength position +75 mÅ from the line center and the corresponding mean Stokes V profile (right) for the entire FOV. In this case, the wavelength scan started well in the blue continuum, and the Stokes V signal also covers enough continuum wavelength points.

5.5. Stokes V Measurement in the Ca II 8542 Å Line

In this section, we report the circular polarization measurements obtained in the chromospheric Ca II 8542 Å line. The measurements were carried out with the second pair of LCVRs specifically procured for this wavelength. The imager was tuned to the blue wing −150 mÅ from the line center. The LCVR was sequentially switched between voltages corresponding to the modulation voltages for the left and right circular polarizations. A pair of 100 images were obtained for this measurement with an exposure time of 120 ms for each image. In Figure 20, the left image shows one of the selected $I + V$ images from these observations, and the right panel shows the mean V image at the above wavelength point.

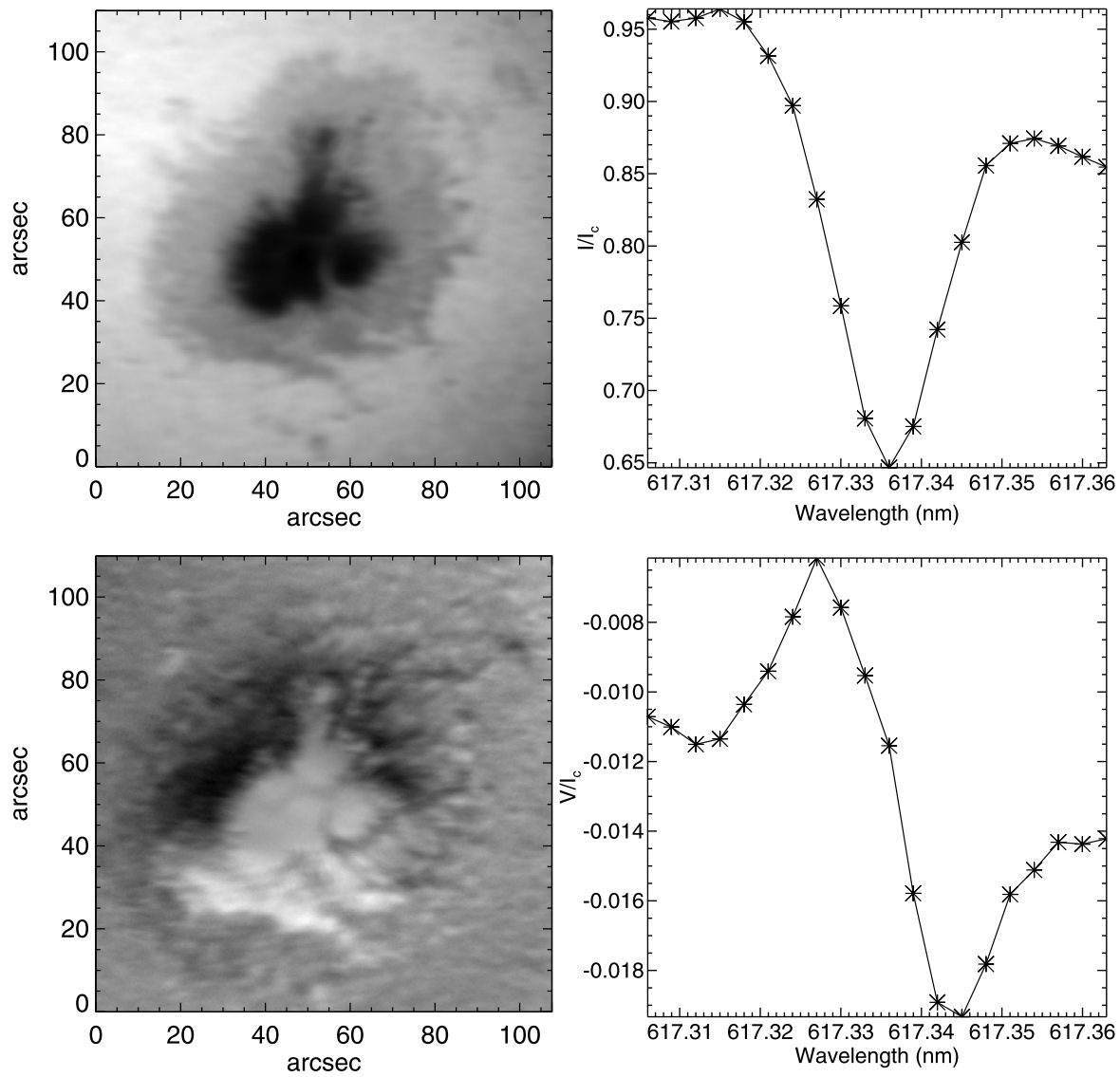

Figure 19 Stokes I and V observations of Active Region NOAA AR 12529 in the spectral line 6173 Å. Top row: Mean intensity (Stokes I) image (left) and its mean intensity profile (right). Bottom row: Mean Stokes V image (left) and its mean profile (right).

A clear Stokes V signal is present in the difference image (Figure 20, right), the seeing variations and the long exposure times produce artifacts, which will definitely be reduced by the ongoing adaptive optics installation. In the above observations, the images were taken only at one wavelength position, but the filter can be tuned to a considerable part of the Ca II 8542 Å line profile, which will be done in the future observations. A linear polarization measurement is also planned for this line.

6. Summary

The imaging spectropolarimeter for MAST was developed to obtain magnetic field information of the Sun in the spectral lines 6173 Å and 8542 Å, which are formed in the photosphere and chromosphere, respectively. The spectropolarimeter includes an FP-based narrow-band filter, and the polarimeter consists of a pair of nematic LCVRs and a linear polarizer. In this article, we have presented the characterization of the LCVRs and its retardance as a func-

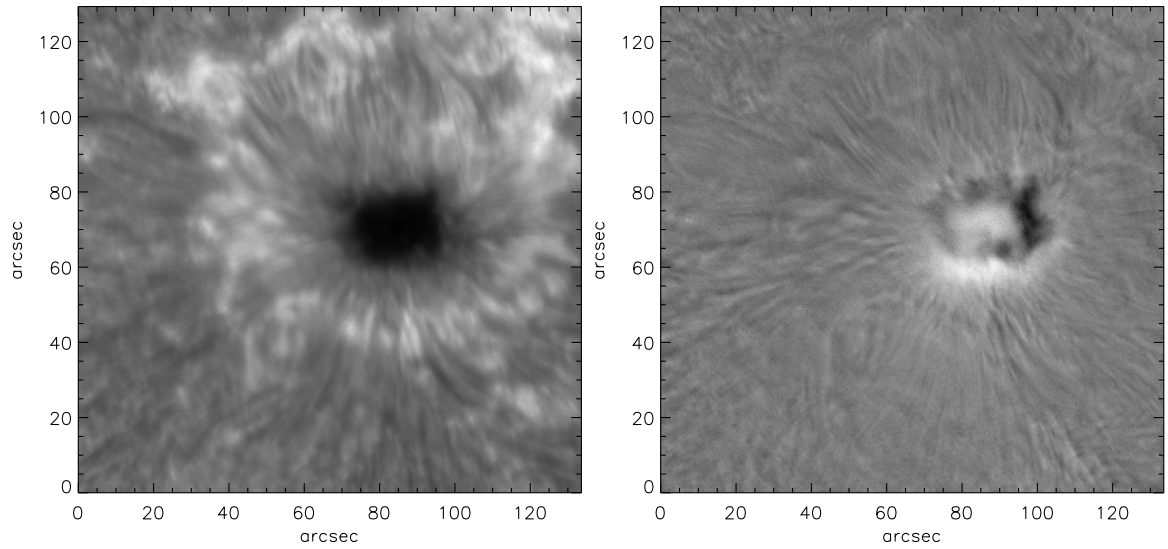

Figure 20 Chromospheric observations in LOS mode of NOAA AR 12546 (S07, E19) observed on 18 May 2016 between 08:30 UT and 08:36 UT using the MAST polarimeter. Images of $I + V$ (left) and mean Stokes parameter V (right) at a wavelength position -150 mÅ from the line center.

tion of voltage and temperature. The response matrix of the polarimeter was obtained using an experimental setup. We also discussed the implementation of four- and six-measurement schemes that are normally employed in obtaining the spectropolarimetric observations. Using the information obtained from the characterization of LCVRs, we obtained preliminary observations in Fe I 6173 Å. For the testing purpose, these observations were acquired by scanning the line profile of Fe I 6173 Å at 27 wavelength positions with a sample of 15 mÅ. We plan to minimize the number of wavelength positions to 8 – 12 to improve the observation cadence. As HMI also provides similar observations, we compared the Stokes I and V observations from MAST with those of SDO/HMI. Qualitatively, the two observations agree well, considering the fact that MAST observations are seeing limited.

In order to obtain the vector magnetic fields of the active region, Stokes Q, and U along with Stokes I and V were also obtained. However, we did not derive the magnetic fields from these observations as this requires information regarding instrument-induced polarization. In this regard, it is important to note that MAST is a nine-mirror system with two off-axis parabolic mirrors and seven plane-oblique mirrors. We have planned to obtain the instrument-induced polarization both theoretically (Anche *et al.*, 2015; Sen and Kakati, 1997) and experimentally (Selbing, 2010). In this article, we also presented the Stokes I and V observations of an active region in Ca II 8542 Å, which is formed in the chromosphere.

Acknowledgements We sincerely thank the referee for valuable comments that helped us to improve the content in the manuscript. The HMI data used here are courtesy of NASA/SDO and the HMI science team. We thank the HMI science team for making available the processed data of $I - V$ (LCP) and $I + V$ (RCP) for our comparative study. We also acknowledge the work of Mukesh M. Sardava of USO in the design and fabrication of the mount for the LCVRs and polarizers.

Disclosure of Potential Conflicts of Interest The authors declare that they have no conflicts of interest.

References

Anche, R.M., Anupama, G.C., Reddy, K., Sen, A., Sankarasubramanian, K., Ramaprakash, A.N., Sengupta, S., Skidmore, W., Atwood, J., Tirupathi, S., Pandey, S.B.: 2015, Analytical modelling of Thirty Meter Telescope optics polarization. In: *Proc. SPIE* **9654**, 965408. DOI. ADS.

Barthol, P., Gandorfer, A., Solanki, S.K., Schüssler, M., Chares, B., Curdt, W., Deutsch, W., Feller, A., Germerott, D., Grauf, B., Heerlein, K., Hirzberger, J., Kolleck, M., Meller, R., Müller, R., Riethmüller, T.L., Tomasch, G., Knölker, M., Lites, B.W., Card, G., Elmore, D., Fox, J., Lecinski, A., Nelson, P., Summers, R., Watt, A., Martínez Pillet, V., Bonet, J.A., Schmidt, W., Berkefeld, T., Title, A.M., Domingo, V., Gasent Blesa, J.L., Del Toro Iniesta, J.C., López Jiménez, A., Álvarez-Herrero, A., Sabau-Graziati, L., Widani, C., Haberler, P., Härtel, K., Kampf, D., Levin, T., Pérez Grande, I., Sanz-Andrés, A., Schmidt, E.: 2011, The Sunrise mission. *Solar Phys.* **268**, 1. DOI. ADS.

Beck, C., Schmidt, W., Kentischer, T., Elmore, D.: 2005, Polarimetric Littrow Spectrograph – instrument calibration and first measurements. *Astron. Astrophys.* **437**, 1159. DOI. ADS.

Beck, C., Bellot Rubio, L.R., Kentischer, T.J., Tritschler, A., Del Toro Iniesta, J.C.: 2010, Two-dimensional solar spectropolarimetry with the KIS/IAA Visible Imaging Polarimeter. *Astron. Astrophys.* **520**, A115. DOI. ADS.

Bello González, N., Kneer, F.: 2008, Narrow-band full Stokes polarimetry of small structures on the Sun with speckle methods. *Astron. Astrophys.* **480**, 265. DOI. ADS.

Bendlin, C., Volkmer, R., Kneer, F.: 1992, A new instrument for high resolution, two-dimensional solar spectroscopy. *Astron. Astrophys.* **257**, 817. ADS.

Born, M., Wolf, E.: 1999, *Principles of Optics*, 7th edn. Cambridge University Press, Cambridge.

Borrero, J.M., Ichimoto, K.: 2011, Magnetic structure of sunspots. *Living Rev. Solar Phys.* **8**, 4. DOI. ADS.

Capobianco, G., Crudelini, F., Zangrilli, L., Buscemi, C., Fineschi, S.: 2008, E-KPol temperature calibration. http://www.to.astro.it/biblioteca/pdf/TechRep111_Capobianco.pdf.

Cavallini, F.: 2006, IBIS: a new post-focus instrument for solar imaging spectroscopy. *Solar Phys.* **236**, 415. DOI. ADS.

Chandrasekhar, S.: 1960, *Radiative Transfer*. ADS.

de Gennes, P.G., Prost, J., Pelcovits, R.: 1995, The physics of liquid crystals. *Phys. Today* **48**, 70. DOI. ADS.

de Juan Ovelar, M., Snik, F., Keller, C.U., Venema, L.: 2014, Instrumental polarisation at the Nasmyth focus of the E-ELT. *Astron. Astrophys.* **562**, A8. DOI. ADS.

Del Toro Iniesta, J.C.: 2003, *Introduction to Spectropolarimetry*, 244. ADS.

del Toro Iniesta, J.C., Collados, M.: 2000, Optimum modulation and demodulation matrices for solar polarimetry. *Appl. Opt.* **39**, 1637. DOI. ADS.

Del Toro Iniesta, J.C., Martínez Pillet, V.: 2012, Assessing the behavior of modern solar magnetographs and spectropolarimeters. *Astron. Astrophys. Suppl.* **201**, 22. DOI. ADS.

Denis, S., Coucke, P., Gabriel, E., Delrez, C., Venkatakrishnan, P.: 2008, Optomechanical and thermal design of the Multi-Application Solar Telescope for USO. In: *Ground-based and Airborne Telescopes II*, *Proc. SPIE* **7012**, 701235. DOI. ADS.

Denis, S., Coucke, P., Gabriel, E., Delrez, C., Venkatakrishnan, P.: 2010, Multi-Application Solar Telescope: assembly, integration, and testing. In: *Proc. SPIE* **7733**, 773335. DOI. ADS.

Denker, C., Balthasar, H., Hofmann, A., Bello González, N., Volkmer, R.: 2010, The GREGOR Fabry–Perot interferometer: a new instrument for high-resolution solar observations. In: *SPIE Conf. Ser.* **7735**, 6. DOI. ADS.

Haller, I.: 1975, Thermodynamic and static properties of liquid crystals. *Prog. Solid State Chem.* **10**, 103. DOI. http://www.sciencedirect.com/science/article/pii/0079678675900084.

Hanle, W.: 1924, Über magnetische Beeinflussung der Polarisation der Resonanzfluoreszenz. *Z. Phys.* **30**, 93. DOI. ADS.

Hecht, E.: 2001, *Optics*, 4th edn. Addison-Wesley, Reading. ADS.

Heredero, R.L., Uribe-Patarroyo, N., Belenguer, T., Ramos, G., Sánchez, A., Reina, M., Martínez Pillet, V., Álvarez-Herrero, A.: 2007, Liquid-crystal variable retarders for aerospace polarimetry applications. *Appl. Opt.* **46**, 689. DOI. ADS.

Ichimoto, K., Lites, B., Elmore, D., Suematsu, Y., Tsuneta, S., Katsukawa, Y., Shimizu, T., Shine, R., Tarbell, T., Title, A., Kiyohara, J., Shinoda, K., Card, G., Lecinski, A., Streander, K., Nakagiri, M., Miyashita, M., Noguchi, M., Hoffmann, C., Cruz, T.: 2008, Polarization calibration of the Solar Optical Telescope onboard Hinode. *Solar Phys.* **249**, 233. DOI. ADS.

Lagg, A., Lites, B., Harvey, J., Gosain, S., Centeno, R.: 2015, Measurements of photospheric and chromospheric magnetic fields, *Space Sci. Rev.* DOI. ADS.

Leka, K.D., Rangarajan, K.E.: 2001, Effects of 'seeing' on vector magnetograph measurements. *Solar Phys.* **203**, 239. DOI. ADS.

Li, J., Gauzia, S., Wu, S.-T.: 2004, High temperature-gradient refractive index liquid crystals. *Opt. Express* **12**, 2002. DOI. ADS.

Lites, B.W.: 1987, Rotating waveplates as polarization modulators for Stokes polarimetry of the Sun – evaluation of seeing-induced crosstalk errors. *Appl. Opt.* **26**, 3838. DOI. ADS.

Ma, L., Zhou, W., Zhou, G., Zhang, J.: 2015, The evolution of arch filament systems and moving magnetic features around a sunspot. *Astron. Astrophys.* **583**, A110. DOI. ADS.

Martinez Pillet, V., Bonet, J.A., Collados, M.V., Jochum, L., Mathew, S., Medina Trujillo, J.L., Ruiz Cobo, B., del Toro Iniesta, J.C., Lopez Jimenez, A.C., Castillo Lorenzo, J., Herranz, M., Jeronimo, J.M., Mellado, P., Morales, R., Rodriguez, J., Alvarez-Herrero, A., Belenguer, T., Heredero, R.L., Menendez, M., Ramos, G., Reina, M., Pastor, C., Sanchez, A., Villanueva, J., Domingo, V., Gasent, J.L., Rodriguez, P.: 2004, The imaging magnetograph eXperiment for the SUNRISE balloon Antarctica project. In: Mather, J.C. (ed.) *Optical, Infrared, and Millimeter Space Telescopes*, *SPIE Conf. Ser.* **5487**, 1152. DOI. ADS.

Martínez Pillet, V., Del Toro Iniesta, J.C., Álvarez-Herrero, A., Domingo, V., Bonet, J.A., González Fernández, L., López Jiménez, A., Pastor, C., Gasent Blesa, J.L., Mellado, P., Piqueras, J., Aparicio, B., Balaguer, M., Ballesteros, E., Belenguer, T., Bellot Rubio, L.R., Berkefeld, T., Collados, M., Deutsch, W., Feller, A., Girela, F., Grauf, B., Heredero, R.L., Herranz, M., Jerónimo, J.M., Laguna, H., Meller, R., Menéndez, M., Morales, R., Orozco Suárez, D., Ramos, G., Reina, M., Ramos, J.L., Rodríguez, P., Sánchez, A., Uribe-Patarroyo, N., Barthol, P., Gandorfer, A., Knoelker, M., Schmidt, W., Solanki, S.K., Vargas Domínguez, S.: 2011, The Imaging Magnetograph eXperiment (IMaX) for the Sunrise Balloon-Borne Solar Observatory. *Solar Phys.* **268**, 57. DOI. ADS.

Mathew, S.K.: 2009, A new 0.5 m telescope (MAST) for solar imaging and polarimetry. In: Berdyugina, S.V., Nagendra, K.N., Ramelli, R. (eds.) *Solar Polarization 5: In Honor of Jan Stenflo*, *Astron. Soc. Pac. Conf. Ser.* **405**, 461. ADS.

Mathew, S.K., Bayanna, A.R., Tiwary, A.R., Ramya, B., Venkatakrishnan, P.: 2017, First observations from the Multi-Application Solar Telescope (MAST) narrow band imager. *Solar Phys.*, submitted.

Mickey, D.L., Canfield, R.C., Labonte, B.J., Leka, K.D., Waterson, M.F., Weber, H.M.: 1996, The imaging vector magnetograph at Haleakala. *Solar Phys.* **168**, 229. DOI. ADS.

Pesnell, W.D., Thompson, B.J., Chamberlin, P.C.: 2012, The Solar Dynamics Observatory (SDO). *Solar Phys.* **275**, 3. DOI. ADS.

Puschmann, K.G.: 2016, The GREGOR Fabry Perot Interferometer (GFPI), Technical innovations and results achieved in 2013, *arXiv e-prints*. ADS.

Raja Bayanna, A., Mathew, S.K., Venkatakrishnan, P., Srivastava, N.: 2014, Narrow-band imaging system for the Multi-Application Solar Telescope at Udaipur Solar Observatory: characterization of lithium niobate etalons. *Solar Phys.* **289**, 4007. DOI. ADS.

Saleh, B.E.A., Teich, M.C.: 2007, *Fundamentals of Photonics*, Wiley-Interscience, New York. 978-0471358329. Chap. 18.

Sankarasubramanian, K., Elmore, D.F., Lites, B.W., Sigwarth, M., Rimmele, T.R., Hegwer, S.L., Gregory, S., Streander, K.V., Wilkins, L.M., Richards, K., Berst, C.: 2003, Diffraction limited spectro-polarimeter – phase I. In: Fineschi, S. (ed.) *Polarimetry in Astronomy*, *SPIE Conf. Ser.* **4843**, 414. DOI. ADS.

Scharmer, G.B., Narayan, G., Hillberg, T., de la Cruz Rodríguez, J., Löfdahl, M.G., Kiselman, D., Sütterlin, P., van Noort, M., Lagg, A.: 2008, CRISP spectropolarimetric imaging of penumbral fine structure. *Astrophys. J. Lett.* **689**, L69. DOI. ADS.

Scherrer, P.H., Schou, J., Bush, R.I., Kosovichev, A.G., Bogart, R.S., Hoeksema, J.T., Liu, Y., Duvall, T.L., Zhao, J., Title, A.M., Schrijver, C.J., Tarbell, T.D., Tomczyk, S.: 2012, The Helioseismic and Magnetic Imager (HMI) investigation for the Solar Dynamics Observatory (SDO). *Solar Phys.* **275**, 207. DOI. ADS.

Schou, J., Scherrer, P.H., Bush, R.I., Wachter, R., Couvidat, S., Rabello-Soares, M.C., Bogart, R.S., Hoeksema, J.T., Liu, Y., Duvall, T.L., Akin, D.J., Allard, B.A., Miles, J.W., Rairden, R., Shine, R.A., Tarbell, T.D., Title, A.M., Wolfson, C.J., Elmore, D.F., Norton, A.A., Tomczyk, S.: 2012, Design and ground calibration of the Helioseismic and Magnetic Imager (HMI) instrument on the Solar Dynamics Observatory (SDO). *Solar Phys.* **275**, 229. DOI. ADS.

Selbing, J.: 2010, SST polarization model and polarimeter calibration. arXiv. ADS.

Sen, A.K., Kakati, M.: 1997, Instrumental polarization caused by telescope optics during wide field imaging. *Astron. Astrophys. Suppl.* **126**, 113 DOI. ADS.

Shin-Tson Wu, D.-K.Y.: 2001, *Reflective Liquid Crystal Displays*, Wiley, New York.

Socas-Navarro, H., Elmore, D., Pietarila, A., Darnell, A., Lites, B.W., Tomczyk, S., Hegwer, S.: 2006, Spinor: visible and infrared spectro-polarimetry at the National Solar Observatory. *Solar Phys.* **235**, 55. DOI. ADS.

Solanki, S.K.: 2003, Sunspots: an overview. *Astron. Astrophys. Rev.* **11**, 153. DOI. ADS.

Stenflo, J.O.: 2015, History of solar magnetic fields since George Ellery Hale. *Space Sci. Rev.* DOI. ADS.

Stix, M.: 2004, *The Sun*, 2nd edn. Springer, Berlin.

Terrier, P., Charbois, J.M., Devlaminck, V.: 2010, Fast-axis orientation dependence on driving voltage for a Stokes polarimeter based on concrete liquid-crystal variable retarders. *Appl. Opt.* **49**, 4278. DOI. ADS.

Tomczyk, S., Casini, R., de Wijn, A.G., Nelson, P.G.: 2010, Wavelength-diverse polarization modulators for Stokes polarimetry. *Appl. Opt.* **49**, 3580. DOI. ADS.

Trujillo Bueno, J.: 2014, Polarized radiation observables for probing the magnetism of the outer solar atmosphere. In: Nagendra, K.N., Stenflo, J.O., Qu, Q., Samooprna, M. (eds.) *Solar Polarization 7*, *Astron. Soc. Pac. Conf. Ser.* **489**, 137. ADS.

Tsuneta, S., Ichimoto, K., Katsukawa, Y., Nagata, S., Otsubo, M., Shimizu, T., Suematsu, Y., Nakagiri, M., Noguchi, M., Tarbell, T., Title, A., Shine, R., Rosenberg, W., Hoffmann, C., Jurcevich, B., Kushner, G., Levay, M., Lites, B., Elmore, D., Matsushita, T., Kawaguchi, N., Saito, H., Mikami, I., Hill, L.D., Owens, J.K.: 2008, The Solar Optical Telescope for the Hinode mission: an overview. *Solar Phys.* **249**, 167. DOI. ADS.

Wiegelmann, T., Petrie, G.J.D., Riley, P.: 2015, Coronal magnetic field models. *Space Sci. Rev.*. DOI. ADS.

Wiegelmann, T., Sakurai, T.: 2012, Solar force-free magnetic fields. *Living Rev. Solar Phys.* **9**(5), 5 DOI. http://www.livingreviews.org/lrsp-2012-5.

Zeeman, P.: 1897, On the influence of magnetism on the nature of the light emitted by a substance. *Astrophys. J.* **5**, 332. DOI. ADS.

applied optics

Estimation of order parameter of a liquid crystal variable retarder using Haller's approximation

Alok Ranjan Tiwary,[1,2,*] A. Raja Bayanna,[1] and Shibu K. Mathew[1]

[1]Udaipur Solar Observatory, Physical Research Laboratory, Dewali, Badi Road, Udaipur 313001, India
[2]Indian Institute of Technology, Gandhinagar, Gujarat 382424, India
*Corresponding author: atiwary@prl.res.in

Received 2 March 2017; revised 16 April 2017; accepted 16 April 2017; posted 18 April 2017 (Doc. ID 287833); published 9 May 2017

We use a liquid crystal variable retarder (LCVR) for polarization modulation of the input beam in a polarimeter intended for solar observations. It is known that the retardance of LCVR depends on the voltage and temperature. Voltage at a constant temperature is used for fast modulation. However, fluctuations in the temperature reduce the accuracy in the polarimetric measurements. In order to understand these, we have performed calibration of the LCVR with respect to temperature and estimated the different parameters, critical exponent (β), maximum retardance (δ_0), and order parameter (S) of the liquid crystal using Haller's approximation. We also study the dependence of these parameters with voltage. It is observed that the change in order parameter with change in temperature varies linearly with voltage in the range of 1–7 V.

OCIS codes: (120.5410) Polarimetry; (230.3720) Liquid-crystal devices; (230.4110) Modulators; (120.6780) Temperature.

https://doi.org/10.1364/AO.56.004180

1. INTRODUCTION

Liquid crystals are finding use in many areas, particularly in display technology [1,2]. They are used for making optical devices such as tunable filters [3,4], shutters [5,6], and variable retarders [7]. Liquid crystal variable retarders (LCVRs) provide the variable retardance without the need of any moving mechanical parts, with added advantages of low mass and low power consumption [8,9]. These devices find importance in polarimetry [10] [and references therein] because of their high switching speeds. With this speed, the modulated images can be acquired at a fast rate to minimize the atmospheric seeing-induced errors in the polarized light in the case of ground-based telescopes.

A polarimeter is an instrument which is used for measuring the polarization state of light [11]. A LCVR-based polarimeter can be used to perform these measurements, where the polarization state is typically characterized in terms of the four-element Stokes vector. LCVRs have been widely used as polarimetric devices in ground- as well as in space-based solar telescopes [12]. There are several LCVR-based polarimeters which are being used for solar magnetic field measurements, such as the CRisp imaging spectropolarimeter (CRISP, [13]) and imaging spectropolarimeters [14] for multi-application solar telescopes [15–17]. LCVRs were also used in the imaging magnetograph eXperiment (IMaX, [18]) onboard the SUNRISE balloon mission [19].

LCVR-based polarimeters usually consist of two LCVRs and a linear polarizer, as shown in Fig. 1. Since the LCVR is the key component of the polarimeter, the precise characterization of the LCVR is very important to achieve better polarimetric accuracy. The retardance of the LCVR largely depends on the voltage for a particular wavelength. But it also depends on the temperature according to Haller's approximation, as explained in Section 2.

In this paper, we present the dependence of the retardance of LCVR on the temperature and estimates of the optical parameters used in Haller's approximations [20]. We also show the dependence of these optical parameters with voltage which depicts the complex behavior of liquid crystals in the presence of an electric field. This paper has been organized in the following manner. Theoretical description of the liquid crystals is discussed in Section 2. In Section 3, we describe the experimental setup used for the characterization of the LCVR with temperature. Results and the relevant discussion are presented in Section 4.

2. THEORY

The states of matter whose symmetric and mechanical properties are intermediate between those of a crystalline solid and an isotropic liquid are called "liquid crystals." The most fundamental characteristic of a liquid crystal is the presence of long-range orientational order, while the positional order is either limited (smectic phases) or absent altogether (nematic phases). One phase differs from the other with respect to its symmetry [21]. The transition between different phases corresponds to the breaking of the symmetry and can be described in

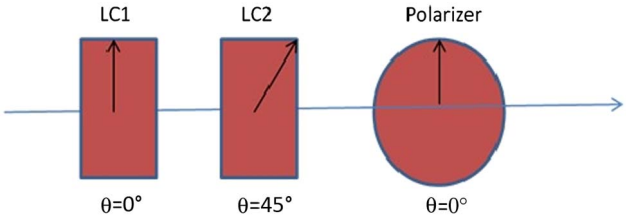

Fig. 1. Schematic layout of a Stokes polarimeter with two LCVRs and a linear polarizer.

terms of order parameter (S), which describe the phase transition. The order parameter S is defined as

$$S = \left\langle \frac{3}{2}\cos^2\theta - \frac{1}{2} \right\rangle, \tag{1}$$

where θ represents the angle between the main axis of a particular molecule and the average orientation of all molecules, and $\langle\rangle$ symbolizes an average over the entire system. Here, $S = 1$ corresponds to a perfectly aligned liquid crystal, and $S = 0$ to an isotropic state [22].

It is well known that S decreases with temperature, and that near the nematic-isotropic transition temperature (T_c), it drops noncontinuously to zero. This behavior with temperature can be understood as when the molecules gain energy, they can depart more from order than at lower temperatures due to the combined effects of entropy and energy. Considering this, Haller has shown that the order parameter can be described over the entire nematic temperature range by the following relation [20]:

$$S = \left(1 - \frac{T}{T_C}\right)^{\beta}, \tag{2}$$

where β is a critical exponent related to the phase transition. β also has a dependence on the birefringence, which in turn depends on the applied voltage. This shows that the order parameter also depends on the applied voltage. Liquid crystal devices, such as LCVR, are used to change the modulation of the input beam by changing the retardance with the application of voltage. In the absence of applied voltage, LCVR produces maximum retardance as the director (long axes of the liquid crystal molecules) of the liquid crystal is parallel to the interfaces. The retardance would be low if all molecules are not aligned parallel to the interface. Retardance and the order parameter are related by the equation [23]

$$\begin{aligned} \delta &= \delta_0 S, \\ &= \delta_0 \left(1 - \frac{T}{T_C}\right)^{\beta}, \end{aligned} \tag{3}$$

where δ_0 is the retardance for $S = 1$. As evident from the above equation, for a particular voltage as temperature increases, S and δ decrease. Thus, from the measurements of retardance as a function of voltage at different temperatures, the behavior of S can be understood.

3. EXPERIMENT

Figure 2 shows the experimental setup used for the characterization of LCVRs. A stabilized DC lamp is used as a white light source (**S**). A diffuser is used to get uniform intensity. A lens

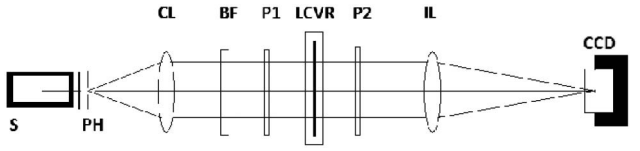

Fig. 2. Schematic diagram of the experimental setup used for the calibration of LCVR: a light source (**S**) from a pinhole (PH) is collimated using a lens (CL). This collimating beam passes through a blocking filter (BF), linear polarizer (P1), and a LCVR whose fast axis is kept at 45° with respect to P1. Light analyzed by the polarizer (or analyzer) P2 is imaged on to the CCD camera using imaging lens (IL).

(CL) collimates the light from pinhole (PH) which is placed after the diffuser for point source representation. An interference filter (or blocking filter, BF) is employed in order to select the particular wavelength for which characterization of the LCVRs is carried out. For the present study, we are using a BF centered at 6173 Å with a pass band of 5 Å. Two Glan–Thompson polarizing prisms (P1 and P2) are used as a polarizer and an analyzer, and the LCVR is placed in between them. The LCVR is placed in a thermally controlled enclosure to maintain the temperature. The accuracy of the enclosure is ±0.5°C. Another lens (IL) is placed after the analyzer (P2) to image the beam onto a CCD camera to measure the intensity of the output light.

The incoming light is linearly polarized by the polarizer P1. After being retarded by the LCVR, whose fast axis is at 45°, the light is analyzed by the second polarizer P2. Polarizer P2 is mounted on a computer controlled rotation stage to measure the intensities at two different orientations. The intensities I_{out} at two different angles, $\theta = 90°$ and $\theta = 0°$, are measured by rotating the polarizer P2. Retardance δ of the LCVR has been calculated using Eq. (4) [14] at different applied voltages to LCVR:

$$\delta = \cos^{-1}\left(\frac{I^0_{\text{out}} - I^{90}_{\text{out}}}{I^0_{\text{out}} + I^{90}_{\text{out}}}\right). \tag{4}$$

The experiment is repeated, changing the temperature of the enclosure of the LCVR. Change in retardance of LCVR with voltage at different temperatures is shown in the left panel of Fig. 4.

4. RESULTS AND DISCUSSION

Equation (3) shows that the temperature also influences the retardances of LCVRs. We have characterized voltage dependence of retardance of a LCVR at four different temperatures, i.e., 28°C, 30°C, 35°C, and 40°C. Retardance estimated with the application of voltage at a **T** = 28°C is shown in Fig. 3. The left and right panels of Fig. 3 show the retardance without phase unwrapping and with phase unwrapping, respectively. Here, it is to be noted that the left panel of Fig. 3 shows two regions, R1 and R2, which need phase unwrapping for a continuous curve. As the retardance required for polarimetry is in the range of 360–50 deg, we have not performed the phase unwrapping in the higher voltage range (R2), where the retardances are very small. For comparison, data obtained from the manufacturer is also shown here. It is evident that our

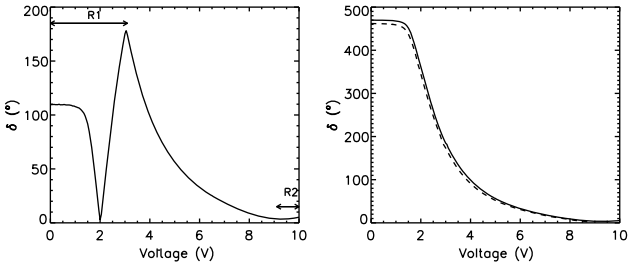

Fig. 3. Left: retardance versus voltage applied to a LCVR for a wavelength of 617.3 nm. Measurements were made in steps of 0.05 V from 0 to 10 V. Right: comparison between the curve provided by the manufacturer (dashed line) of the LCVR and that obtained with our procedure (continuous line). It is evident from the figure that our measurement is in agreement with that of manufacturer. However, the minor difference observed in both the curves is due to a change in the wavelength of the light used. Our measurements are performed for a light of wavelength centered at 6173 Å, whereas the data provided by the manufacturer is for 6302 Å.

measurement is in agreement with that of the manufacturer. However, the minor difference observed in both the curves is due to the change in the wavelength of the light used. Our measurements are performed for a light of wavelength centered at 6173 Å, whereas the data provided by the manufacturer is for 6302 Å.

Figure 4 shows the retardance as a function of voltage at different temperatures. As evident from Fig. 4 (left), retardance of the LCVR decreases as its temperature increases. At lower voltages (0–2 V), the applied electric field may not be sufficient to provide the torque to change the orientation of liquid crystal molecules, so it remains parallel to the interfaces; here temperature influence is dominant. However, at higher voltages ($V > 6$ V), torque due to the applied electric field is strong enough to not be influenced by the temperature, i.e., change in retardance due to voltage is more dominant than the change

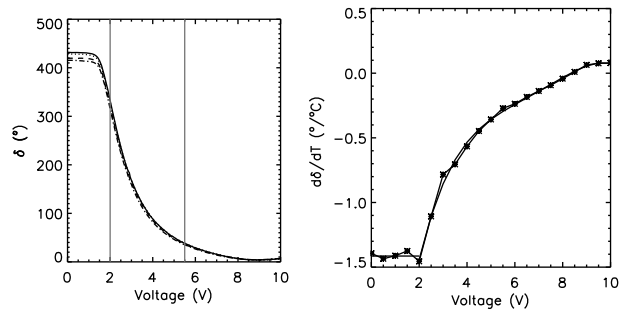

Fig. 4. Left: variation of the retardance with the applied voltage of the LCVR for four different temperatures. Continuous, dotted, dashed, and dotted-dashed curves are corresponding to temperatures 28°C, 30°C, 35°C, and 40°C, respectively. The vertical line represents different voltage regimes in which influence of voltage and temperature on retardance varies. Right: retardance derivative with respect to the temperature as a function of voltage, which shows that LCVR is insensitive to temperature for higher voltages. Thin line with asterisk symbols represents $d\delta/dT$, derived using the data shown in the left panel, and the polynomial fit is shown with a thick line. This figure is reproduced from [14].

in retardance due to temperature. In the intermediate regime (2–6 V), both temperature and voltage play a role in changing the retardance. The effect of temperature on the retardance of the LCVR can be clearly seen in the right panel of Fig. 4. It shows that the LCVR is more sensitive to the temperature when it is operated at low voltages, and it is nearly constant in the voltage range 0–2 V.

A relation between temperature sensitivity ($d\delta/dT$) and voltage is obtained for two regions of voltage separately using polynomial fit of the order 1 and 4, respectively. When we fit the entire data with a polynomial fit, the chi-square value is higher. Hence, the data is divided into two regimes ($V \leq 2$ and $2 < V > 10$) and used to find an appropriate polynomial fit as shown below:

$$\frac{d\delta}{dT} = -1.41 \quad \forall\ V \leq 2,$$
$$\frac{d\delta}{dT} = -4.03 + 1.97V - 0.41V^2 + 0.04V^3 - 0.0014V^4$$
$$\forall\ 2 < V < 10. \tag{5}$$

Using Eq. (3), it can be shown that

$$\frac{dS}{dT} = \frac{1}{\delta_0}\frac{d\delta}{dT}. \tag{6}$$

The above equation shows that in order to know the sensitivity of the order parameter (S), it is important to know the δ_0, which depends on the applied voltage. Hence, δ_0 and β are estimated by rearranging the experimental data as shown in Fig. 5.

The asterisk symbols in the left panel of Fig. 5 depict the temperature dependence of the retardance at a fixed voltage 3.967 V (voltage corresponding to quarter-wave retardance). The data (temperature versus retardance) is fitted to Eq. (3) in two ways: one, in which T_C is fixed at a known value of 368 K (95°C, provided by the manufacturer of LCVR, M/s Meadowlark Optics) for this particular LCVR (fit A), and another in which all the parameters are (fit B) obtained from the fit. Fit A yields $\beta = 0.395 \pm 0.086$ and $\delta_0 = 178.5 \pm 27.4$.

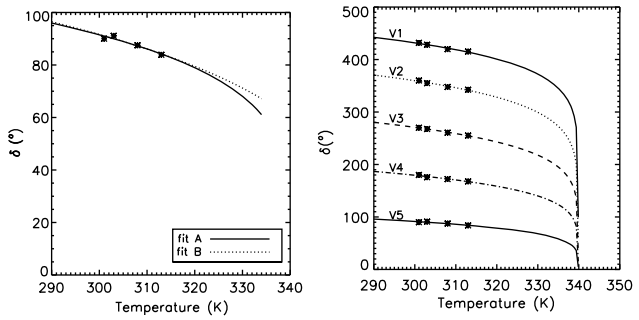

Fig. 5. Left: temperature versus retardance, keeping the LCVRs at a voltage corresponding to quarter-wave plate ($V = 3.967$ V). Asterisk symbols show the experimental data, and the curves show the corresponding fits using the two methods (Fit A and Fit B). For Fit A, temperature is fixed at 368 K. For Fit B, all three parameters are varied to fit Eq. (3). Right: retardance versus temperature for different voltages: $V1 = 0.0$, $V2 = 1.861$, $V3 = 2.318$, $V4 = 2.918$, and $V5 = 3.967$ V at a constant $T_C = 339.9$ K. These voltages correspond to retardance of maximum, λ, $3\lambda/4$, $\lambda/2$, and $\lambda/4$, respectively.

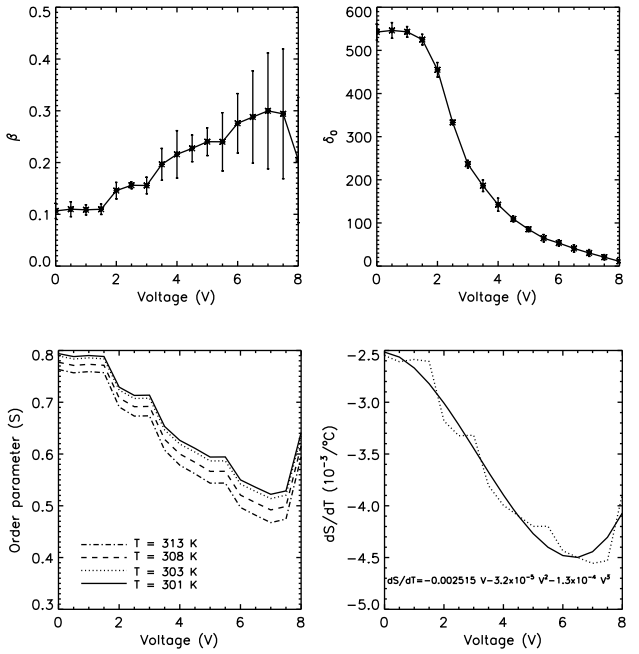

Fig. 6. Top left: change in critical exponent (β) with voltage. Right: change in δ_0 with voltage. The error bars correspond to 1-σ error. Bottom left: change in order parameter (S) with voltage at different temperatures. Right: change in order parameter (S) with respect to change in temperature.

The β value obtained here is more than the expected [20]. However, a better fit is obtained in the second method, which yields $\beta = 0.213 \pm 0.004$, $\delta_0 = 144.1 \pm 1.3$, and $T_C = 339.9 \pm 1.6$ K. As the percentage of deviation in the obtained parameter is smaller, we use the values β, δ_0, and T_C obtained here for further analysis. Using the derived value of T_C (339.9 K or 66.9°C) and Eq. (3), the data shown in Fig. 5 (right) is extrapolated for retardance as a function of temperature at different voltages (refer to Fig. 5). As the polarimeter uses voltages in the range of 0–4 V for achieving required retardance, we have shown only these five voltages in the plot.

Critical exponent β and maximum retardance δ_0 are also obtained for the voltage range 0–8 V using Eq. (3) with T_C at 340 K. Figure 6 depicts the change in β (top left panel) and δ_0 (top right panel) with voltage along with the 1-σ error bars. Change in β shows larger error at higher voltages. This could be due to the temperature sensitivity of retardance, which is very low at higher voltages (refer to Fig. 4). Also, β and δ_0 are almost constant in the low-voltage regime (0–2 V). The lower panel of Fig. 6 shows the variation of order parameters at different temperatures and voltages, and also change in the order parameter with respect to change in temperature.

The estimated order parameter varies between 0.45 and 0.8 for different combinations of voltage and temperature, and it decreases with an increase in temperature, as well as with the increase in voltage. It also shows that order parameter is more sensitive to voltage or the applied electric field than the temperature. $\frac{dS}{dT}$ shows the linear relation (approximately) with voltage (V). The difference in obtained equations for $\frac{d\delta}{dT}$ and $\frac{dS}{dT}$ could be due to the voltage dependence of the δ_0 as seen in the top right panel of Fig. 6. $\frac{dS}{dT}$ shows less complex behavior than the $\frac{d\delta}{dT}$. The complexity might have been normalized by the complex behavior of the voltage dependence of δ_0.

Acknowledgment. We sincerely thank the reviewers for their valuable comments that helped us to improve the content of the paper. We acknowledge the work done by Mr. Mukesh M. Sardava of Udaipur Solar Observatory in the design and fabrication of the mount for LCVRs and polarizers.

REFERENCES

1. J. Li, S. Gauza, and S.-T. Wu, "Temperature effect on liquid crystal refractive indices," J. Appl. Phys. **96**, 19–24 (2004).
2. J. A. Castellano, "Liquid crystal display applications: past, present & future," Liq. Cryst. Today **1**(1), 4–6 (1991).
3. Y.-H. Yao, C.-T. Wang, R.-R. Chen, H.-C. Jau, Y.-J. Chiu, and T.-H. Lin, "Wavelength tunable infrared light source based on semiconductor-integrated liquid crystal filter," Opt. Express **20**, 22872–22877 (2012).
4. H. Zhang, A. Muhammmad, J. Luo, Q. Tong, Y. Lei, X. Zhang, H. Sang, and C. Xie, "Electrically tunable infrared filter based on the liquid crystal Fabry-Perot structure for spectral imaging detection," Appl. Opt. **53**, 5632–5639 (2014).
5. P. Xu, X. Li, V. G. Chigrinov, and S. A. Studentsov, "Fast and high-contrast liquid-crystal shutters with low power consumption based on an optical-mode-interference cell," Appl. Opt. **45**, 4020–4025 (2006).
6. L. Komitov, G. Hegde, and D. Kolev, "Fast liquid crystal light shutter," J. Phys. D **44**, 442002 (2011).
7. B. E. A. Saleh and M. C. Teich, *Fundamentals of Photonics* (Wiley, 2007).
8. J. Shekwoga Baba and P. R. Boudreaux, "Wavelength, temperature, and voltage dependent calibration of a nematic liquid crystal multispectral polarization generating device," Appl. Opt. **46**, 5539–5544 (2007).
9. P. Terrier, J. M. Charbois, and V. Devlaminck, "Fast-axis orientation dependence on driving voltage for a Stokes polarimeter based on concrete liquid-crystal variable retarders," Appl. Opt. **49**, 4278–4283 (2010).
10. R. L. Heredero, N. Uribe-Patarroyo, T. Belenguer, G. Ramos, A. Sánchez, M. Reina, V. Martínez Pillet, and A. Álvarez-Herrero, "Liquid-crystal variable retarders for aerospace polarimetry applications," Appl. Opt. **46**, 689–698 (2007).
11. J. M. López-Téllez and N. C. Bruce, "Stokes polarimetry using analysis of the nonlinear voltage-retardance relationship for liquid-crystal variable retarders," Rev. Sci. Instrum. **85**, 033104 (2014).
12. A. Alvarez-Herrero, N. Uribe-Patarroyo, P. García Parejo, J. Vargas, R. L. Heredero, R. Restrepo, V. Martínez-Pillet, J. C. del Toro Iniesta, A. López, S. Fineschi, G. Capobianco, M. Georges, M. López, G. Boer, and I. Manolis, "Imaging polarimeters based on liquid crystal variable retarders: an emergent technology for space instrumentation," Proc. SPIE **8160**, 81600Y (2011).
13. G. B. Scharmer, G. Narayan, T. Hillberg, J. de la Cruz Rodríguez, M. G. Löfdahl, D. Kiselman, P. Sütterlin, M. van Noort, and A. Lagg, "CRISP spectropolarimetric imaging of penumbral fine structure," Astrophys. J. Lett. **689**, L69–L72 (2008).
14. A. R. Tiwary, S. K. Mathew, A. R. Bayanna, P. Venkatakrishnan, and R. Yadav, "Imaging spectropolarimeter for the multi-application solar telescope at Udaipur solar observatory: characterization of polarimeter and preliminary observations," Sol. Phys. **292**, 49 (2017).
15. S. Denis, P. Coucke, E. Gabriel, C. Delrez, and P. Venkatakrishnan, "Multi-application solar telescope: assembly, integration, and testing," Proc. SPIE **7733**, 773335 (2010).
16. S. Denis, P. Coucke, E. Gabriel, C. Delrez, and P. Venkatakrishnan, "Optomechanical and thermal design of the multi-application solar telescope for USO," Proc. SPIE **7012**, 701235 (2008).
17. S. K. Mathew, "A new 0.5 m telescope (MAST) for solar imaging and polarimetry," in *Solar Polarization 5: In Honor of Jan Stenflo*, S. V. Berdyugina, K. N. Nagendra, and R. Ramelli, eds.,

Astronomical Society of the Pacific Conference Series (2009), Vol. **405**, p. 461.
18. V. Martínez Pillet, J. C. Del Toro Iniesta, A. Álvarez-Herrero, V. Domingo, J. A. Bonet, L. González Fernández, A. López Jiménez, C. Pastor, J. L. Gasent Blesa, P. Mellado, J. Piqueras, B. Aparicio, M. Balaguer, E. Ballesteros, T. Belenguer, L. R. Bellot Rubio, T. Berkefeld, M. Collados, W. Deutsch, A. Feller, F. Girela, B. Grauf, R. L. Heredero, M. Herranz, J. M. Jerónimo, H. Laguna, R. Meller, M. Menéndez, R. Morales, D. Orozco Suárez, G. Ramos, M. Reina, J. L. Ramos, P. Rodrguez, A. Sánchez, N. Uribe-Patarroyo, P. Barthol, A. Gandorfer, M. Knoelker, W. Schmidt, S. K. Solanki, and S. Vargas Domínguez, "The imaging magnetograph eXperiment (IMaX) for the sunrise balloon-borne solar observatory," Sol. Phys. **268**, 57–102 (2011).
19. P. Barthol, A. Gandorfer, S. K. Solanki, M. Schüssler, B. Chares, W. Curdt, W. Deutsch, A. Feller, D. Germerott, B. Grauf, K. Heerlein, J. Hirzberger, M. Kolleck, R. Meller, R. Müller, T. L. Riethmüller, G. Tomasch, M. Knölker, B. W. Lites, G. Card, D. Elmore, J. Fox, A. Lecinski, P. Nelson, R. Summers, A. Watt, V. Martínez Pillet, J. A. Bonet, W. Schmidt, T. Berkefeld, A. M. Title, V. Domingo, J. L. Gasent Blesa, J. C. Del Toro Iniesta, A. López Jiménez, A. Álvarez-Herrero, L. Sabau-Graziati, C. Widani, P. Haberler, K. Härtel, D. Kampf, T. Levin, I. Pérez Grande, A. Sanz-Andrés, and E. Schmidt, "The sunrise mission," Sol. Phys. **268**, 1–34 (2011).
20. I. Haller, "Thermodynamic and static properties of liquid crystals," Prog. Solid State Chem. **10**, 103–118 (1975).
21. P. G. de Gennes, J. Prost, and R. Pelcovits, "The physics of liquid crystals," Phys. Today **48**(5), 70–71 (1995).
22. P. G. De Gennes, "Phenomenology of short-range-order effects in the isotropic phase of nematic materials," Phys. Lett. A **30**, 454–455 (1969).
23. G. Capobianco, F. Crudelini, L. Zangrilli, C. Buscemi, and S. Fineschi, "E-KPol temperature calibration," OATo Technical Reports, 111 (2008).